SEPARATION AND WAKES
OVER
THREE-DIMENSIONAL BODIES

by

CHRISTOPHER E. COSTIS

Dissertation submitted to the Graduate Faculty of the
Virginia Polytechnic Institute and State University
in partial fulfillment of the requirements
for the degree of

DOCTOR OF PHILOSOPHY

in

Engineering Science and Mechanics

APPROVED

D. P. Telionis, Chairman	Th. Herbert
D. T. Mook	A. H. Nayfeh
W. S. Saric	C. L. Prather

September 1985

Blacksburg, Virginia

ACKNOWLEDGEMENTS

The author is thankful to his thesis advisor and his committee for their support and advice. The support of Naval Air Systems Command under Contract Nos. N00167-82-K-0085 and N00167-84-C-0044, Dr. T. C. Tai monitor is also gratefully acknowledged.

TABLE OF CONTENTS

CHAPTER I
INTRODUCTION..... 1

1.1 General..... 1
1.2 Introduction to the Problem..... 4
1.3 Literature..... 6

CHAPTER II
PRELIMINARY CONCEPTS IN 3-D FLOWS..... 13

2.1 Introduction..... 13
2.2 Systems of Coordinates..... 14
2.3 Survey of Numerical Solutions of 3-D B-L Equations..... 16
2.4 The Potential Flow over an Ellipsoid..... 18
2.5 Local-Similarity Solutions..... 21

CHAPTER III
FLOW VISUALIZATION..... 35

3.1 Introduction..... 35
3.2 Water Tunnel..... 36
3.3 The Model..... 38
3.4 Skin-Friction Line Visualization..... 40
3.5 Vortex Sheet Visualization..... 51

CHAPTER IV
VELOCITY MEASUREMENTS..... 61

4.1 Introduction..... 61
4.2 The Design of the Optical Arrangement..... 62
4.3 The Traversing Mechanism..... 66
4.4 Optical and Electronic Equipment..... 71
4.5 Data Reduction..... 76

CHAPTER V
THE VORTEX LATTICE METHOD..... 106

5.1 Introduction..... 106
5.2 Potential Flow Calculations..... 108
5.3 Viscous Inviscid Interaction..... 116
5.4 Results and Discussion..... 122

CHAPTER VI
CONCLUSIONS AND RECOMMENDATIONS..... 145

REFERENCES 148

LIST OF FIGURES

Fig. 1.1 Maskell's (1955) Concepts on Three-Dimensional Flow Separation)..... 3

Fig. 1.2 Regions of interest in a 3-D external flow..... 5

Fig. 2.1 The coordinate systems..... 15

Fig. 2.2 Flow about an ellipsoid with axes ratios a:b:c = 4:1:1 (prolate spheroid) at an angle of attack a = 30°..... 25

Fig. 2.3 Flow about an ellipsoid with axes ratios a:b:c = 70:10:7 and a free stream U_∞ = cos 15°, V_∞ = sin 15°, W_∞ = sin 15°..... 26

Fig. 2.4 Flow about an ellipsoid with axes ratios a:b:c = 50:30:10 and free stream U_∞ = cos 30°, V_∞ = sin 15°, W_∞ = sin 15°..... 27

Fig. 2.5 Lines of separation for a prolate spheroid with axes ratios a/b = 2 and angle of attack a = 20°. _____, Stock (1980; -----, Geissler (1973); , present method..... 29

Fig. 2.6 Lines of separation for a prolate spheroid with axes ratios a/b = 4 and angles of attack a = 15° and 30°. _____, Stock (1980); -----, Geissler (1973); , present method..... 30

Fig. 2.7 Lines of separation for a prolate spheroid with axes ratios a/b = 6 and angles of attack a = 5°, 10° and 15°. _____, Stock (1980); -----, Geissler (1973); , present method..... 31

Fig. 2.8 Lines of separation and external streamlines for a prolate spheroid of α/b = 6 at an angle of attack α = 6°. _____, Cebeci et al. (1983); -----, Wang (1975); , present approximate method..... 32

Fig. 2.9 Lines of separation and external streamlines for a prolate spheroid of a/b = 6 at an angle of attack α = 15° as reported in Cebeci et al. (1983); , present approximate method; -o-o-o-o-; present experimental data..... 33

Fig. 2.10 Lines of separation and external streamlines for a prolate spheroid of a/b = 4 at an angles of attack a = 30° as reported in Cebeci et al. (1983); , present approximate method; -o-o-o-o-; present experimental data..... 34

Fig. 3.1 Schematic representation of the water tunnel..... 37

Fig. 3.2 RMS spectrum of the velocity fluctuation. If the low frequencies (less than 4 Hz) are eliminated, then the turbulence level is less than 0.1%. The spikes in the spectrum correspond to the 60 Hz and its multiples and are due to the power supply..... 39

Fig. 3.3 Skin friction lines for $\alpha = 3°$. (a) Leeward view, (b) View from $\phi = 120°$, (c) Side view..... 42

Fig. 3.4 Skin friction lines for $\alpha = 6°$. (a) Leeward view, (b) View from $\phi = 120°$, (c) Side view..... 43

Fig. 3.5 Skin friction and inviscid lines for $\alpha = 10°$. (a) Leeward view, (b) View from $\phi = 120°$..... 44

Fig. 3.6 Skin friction and inviscid lines for $\alpha = 20°$. (a) Leeward view, (b) View from $\phi = 120°$..... 45

Fig. 3.7 The three regions of difficult accessibility for $\alpha = 10°$. (a) Leeward view, (b) View from $\phi = 120°$.... 46

Fig. 3.8 Skin friction and inviscid lines for $\alpha = 30°$. (a) Leeward view, (b) View from $\phi = 120°$..... 48

Fig. 3.9 Approximate form of skin friction lines for $\alpha = 10°$. (a) Leeward view, (b) View from $\phi = 120°$..... 49

Fig. 3.10 Approximate form of skin friction lines for $\alpha = 20°$. (a) Leeward view, (b) View from $\phi = 120°$..... 50

Fig. 3.11 Qualitative shape of skin-friction lines superimposed on a figure from Cebeci et al. (1981). _____, line of accessibility; ___ _ ___, inviscid streamline, Cebeci et al. (1981). __ _ __ _; skin friction lines conjectured by the present author..... 52

Fig. 3.12 Laser cuts of separating vortex sheets at different axial locations for a spheroid at $\alpha = 30°$..... 55

Fig. 3.13 View from downstream of the field of Fig. 3.12..... 56

Fig. 3.14 Composite flow visualization of skin friction lines with vortex sheet cuts..... 57

Fig. 3.14 (contd.)..... 58

Fig. 3.15 Schematic Representation of the skin friction lines and vortex sheets as obtained by flow visualization... 59

Fig. 4.1 Schematic representation of the crossing of 3 beams. All 3 beams are in the same plane. Interference between beam 1 and 2 generates the velocity component V_{12} and interference between 2 and 3 generates the component V_{23}..... 63

Fig. 4.2 Schematic representation of errors inolved in 3-beam LDV system, or 2 velocity component measurements..... 65

Fig. 4.3 Schematic of the optical bench, optical equipment and traversing options..... 67

Fig. 4.4 Model support..... 68

Fig. 4.5 Example of laser beam locations with respect to the body and output of program for the calculation of measuring position..... 70

Fig. 4.6 Arrangement of sending optics..... 72

Fig. 4.7 The optical bench for the measurement of 2 components 74

Fig. 4.8 The actual experimental points shown together with the smoothed profile on the leeward side at the fourth station, V_{12}; V_{23}..... 77

Fig. 4.9 The u-component velocity profile. Horizontal and vertical scales are marked in tenths of free stream velocity and increments of 1/10" (and 0.85 mm) respectively..... 79

Fig. 4.10 The u-component velocity profile calculated by Patel and Baek..... 80

Fig. 4.11 The u- and v-velocity components at the first station of measurement..... 82

Fig. 4.12 The u- and v-velocity components at the second station of measurement..... 83

Fig. 4.13 The u- and v-velocity components at the third station of measurement..... 84

Fig. 4.14 The u- and v-velocity components at the fourth station of measurement..... 85

Fig. 4.15 The u- and v-velocity components at the fifth station of measurement..... 86

Fig. 4.16 Composite figure showing all the velocity profiles in the two-dimensional space of the ellipsoid surface.... 88

Fig. 4.17 Interpolated velocity profiles at x/a = 0.2..... 89

Fig. 4.18 Interpolated velocity profiles at x/a = 0.25..... 90

Fig. 4.19 Interpolated velocity profiles at x/a = 0.3..... 91

Fig. 4.20 Interpolated velocity profile at x/a = 0.35..... 92

Fig. 4.21 Interpolated velocity profile at x/a = 0.4..... 93

Fig. 4.22 Interpolated velocity profile at x/a = 0.45..... 94

Fig. 4.23 Interpolated velocity profile at x/a = 0.5..... 95

Fig. 4.24 Interpolated velocity profile at x/a = 0.55..... 96

Fig. 4.25 Interpolated velocity profile at ϕ = 90°..... 97

Fig. 4.26 Interpolated velocity profile at ϕ = 105°..... 98

Fig. 4.27 Interpolated velocity profile at ϕ = 120°..... 99

Fig. 4.28 Interpolated velocity profile at ϕ = 135°..... 100

Fig. 4.29 Interpolated velocity profile at ϕ = 150°..... 101

Fig. 4.30 Interpolated velocity profile at ϕ = 165°..... 102

Fig. 4.31 Interpolated velocity profile at ϕ = 180°..... 103

Fig. 4.32 Composite of interpolated profiles at x/a = 0.2, 0.3, 0.4 and 0.5..... 104

Fig. 4.33 Composite of interpolated profiles at x/a = 0.25, 0.35, 0.45 and 0.55..... 105

Fig. 5.1 Velocity induced at a point due to a vortex segment... 109

Fig. 5.2 Vortex lattice and control points for a sphere (10 circumferential and 11 axial panels..... 111

Fig. 5.3 Vortex lattice and control points for an ellipse with axes ratio 1:4 (6 circumferential and 25 axial panels) 112

Fig. 5.4 The velocity distribution along the meridional of a sphere. _____, exact solution; ', vortex lattice with 6x27 circumferential x axial panels..... 114

Fig. 5.5 The velocity distribution along the meridional of a prolate spheroid at zero angle of attack. _____, exact solution; °, vortex lattice with 4x28 circumferential x axial panels..... 115

Fig. 5.7 Vorticity field in 2 dimensions. (a) Schematic of discrete vortex shedding at the separation points S_1 and S_2. (b) The contour of integration for the circulation..... 119

Fig. 5.8 The boundary layer and total vorticity flux near separation. The plane xy is on the surface of the body. The plane y,z is a separation surface..... 121

Fig. 5.9 Skin friction lines, separation and separated vortex sheets over a prolate spheroid started impulsively from rest (a) $t = 0$, (b) $t = 3\Delta t$, (c) $t = 4\Delta t$, (d) $t = 5\Delta t$, (e) $t = 6\Delta t$. 124

Fig. 5.9 continued..... 125

Fig. 5.10 The instantaneous line of separation for a prolate spheroid started impulsively from rest..... 126

Fig. 5.11 Lines of separation and external streamlines for a prolate spheroid of $a/b = 4$ at an angle of attack $a = 30°$ as reported in Cebeci, et al. (1981) (solid line); ----, Wang (1975); o-o-, present experimental results; +, present numerical results..... 128

Fig. 5.12 Comparison of flow visualizations from Ref. 20 with present calculations. View from $\phi = 90°$..... 129

Fig. 5.13 Schematic representation showing a vortex line off the surface of the body..... 130

Fig. 5.14 Skin friction and potential lines of an ellipsoid with axes ratio 1:6:4..... 131

Fig. 5.14b Skin friction lines, potential ines and separated vortex sheets over an ellipsoid with axes ratio 1:6:4 started impulsively from rest at an angle of attack, $\alpha = 30°$..... 132

Fig. 5.15 Skin friction lines, potential lines and separated vortex sheets over an ogive-cylinder body started impulsively from rest at an angle of attack, $\alpha = 24.5°$ 134

Fig. 5.16 Results for the body of Fig. 15 but with separation line fixed along a generator of the body..... 135

Fig. 5.17 The wake over a prolate spheroid with axes ratio 1:4 and the separation line fixed according to Meier's data 136

Fig. 5.18 Comparison of vector fields at a cross-sectional plane of x = 0.72. (Experiment, Ref. 26 (b) Present theory 137

Fig. 5.19 Experimental and analytical pressure distributions for the case of Fig. 17, along the meridionals ϕ = 22.5° and 112.5°, 0, experimentl, Ref. 26. _____, present theory; -----, potential flow..... 138

Fig. 5.20 Experimental and analytical pressure distribution for the case of Fig. 17, along the axial location x/L = 0.4812. 0, experiment, Ref. 26. _____, present theory; -----, potential flow..... 140

Fig. 5.21 Experimental and analytical pressure distribution for the case of Fig. 17, along the axial location x/L = 0.3501. 0, experiment, Ref. 26. _____, present theory; -----, potential flow..... 141

Fig. 5.22 Experimental and analytical pressure distribution for the case of Fig. 17, along the axial location x/L = 0.4812. 0, experiment, Ref. 26. _____, present theory; -----, potential flow..... 142

Fig. 5.23 Experiment and analytical pressure distribution for the case of Fig. 17, along the axial location x/L = 0.6061. 0, experiment, Ref. 26. _____, present theory; -----, potential flow..... 143

Fig. 5.24 Experimental and analytical pressure distribution for the case of Fig. 17, along the axial location x/L = 0.7725. 0, experiment, Ref. 26. _____, present theory; -----, potential flow..... 144

CHAPTER I

INTRODUCTION

1.1 General

In the past, developments in the fields of aeronautical and naval structures were achieved mainly through tests of scaled models. The design and development of a vessel was based partly on measurements and observations of the flow about a scale model, and partly on previous experience from already existing similar vessels. Today, it is feasible to base the design on numerical calculations of the flow field.

The detailed study of three-dimensional boundary-layer flows is a recent chapter in the science of fluid mechanics. Only recently three-dimensional flows attracted the attention of fluid dynamicists, and this is primarily due to the development of high-speed digital computers. The Navier-Stokes equations and the boundary-layer equations for three-dimensional flows accept analytical solutions only for a few cases of little practical interest. Only the modern digital computer can provide a solution for more practical cases.

The principle difference between a two and a three-dimensional boundary-layer flow is the following: in the two-dimensional case, the fluid in the boundary layer can be forced by a strong adverse pressure gradient induced by the external flow, causing separation and, eventually, formation of wake. The presence of the third dimension

calls for an entirely new consideration of concepts like: separation patterns, vorticity convection and wake behavior.

In 2-D flows, the concept of separation 'point' is easy to be defined. Thus for steady 2-D flow, vanishing of the wall shear stress defines the separation point and the beginning of separation. Such a definition in 3-D flows is not possible. In 3-D flows the definition of the separation 'line' has been the topic of controversy among researchers.

The first to give topological description of the concept of separation in 3-D flows was Mashell (1955). He distinguished 3-D separation into two types (Fig. 1.1): the closed or bubble-type of separation and the open or free-vortex layer type of separation. In the closed or bubble-type of separation there is a region behind the 'line' of separation which is not accessible to fluid particles coming from any point upstream. On the other hand, for the case of open separation, the region behind the separation line can be reached by fluid particles emanating from the region upstream of separation. In the present work, the line of separation is defined as the line of convergence of the skin friction lines. Our experimental evidence indicates indeed that the convergence of skin-friction lines is an unambiguous criterion of separation.

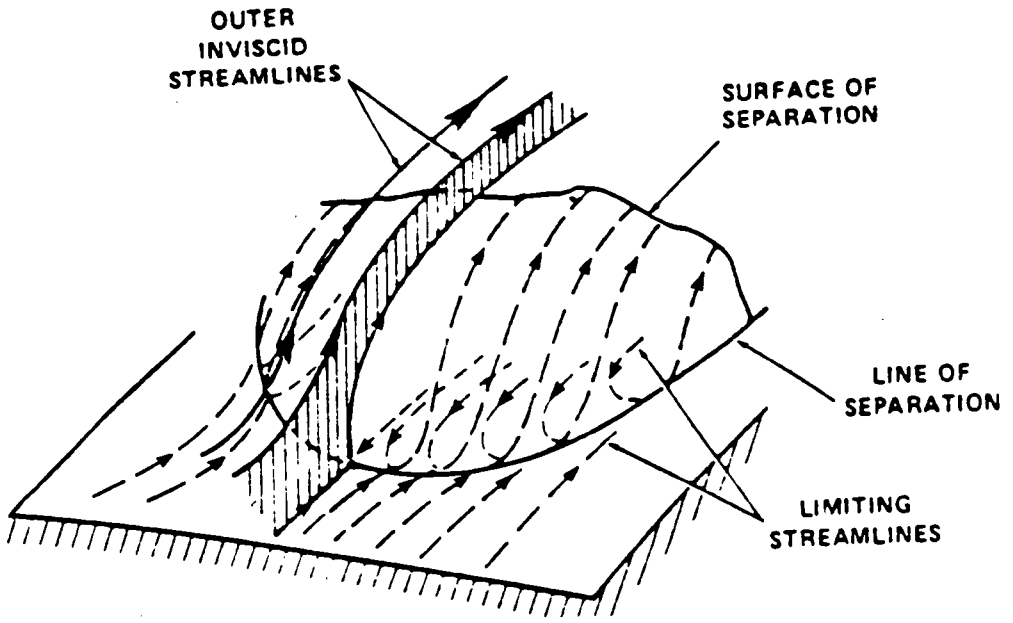

Figure 10a - Bubble

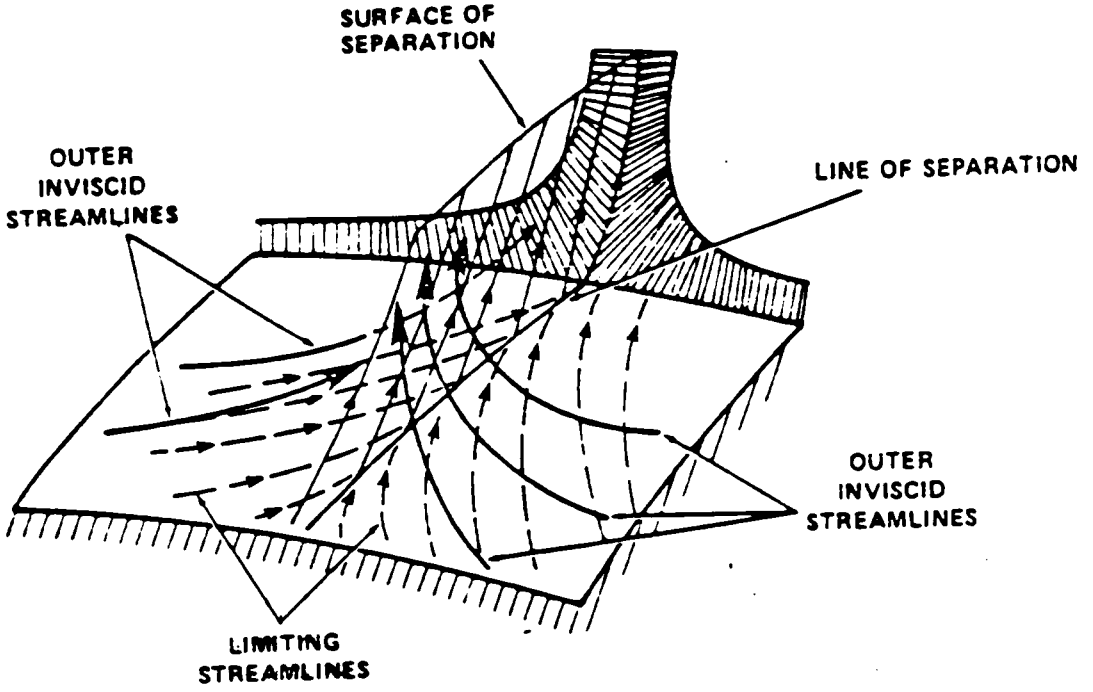

Figure 10b - Free-Vortex Layer

Figure 1.1 Maskell's (1955) Concepts on Three-Dimensional Flow Separation)

1.2 Introduction to the Problem

In the study of the flow about a 3-D body one can define three regions of interest. Starting from the front stagnation point and moving to the leeward side of the body, one considers first the region of attached flow (Fig. 1.2). This is the region of the development and growth of the three-dimensional boundary layer. The second region one encounters is the separation region. The flow detaches from the surface of the body. Vorticity is shed into the free-stream, usually along the lines of separation. The vorticity shed from the separation line enters the freestream and forms vorticity sheets. These sheets interact with the freestream and form the third region of interest known as the wake.

The features of the attached flow depend greatly upon the shape of the wake and the location of the separation line. On the other hand, the strength of the shed vorticity depends on the development and growth of the 3-D boundary layer in the attached flow region. Furthermore, the shape of the wake depends strongly on the location of the separation line and the rate of vorticity shedding.

The present study attacks the problem of the flow about a finite three-dimensional body, using both experimental and numerical methods. The experimental methods include flow-visualization techniques to reveal the skin friction line patterns. Moreover Laser-Doppler velocimetry was used for the first time for flow measurement about a 3-D bluff body at an angle of attack. In the numerical study a combination of an approximate boundary-layer method and an unsteady vortex-lattice code was used to study the growth of the wake simultaneously with the 3-D boundary-layer development. In this dissertation, individual studies of

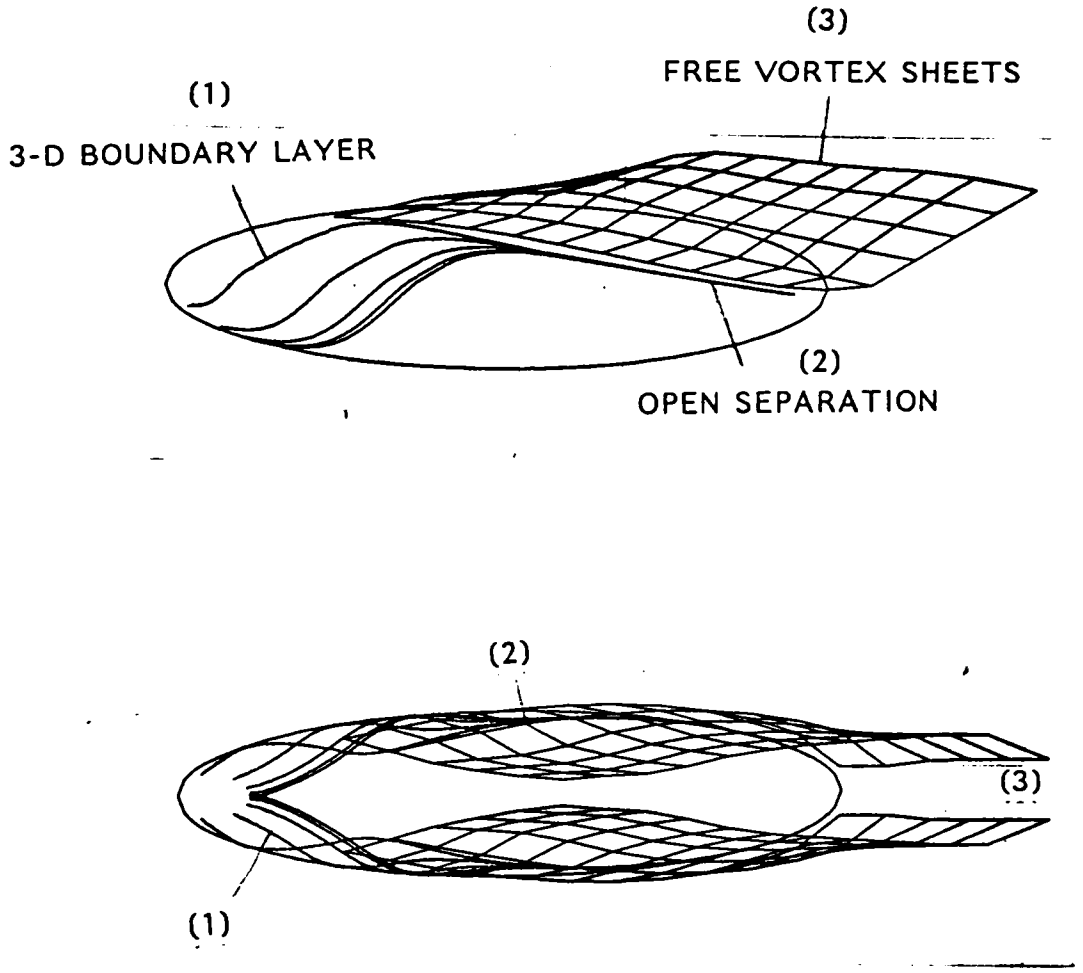

Fig. 1.2 Regions of interest in a 3-D external flow.

extensions and generalizations of concepts like separation, vortex shedding, etc. can be found. The present effort is therefore, at least to the knowledge of the author, the first global study of this complex problem.

1.3 Literature

Looking back into early attempts of integration of the boundary-layer equations in three dimensions, one has to stop at Sears' solution of the flow about infinite cylinders in yaw (1948). In this early work an analytical solution for a non-axisymmetric flow appears for the first time. Sears' work, although of great importance for the study of flows over swept wings, offers little insight into the flow about a finite, arbitrary body. It was Maskell (1955) who introduced the concepts of "vortex-" and "bubble-" separation which later became known as "open" and "closed" separation for 3-D flows. Maskell's considerations, although disputed by many researchers, have actually introduced for the first time a reconsideration of basic concepts, such as separation, in the presence of the third dimension.

The studies that followed in the area of three-dimensional flows can be divided into various branches, depending on the method of approach: experimental measurements, flow visualizations, studies of potential flow with or without wake development, numerical integration of the boundary-layer equations, integral methods, and topological studies. Experimental data, readily available for comparison with analysis were obtained offered by Meier and Kreplin (1980), but only for high-Reynolds-number flows. Meier, Kreplin and Vollmers studied the

flow over a prolate spheroid at incidence and made detailed measurements of the wall shear stress (1980), investigated the transition of the boundary layer and separation for both laminar and turbulent flows (1980) and took detailed data of velocity profiles and pressure coefficients for various angles of attack and free-stream velocities (1980, 1981). The measurements were obtained in a wind tunnel for the case of a prolate spheroid of axis ratio 1 to 6. Special probes were used for shear stress and velocity measurements, while the experimental techniques were greatly simplified by the axisymmetry of the body.

Ramaprian et al. (1981) obtained detailed information on three-dimensional velocity profiles using also a three-hole probe but for the case of a rather arbitrarily defined body of revolution. Numerous experimental data have been obtained for 3-D boundary-layer flows, such as East's (1973) for the turbulent boundary layer about a delta wing and Elsenaar et al. (1974) for the turbulent boundary layer under infinite swept wing conditions. But the work of Meier and his associates is a good reference for the study of the boundary layer in connection with separation in three dimensions.

Numerous visualizations of flow have been presented, especially for the case of finite wings. However the patterns of 3-D separation were visualized clearly by Oudart and Eichelbrenner (1955) for a prolate spheroid of a 1 to 6 axes ratio and by Han and Patel (1979) for a 1 to 4 axes ratio. Dye injection on the surface of the body was the method of visualization in both cases. Meier et al. (1980) employed again flow vizualization technique for further investigations of the problem.

The starting point for the integration of the boundary-layer equations for 3-D flow dates back in 1951. A good number of integrations has been presented, each of which has approached in a different way the two basic difficulties encountered in this problem: (i) a coordinate system that overrides the singularity at the blunt nose of the body and (ii) a stable numerical scheme that can handle large negative cross-flows in the marching process.

Blottner et al. (1973) considered the case of a prolate spheroid with axes-ratio 1 to 4. They used an orthogonal system of coordinates and Crank-Nicolson and Krause's zig-zag numerical schemes. Wang in a sequence of publications since 1974 (1974, 1975, 1982) also calculated the flow about a prolate spheroid at incidence. He used an orthogonal mesh generated by meridional and normal to the axis planes for the integration, and various numerical schemes. He took careful account of the zones of influence and dependence in the marching process and his work seems to support the concept of open separation originally introduced by Maskell.

Geissler (1974) used also a variation of Krank-Nicolson's numerical scheme and a mesh created by equi-potentials and streamlines for the study of the flow about the prolate spheroid. Patel and Choi (1979) studied the flow about a prolate spheroid as well as about a more general body of revolution, for the laminar and turbulent cases. They used Crank-Nicolson's scheme and alternating-direction-implicit scheme. Recently Patel and Baek (1983) performed a numerical integration of the flow about a prolate spheroid of 1 to 4 axis-ratio using exact theoretical as well as experimentally obtained outer potential flow data.

More involved was the numerical scheme used by Cebeci, Khattab and Steuartson (1981) for the integration of the boundary-layer equations. They employed a new transformation of the body coordinates to facilitate the computation of the solution near the blunt nose and two variations of standard-box scheme for marching in regions of cross-flow reversal. They are referred to as "zigzag box" and "characteristic box." New concepts, like accessible regions and OK of accessibility, have been introduced to interpret the behavior of the numerical scheme in various regions of integration. Ragab (1982) used a non-orthogonal curvilinear coordinate system to circumvent the nose singularity and a finite-difference scheme, called the 'wedge' scheme to approach separation. Adequate agreement was found between his results and Meier's experimental data for both laminal and turbulent flow about a prolate spheroid.

Among the integral methods for the solution of the boundary-layer equations Stock (1980) calculated the flows about ellipsoids of various axis-ratios and angles of incidence as well as for separated flows about infinite swept wings. It must be mentioned here that Prandtl was the first to propose a method for obtaining approximate solutions of 3-D boundary-layer flows with the aid of momentum equations (1945).

Tobak and Peake (1981) approached the problem of 3-D separation using topological concepts. However the topology of 3-D separated flows is an open subject since there is no agreement, in general, among researchers. Wang (1982) presented a critical view of various suggestions regarding separation patterns on axisymmetric bodies at incidence.

In all the numerical integrations of the boundary layer equations like the ones discussed above, the outer flow was given either by exact potential solutions or by experimental data of pressure distribution on the surface. The upstream influence of the wake was therefore either neglected or introduced in the outer flow in the form of experimental data. For the wake to be taken into account, solution of the Navier-Stokes equations for the three components of the velocity must be considered. Wang (1982) attempted such an integration but for a bounded region on a prolate spheroid. The problem of the wake development has been faced successfully for two-dimensional bluff bodies by means of vortex methods. Gerrard (1966), Sarpkaya (1968), Deffenbaugh et al. (1974), Kuwahara (1978), Sarpkaya et al. (1979) are few of the researchers who presented detailed treatments of the wake develoment behind circular cylinders or other blunt bodies.

The first efforts to study 3-D wake regions were mainly concerned with elongated three-dimensional bodies. The solutions given were based on the cross-flow plane analogy, which employs two-dimensional solutions in cross sections of the body. Marshall and Deffenbauch (1974) presented such a work for the case of a body of revolution using results of the flow about a 2-D circular cylinder.

Purely three-dimensional considerations for the study of the separated flows about 3-D bodies appeared only recently. One set of such methods is known as vortex-lattice methods. The first vortex-lattice solution was given by Belotserkovskii (1966) for the case of thin wings of arbitrary planform. Mook and Maddox (1974), Kandill et al. (1976), Zorea and Rom (1978) used vortex-lattice methods to treat

steady problems involving sharp-edge separation, while Atta et al. (1976), Thrasher et al. (1977), Levin and Katz (1980), Konstadinopoulos et al. (1981) treated the unsteady problem of sharp-edge geometry.

Three-dimensional flows involving separation over smooth surfaces have been considered only very recently. Fiddes (1980) expanded on a viscous-inviscid interacting method to solve the problem of 3-D separation over a cone. However his method is limited to slender body configurations and conical flows. Thrasher (1983) studied the flow over a semi-infinite body with a tangent-ogive nose and a cylindrical afterbody. He employed an interation version of a vortex-lattice scheme to solve the problem and assumed that the separation lines coincided with the generators of the body. Almonsino and Rom (1983) have considered the flow about a very similar semi-infinite body and employed again an iteration method to achieve convergence of the wake vortices. However they modeled the separated vortex sheets by only 4 vortex lines on each side emanating from very narrow segments aligned again with generators of the body. Most recently, Almonsino (1985) refined this method which, however, still requires as input the line of separation. In all investigations of three-dimensional bluff-body separated flows, the body was assumed to be semi-infinite. Moreover, with the exception of the degenerate case considered by Fiddes (1980), all other investigators assumed that the position of the separation line is known and that in fact coincides with a meridional line of axisymmetric bodies.

The present study is divided into four chapters. The first chapter includes preliminary work for the study of the flow about an ellipsoid

of arbitrary axis-ratio at angle of attack. A code has been developed for the calculation of the potential flow. Boundary-layer approximate solutions have been derived by means of local-similarity methods. Moreover, flow visualization of the surface streamlines for a prolate spheroid of 1 to 4 axis-ratio are presented. The pictures of the flow have been digitized and combined for every angle of attack. The second chapter includes the treatment of the wake for the case of an ellipsoid by means of vortex-lattice and vorticity methods. The boundary-layer solution has been employed to predict the location of the separation line. The third chapter includes the experimental work, conducted in a low-turbulence water tunnel and discussion of velocity measurements using a two-component Laser Velocimetry System. Finally, the fourth chapter contains comparisons of the data obtained by the preceding methods, among themselves as well as with other published related works. A discussion concludes the present study.

CHAPTER II

PRELIMINARY CONCEPTS IN 3-D FLOWS

2.1 Introduction

In this chapter we discuss the solutions to some special problems, necessary for the discussion of subsequent chapters. Each of the problems discussed here can be addressed independently of the main body of the present work. Moreover, the solutions offered have been obtained independently by the present author, although the ideas employed are not altoghether original.

There is no analytical solution of the inviscid flow about a general three-dimensional smooth body. Conformal mapping cannot be applied in 3 dimensions. However, for some flows about a few special bodies, analytical solutions exist. Such a family of 3-D bodies is the family of ellipsoids of arbitrary axes ratio. In the present work, it appeared necessary to obtain an analytical solution of the inviscid flow about a non-axisymmetric body at an arbitrary angle of attack. A code has been developed for the study of the inviscid flow about an arbitrary ellipsoid at an angle of attack, based on a classical development (Lamb 1955; Band and Payne, 1974).

An approximate 3-D boundary-layer solution was also necessary. In the process of this work we have reproduced Tai's (1981) streamline method. Inspired by this method we have also developed a method based on the concept of local similarity. The results of these and a third oversimplified model for the calculation of laminar 3-D separation are

compared with results of more involved methods as well as with experimental data.

2.2 Systems of Coordinates

Three systems of coordinates are employed here. The Cartesian system (Fig. 2.1) of coordinates is used in calculations of the development of the wake. The X-axis and its origin coincide with the body's central axis and its nose respectively. For most cases studied, the Y-axis is in the plane of symmetry of the flow. For the study of the flow in the attached region, and especially for the boundary-layer calculations, another system of coordinates is used (Fig. 2.1). The three coordinates of that system are X-ϕ-z as defined in Fig. 2.1b. The X and ϕ coordinates are the polar coordinates used for the definition of the body. The surface of a body is given by a function of the coordinates X and ϕ, as shown in the Figure. The z-coordinate is measured along normals to the surface of the body. In this way the system of coordinates is adapted to the natural description of the 3-D boundary layer. Moreover for the case of Sears' problem, the well known cylindrical system of coordinates is used. The cylindrical system of coordinates is a special case of the one mentioned above. The only difference is that the z coordinate is normal not to the surface, but to the central axis (Fig. 2.1a).

Connected to the system of coordinates is the definition of velocity components. For the Cartesian system of coordinates the three components of velocity aligned with the axes X, Y, and Z are indicated by U, V, and W respectively. For the second system of coordinates, it

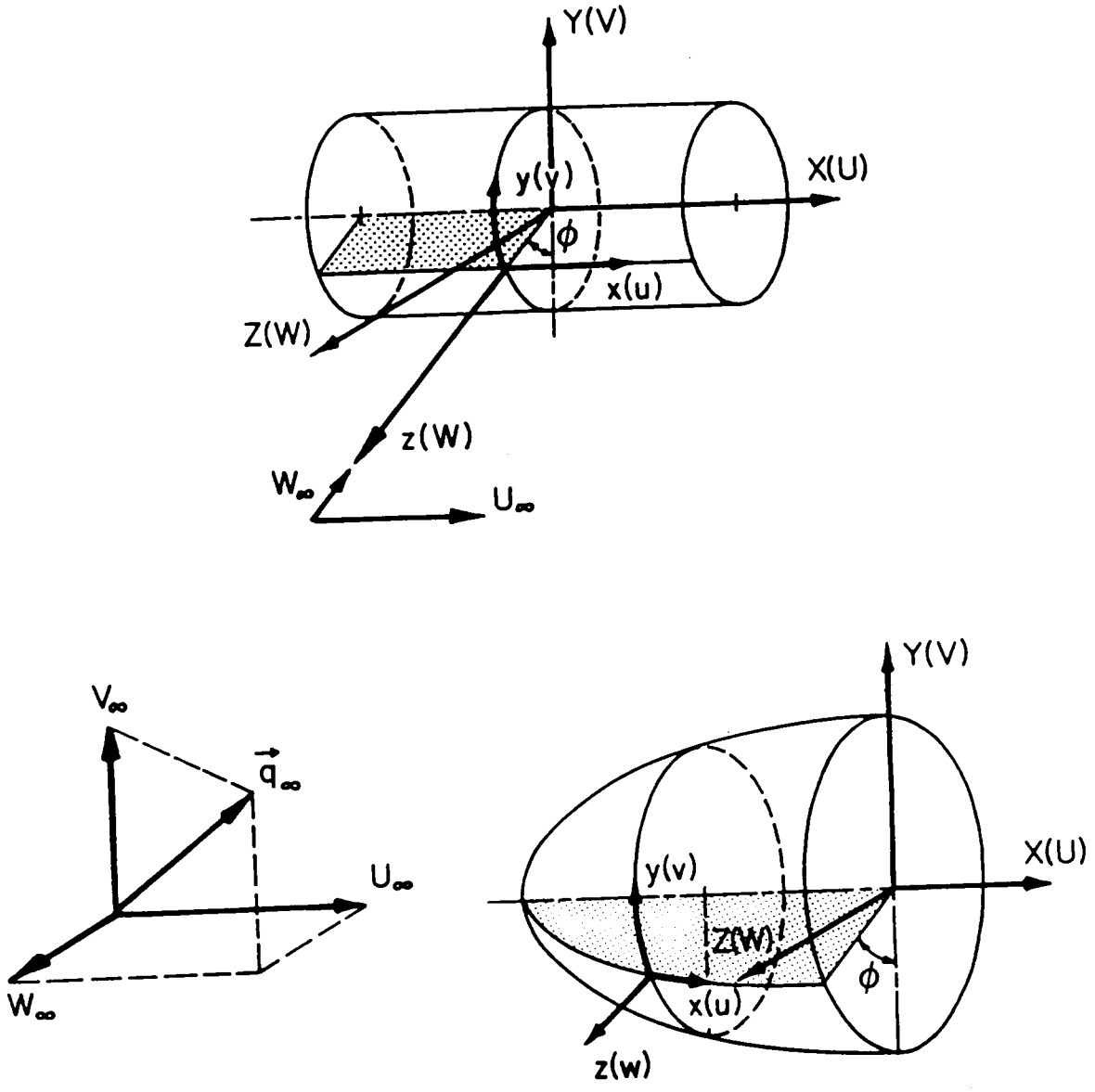

Fig. 2.1 The coordinate systems.

is preferrable to introduce the velocity components tangent to the surface. Therefore the u component is tangent to the surface and in a plane passing through the x-axis while the v component is tangent to the surface and in a plane perpendicular to the x-axis. The same notation is used for the cylindrical system of coordinates (Fig. 2.1a & b).

2.3 Survey of Numerical Solutions of 3-D B-L Equations

Two basic difficulties are encountered in this problem: (i) a singularity at the nose of the body associated with some coordinate systems, and (ii), numerical instabilities that are encountered in the marching process in case of large negative cross-flows. In the 1970's a number of integrations have been presented, each of which has approached in a different way the aforementioned two basic difficulties.

Blottner and Ellis (1973) considered the case of a prolate spheroid with axis-ratio 1 to 4. They used an orthogonal system of coordinates and Crank-Nicolson and Krause's zig-zag numerical schemes. Wang in a sequence of publications since 1974, (Wang, 1974,1975,1980) calculated also the flow about a prolate spheroid at incidence. He used an orthogonal mesh for the integration, generated by meridional and normal to the axis planes, and various numerical schemes. He took careful account of the zones of influence and dependence in the marching process and his work seems to support the concept of open separation originally introduced by Maskell. Geissler (1974) used also a variation of Krank-Nicolson numerical scheme and a mesh created by equipotentials and streamlines again for the study of the flow about a prolate spheroid.

Patel and Choi (1979) studied the flow about a prolate spheroid as well as about a more general body of revolution, for the laminar and turbulent cases. They used a Crank-Nicholson and alternating-direction-implicit scheme. Recently Patel and Baek (1983) performed a numerical integration for the flow about a prolate spheroid of 1 to 4 axis-ratio using exact theoretical as well as experimental data of outer flow.

More involved was the numerical scheme used by Cebeci, Khattab and Steuartson (1981). They employed a new transformation of the body coordinates to facilitate the computation of the solution near the blunt nose and two variations of the standard-box scheme for marching in regions of cross-flow reversal. They are referred to as zig-zag box and characteristic box. New concepts, like regions of accessibility and OK of accessibility, have been introduced to interpret the behavior of the numerical scheme in various domains of integration.

Ragab (1982) used a non-orthogonal curvilinear coordinate system to circumvent the nose singularity and a finite-difference scheme, called the 'wedge' scheme to approach separation. Adequate agreement was found between his results and Meier's experimental data for both, laminal and turbulent flow about a prolate spheroid.

The methods described here are far more simple and require at least 2 orders of magnitude less time and space. They are not offered here as substitutes of the more involved methods described above, although the results thus generated are comparable to the results of other methods. The techniques described here have been developed only to demonstrate how an outer flow method could be coupled with the boundary-layer solution.

2.4 The Potential Flow over an Ellipsoid

The prolate spheroid has been chosen by all investigators as a test case for 3-D boundary-layer investigations on separation. One of the significant advantages that such a choice offers is the existence of an exact analytical solution to Laplace's equation. This is given by velocity components on the skin of the spheroid (Tai, 1981).

$$\frac{u_e}{q_\infty} = \frac{1}{\left[1-e^2\left(\frac{X}{a}-1\right)^2\right]^{1/2}}\left\{(1+k_a)(\cos\alpha)\times\right.$$
$$\left.\left[2\frac{X}{a}-\left(\frac{X}{a}\right)^2\right]^{1/2}+\left(\frac{b}{a}\right)(1-k_c)(\sin\alpha)\left(\frac{X}{a}-1\right)\cos\phi\right\} \tag{2.4.1}$$

$$\frac{v_e}{q_\infty} = (1+k_c)\sin\alpha\sin\phi \tag{2.4.2}$$

where q_∞ is the velocity at infinity, ϕ is the meridional angle, α is the angle of attack, a, b are the major semiaxes of the ellipse, e is the eccentricity, given by the formula

$$e = \sqrt{1-(b/a)^2} \tag{2.4.3}$$

and k_a and k_c are the following parameters

$$k_a = \left(\frac{1}{2e}\ln\frac{1+e}{1-e}-1\right)/\left(\frac{1}{1-e^2}-\frac{1}{2e}\ln\frac{1+e}{1-e}\right) \tag{2.4.4}$$

$$k_c = \frac{1}{1+2K_a} \tag{2.4.5}$$

A more general body with no symmetry about a particular axis which was found to be a challenging problem for the testing of a 3-D code is the ellipsoid of arbitrary axes ratios. We found that a potential solution can be easily obtained again on a personal computer and we outline it here for the convenience of other investigators who may want to compare our boundary-layer results with theirs. The potential velocity on the skin of the body is calculated in terms of an ellipsoid coordinate λ which is constant on all confocal ellipsoids and zero on the ellipsoid of interest (Band and Payne, 1979). The solution is given in terms of three integrals

$$I_1 = \int_0^\infty \frac{d\lambda}{(a^2+\lambda)\Delta}, \quad I_2 = \int_0^\infty \frac{d\lambda}{(b^2+\lambda)\Delta}, \quad I_3 = \int_0^\infty \frac{d\lambda}{(c^2+\lambda)\Delta} \tag{2.4.6}$$

where a, b and c are the three major axes and

$$\Delta^2 = (a^2+\lambda)(b^2+\lambda)(c^2+\lambda) \tag{2.4.7}$$

The constants α_0, β_0 and γ_0 and A, B and C are then defined as follows

$$\alpha_0 = abcI_1, \quad A = \frac{2}{2-\alpha_0} \tag{2.4.8}$$

$$\beta_0 = abcI_2, \quad B = \frac{2}{2-\beta_0} \tag{2.4.9}$$

$$\gamma_0 = abcI_3, \quad C = \frac{2}{2-\gamma_0} \tag{2.4.10}$$

For a cartesian system of coordinates aligned with the major axes, a, b and c, the velocity on the skin of the body is then given in terms of the components of the oncoming stream $(U_\infty, V_\infty, W_\infty)$ and the unit vector normal to the body at the point of interest, $\bar{e}$, with components (ℓ,m,n)

$$\bar{q} = (AU_\infty \bar{i} + BV_\infty \bar{j} + CW_\infty \bar{k}) - (AU_\infty \ell + BV_\infty m + CW_\infty n)\bar{e} \quad (2.4.11)$$

The unit vector, $\bar{e}$, normal to the ellipsoid at the point X, Y, Z has the cartesian components

$$\ell = Xa^{-2} \left(\frac{X^2}{a^4} + \frac{Y^2}{b^4} + \frac{Z^2}{c^4}\right)^{-1/2} \quad (2.4.12)$$

$$m = Yb^{-2} \left(\frac{X^2}{a^4} + \frac{Y^2}{b^4} + \frac{Z^2}{c^4}\right)^{-1/2} \quad (2.4.13)$$

$$n = Zc^{-2} \left(\frac{X^2}{a^4} + \frac{Y^2}{b^4} + \frac{Z^2}{c^4}\right)^{-1/2} \quad (2.4.14)$$

In terms of these quantities, the cartesian components U, V, W of the velocity $\bar{q}$ (see Fig. 2.1 for notation) are given by

$$U = AU_\infty - (AU_\infty \ell^2 + BV_\infty m\ell + CW_\infty n\ell) \quad (2.4.15)$$

$$V = BV_\infty - (AU_\infty \ell m + BV_\infty m^2 + CW_\infty nm) \quad (2.4.16)$$

$$W = CW_\infty - (AU_\infty \ell n + BV_\infty mn + CW_\infty n^2) \quad (2.4.17)$$

To obtain the components u, v and w along the system x, ϕ, z one needs, of course, to go through the proper transformation.

A computer program was prepared for the calculation of the topography of viscous and inviscid streamlines. In both cases, the inclination of the curve under investigation is given with respect to the local meridional direction. Streamlines are then calculated by any of the standard method of reconstructing a curve, if its slope is given everywhere. Integation was started at points on the meridionals $\phi = 90°$ and $\phi = 270°$ and was marched in both the upstream and the downstream direction. In this way, difficulties encountered in the neighborhood of stagnation points were avoided. In fact, the method provides a clear indication of accuracy at stagnation points where it was demonstrated that all lines cross each other at points not farther than a distance of a/1000 from the actual location of the stagnation point.

2.5 Local-Similarity Solutions

For a few special three-dimensional bodies it is relatively easy to obtain accurate numerical solutions of the three-dimensional boundary-layer equations. One class of such configurations are cylinders of arbitrary cross section in yaw with respect to the oncoming flow. For these special bodies the two momentum equations are uncoupled and the solution can be easily obtained (Sears, 1948). We assume here that the flow about a general 3-D configuration is locally similar to the flow about a special cylindrical body at an angle of yaw. In other words, we assume that the properties of the boundary layer at a specific station on the body of interest are similar to the properties at a suitably chosen point, on a special body, at a specific angle of yaw. The criterion for the determination of the special body shape, the angle of

yaw and the point on the body which corresponds to the point of our interest are based on properties of the outer flow. The known special solution is thus considered essentially a bank of properties which are drawn according to certain rules, in order to synthesize the properties of the flow about the body of interest. One of the physical and mathematical properties of the boundary layer which is missing from such a mathematical model is history. However, the limitations are not so severe, if there are no sharp changes in the pressure gradient distribution.

Consider the flow about a cylinder in yaw. Let the x, y and z axes be parallel to the generators, along the surface of the body but normal to the generators, and normal to the body surface respectively (see Fig. 2.1a). Let u, v and w be the corresponding velocity components, while u_e and v_e are the corresponding outer-flow edge velocity components and U_∞, V_∞ are the components of the undisturbed free stream. The governing equations in their dimensionless stretched form then read

$$\frac{\partial v}{\partial y} + \frac{\partial w}{\partial z} = 0 \tag{2.5.1}$$

$$v \frac{\partial u}{\partial y} + w \frac{\partial u}{\partial z} = \frac{\partial^2 u}{\partial z^2} \tag{2.5.2}$$

$$v \frac{\partial v}{\partial y} + w \frac{\partial v}{\partial z} = v_e \frac{dv_e}{dy} + \frac{\partial^2 v}{\partial z^2} \tag{2.5.3}$$

Notice that there is no pressure gradient term in Eq. (2.5.2). Moreover Eqs. (2.5.1) and (2.5.3) can be solved independently of Eq. (2.5.2). The familiar boundary conditions are

$$u = v = w = 0 \qquad \text{at } z = 0 \tag{2.5.4}$$

$$u \to u_e,\ v \to v_e \qquad \text{as } z \to \infty \tag{2.5.5}$$

Solutions to this problem were obtained by Sears (1948) for an outer flow given by

$$u_e = U_\infty \tag{2.5.6}$$

$$v_e = C_1 y + C_3 y^3 \tag{2.5.7}$$

The solution was given in the form of expansions

$$u = U_\infty \left[g_0(z) + \frac{C_3}{C_1} y^2 g_2(z) \right] \tag{2.5.8}$$

$$v = C_1 y\, f_1(z) + C_3 y^3\, f_3(z) \tag{2.5.9}$$

and the functions f_1, f_3, g_0 and g_2 were tabulated.

The rules of correspondence between points on the body of interest and the Sears problem described by Eqs. (2.5.1) through (2.5.9) require matching of the following:

a. the reduced distance S along inviscid streamlines scaled with the total length of each streamline, measured from stagnation to separation

b. the u_e velocity component,

c. the v_e velocity component and

d. the velocity gradient along the inviscid streamline

For a coordinate system x, ϕ defined on a prolate spheroid as shown in Fig. 2.1b the four conditions read

$$S = S_s \tag{2.5.10}$$

$$v_e(x,\phi) = C_1 S_s + C_3 S_s^3 \tag{2.5.11}$$

$$u_e(x,\phi) = U_\infty . \tag{2.5.12}$$

$$\frac{\partial(u_e^2 + v_e^2)}{\partial s} = C_1 + 3C_3 S_s^2 \tag{2.5.13}$$

where S and S_s are distances along the streamlines on the body of interest and the Sears body, respectively, measured from the stagnation point.

Equations (2.5.10)-(2.5.13) are solved for the quantities C_1, C_3, U_∞ and x_s. These then determine the shape of a Sears body.

Sample results are shown in Figs. 2.2, 2.3 and 2.4 for a prolate spheroid and ellipsoids respectively. In these figures are plotted the projections of lines on planes that correspond to windward views and side views. The lines that are behind the body are shown dotted. In all figures, envelopes of skin friction lines are clearly developed, thus defining the line of separation. The separation lines found are compatible with analytical predictions of open separation (Wang (1975), Patel and Choi (1979), Cebeci et al. (1981)). However, the present method is very crude for offering verification of the existence of open or closed separation. Comparison of the relative performance of this

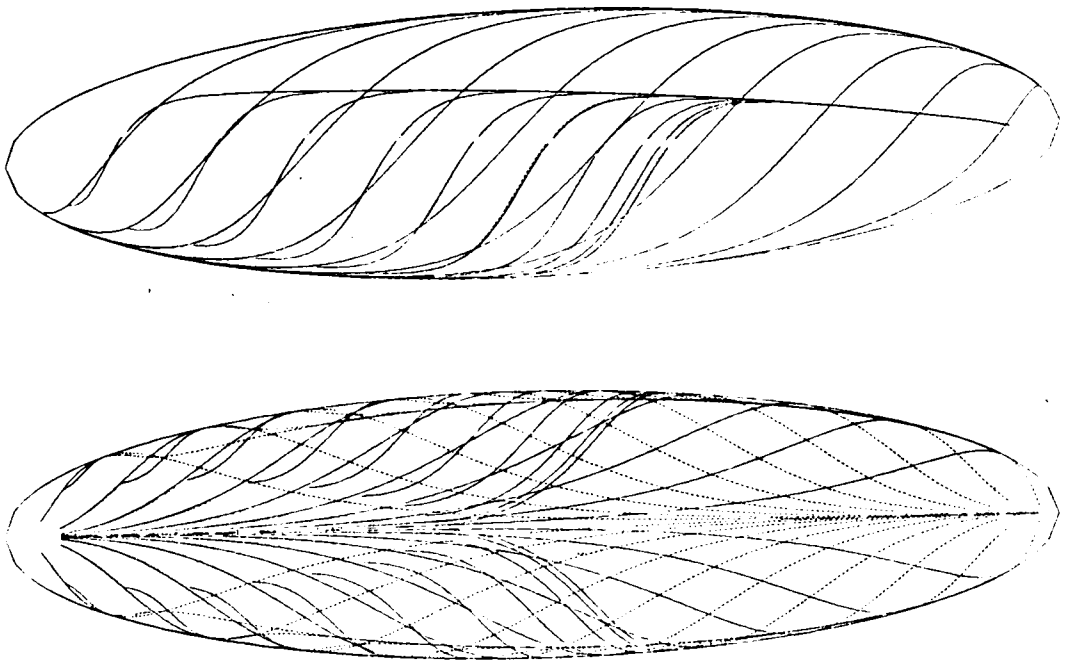

Fig.2.2 Flow about an ellipsoid with axes ratios a:b:c = 4:1:1 (prolate spheroid) at an angle of attack a = 30°.

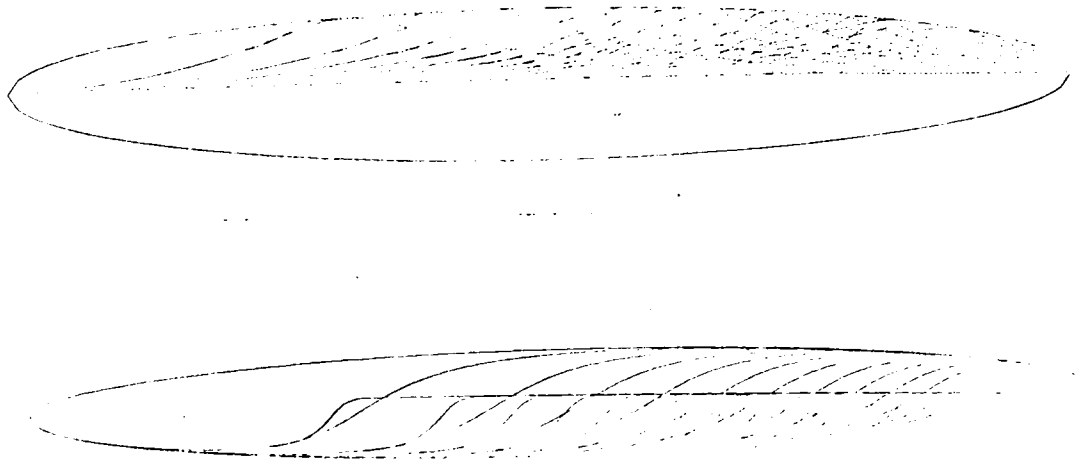

Fig. 2.3 Flow about an ellipsoid with axes ratios a:b:c = 70:10:7 and a free stream U_∞ = cos 15°, V_∞ = sin 15°, W_∞ = sin 15°.

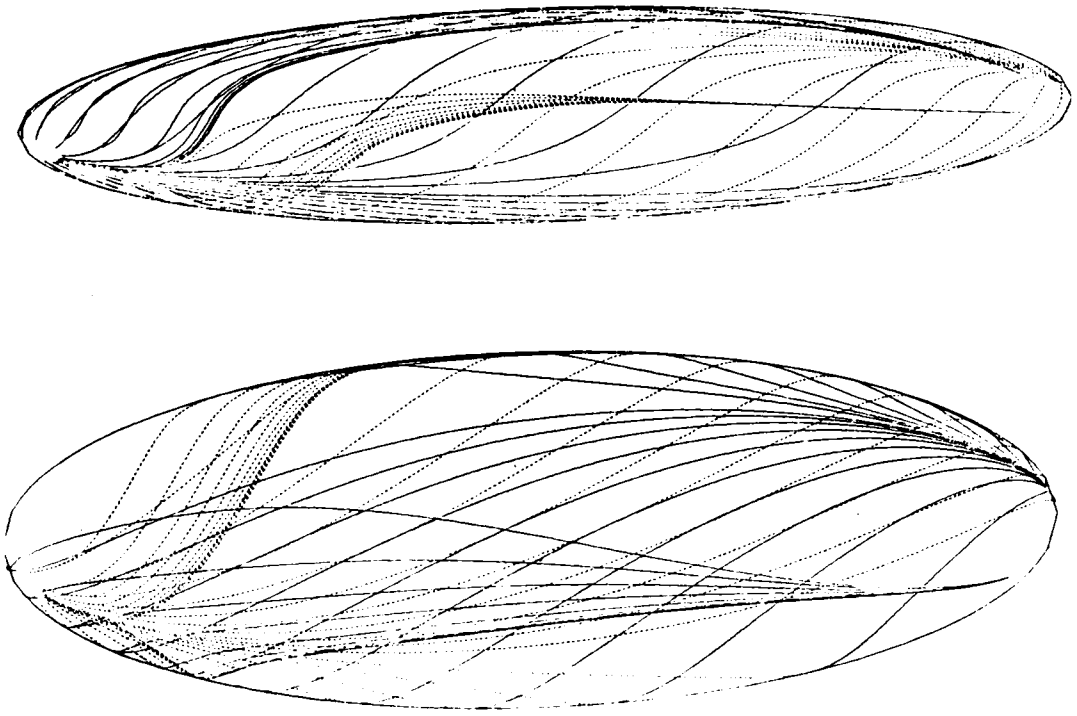

Fig. 2.4 Flow about an ellipsoid with axes ratios a:b:c = 50:30:10 and free stream U_∞ = cos 30°, V_∞ = sin 15°, W_∞ = sin 15°.

method with other methods indicated surprising agreement (Wang, 1975; Cebeci, 1982; Stock, 1980; Geissler, 1973) as reported in Telionis and Costis (1983). Examples of results for axes ratios of a/b = 2,4 and 5 and various angles of attack are plotted in Figs. 2.5, 2.6 and 2.7 respectively. The agreement of the present crude method with the methods of Stock (1980) and Geissler (1973) is surprisingly good.

Comparison with the work of Wang (1974) and Cebeci et al. (1981) is given in Figs. 2.8, 2.9 and 2.10. In Figs. 2.9 and 2.10 our estimates of the separation line as obtained from our flow visualizations are also included. For $\alpha = 6°$ no experimental data is available. However, for $\alpha = 5°$, there is no experimental evidence of closed separation. The separation line should not be continued towards the leeward side beyond the OK which Cebeci, et al. (1981) have identified.

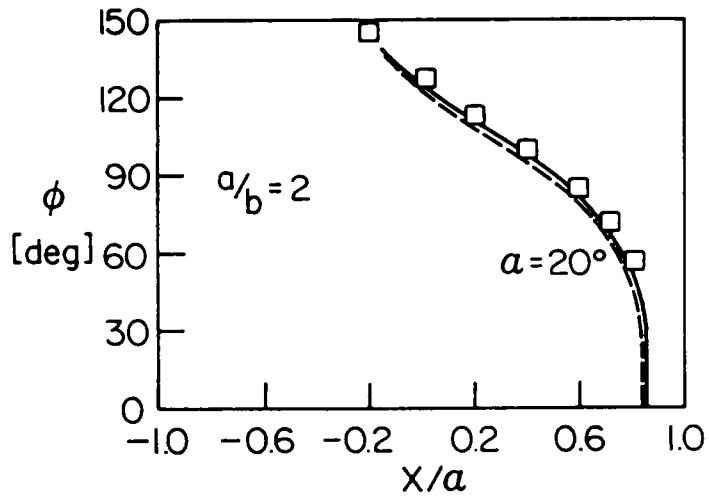

Fig. 2.5 Lines of separation for a prolate spheroid with axes ratios a/b = 2 and angle of attack a = 20°. ———, Stock[8]; -----, Geissler[19]; □, present method.

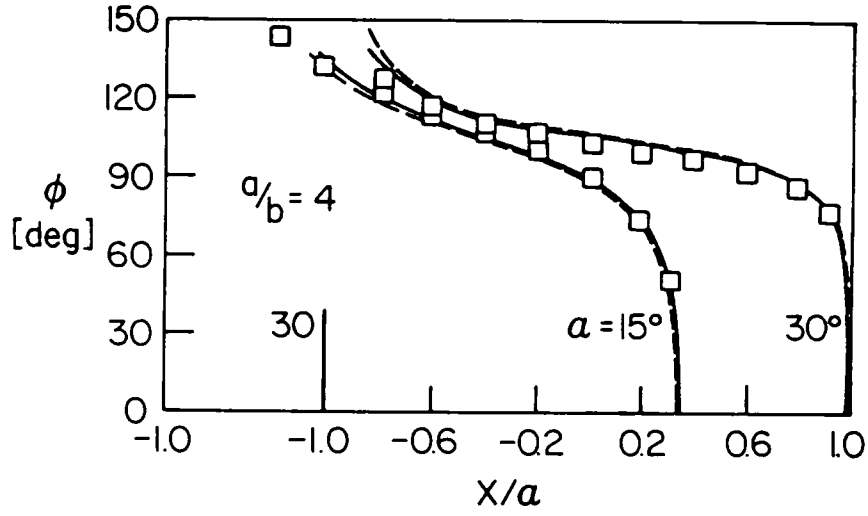

Fig.2.6 Lines of separation for a prolate spheroid with axes ratios a/b = 4 and angles of attack a = 15° and 30°. ———, Stock[8]; -----, Geissler[19]; □, present method.

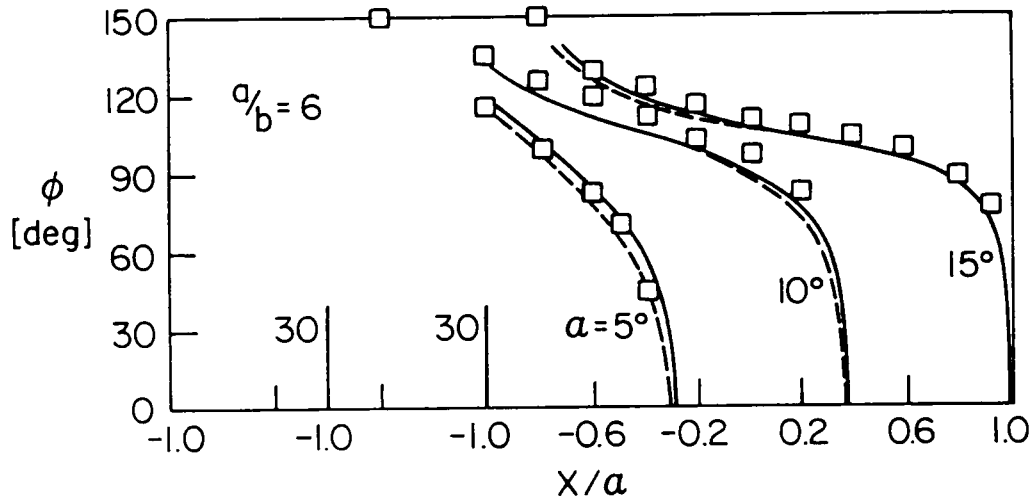

Fig 2.7 Lines of separation for a prolate spheroid with axes ratios a/b = 6 and angles of attack a = 5°, 10° and 15°. ———, Stock[8], -----, Geissler[19]; □ , present method.

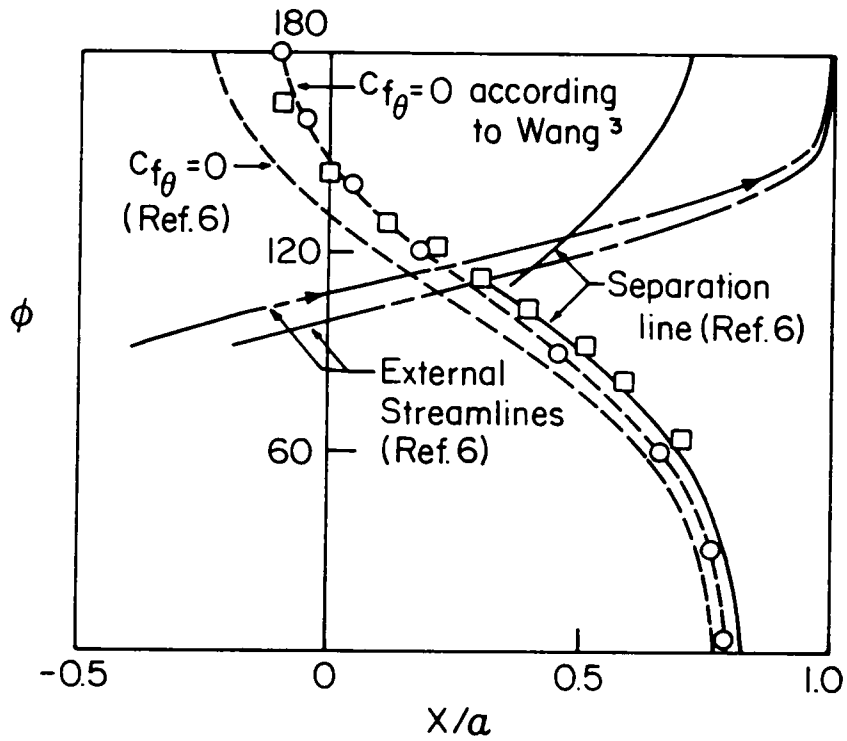

Fig.2.8 Lines of separation and external streamlines for a prolate spheroid of $\alpha/b = 6$ at an angle of attack $\alpha = 6°$. ———, Ref. 6; -----, Ref. 3; □, present approximate method.

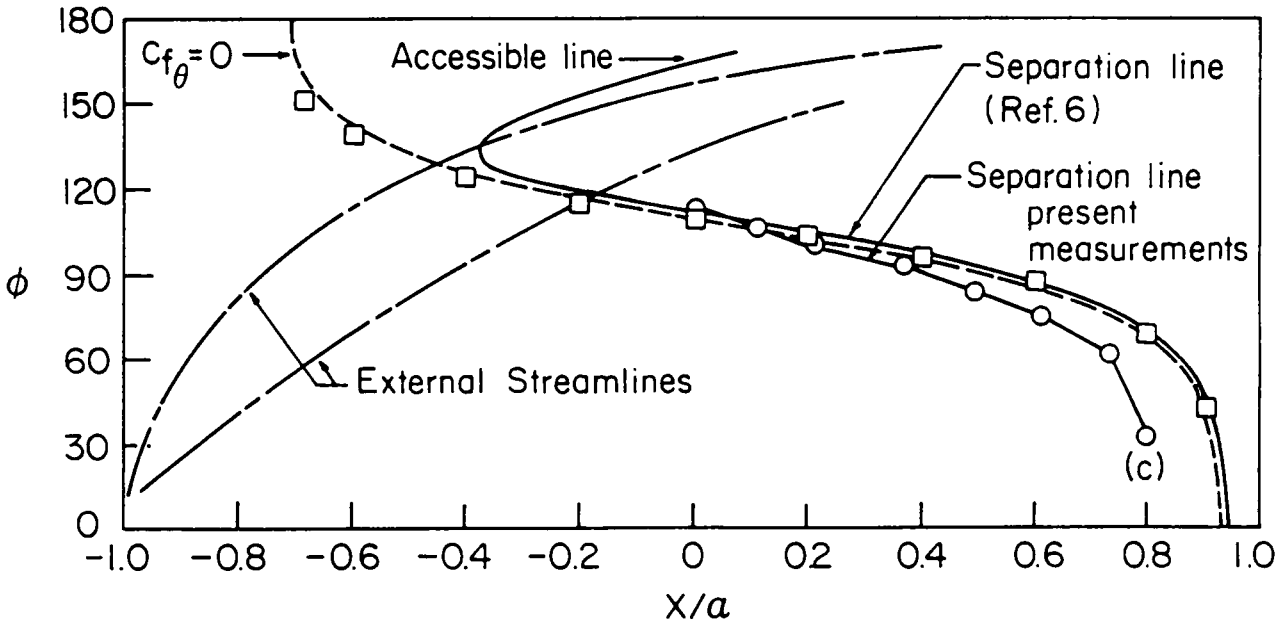

Fig. 2.9 Lines of separation and external streamlines for a prolate spheroid of a/b = 6 at an angle of attack α = 15° as reported in Ref. 6; □, present approximate method; -o-o-o-o; present experimental data.

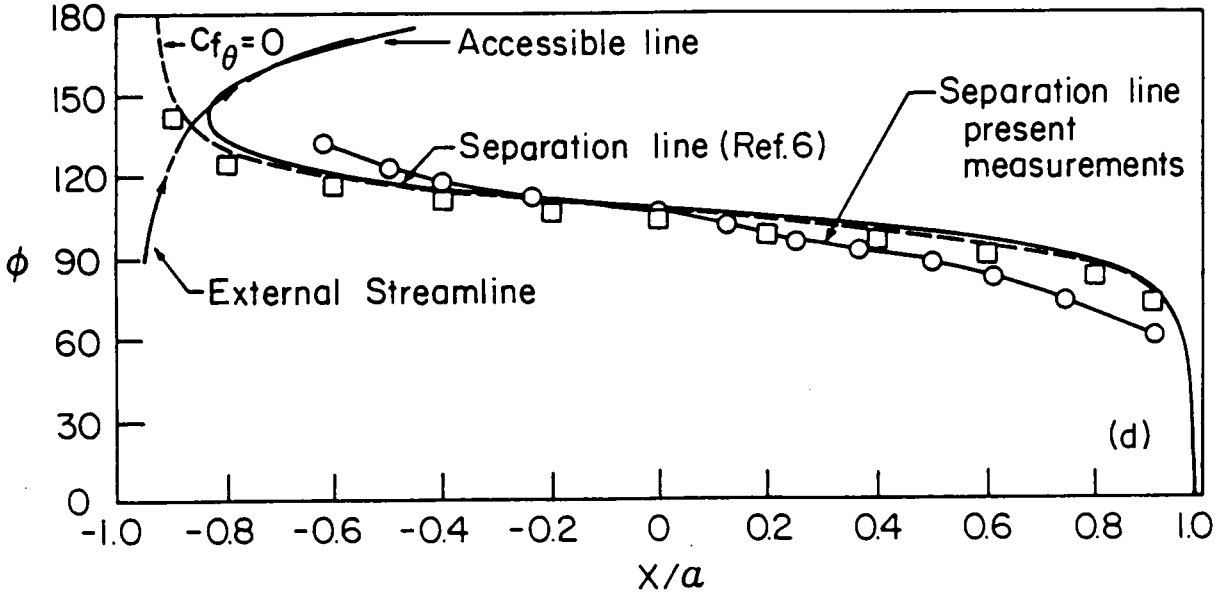

Fig.2.10 Lines of separation and external streamlines for a prolate spheroid of a/b = 4 at an angle of attack a = 30° as reported in Ref. 6; □, present approximate method; o-o-o-o-o; present experimental data.

CHAPTER III

FLOW VISUALIZATION

3.1 Introduction

Numerous visualizations of the flow have been presented on a wide variety of fluid mechanics problems (Merzkirch 1980). Using the color-dye technique, visualizations of the flow around models of air-vehicles or underwater vessels have been attempted. The patterns of separation, in connection with the limited streamlines, were visualized, although not with adequate resolution by Oudart and Eichelbrenner (1955) and by Han and Patel (1979) on prolate spheroids with axes ratios of 1 to 6 and 1 to 4 respectively. Dye injection on the surface of the body was the method of visualization in both cases. Meier et al. (1980) used oil-dot techniques for their visualization in wind tunnel for a prolate spheroid of 1 to 4 axis ratio.

The flow visualization by Meier et al. gives a clear picture of the separation pattern. However, the Reynolds number of the experiment is rather high. On the other hand, the visualizations by Oudart and Eichelbrenner (1955) and Han and Patel (1979) fail to fully indicate the skin-friction line pattern in the leeward side of the body. This is a region of interest for the numerical analysis, since most of the numerical schemes of integration fail in this region. An attempt was made here to obtain clear flow visualization pictures in the leeward side of a prolate spheroid, as well as in all other regions. A prolate spheroid of axis ratio 1 to 4 was used. The method of dye injection was

employed and the experiments were conducted in a water tunnel. Furthermore, an attempt was made to convert the flow visualization data into discrete quantitative data in the form of coordinates of points along the skin friction lines.

3.2 The Water Tunnel

A small, low-turbulence water tunnel was used for flow visualization. Fig. 3.1 shows schematically the water tunnel. An impeller was used originally for the circulation of water. Although the impeller did not create high frequency disturbances, the flow was unsteady. The unsteadiness of the flow was due to the discontinuity of the driving force exerted by the plates of the impeller.

After numerous efforts to reduce the unsteadiness by increasing the radii of the propeller or by inserting porous material in the gaps between the plates of the impeller, it was decided instead to use a mixed-flow water pump. Fig. 3.1 shows the configuration of the facility after the necessary modification. The use of the pump eliminated the organized low-frequency unsteadiness, but the direct injection of water in the tunnel, and the absence of a settling chamber lead to tremendous increase of diturbance amplitudes of all higher frequencies. Various configurations of honeycomb, screens, and foamy material were tested for the most effective way to reduce the turbulence level. Finally, the configuration shown in fig. 3.1 was chosen. A polymethylane foam was placed immediately after the exit of the water from the pump. The foam eliminated all the high frequency disturbances introduced by the abrupt injection of the water to the chamber wall of the tunnel. However,

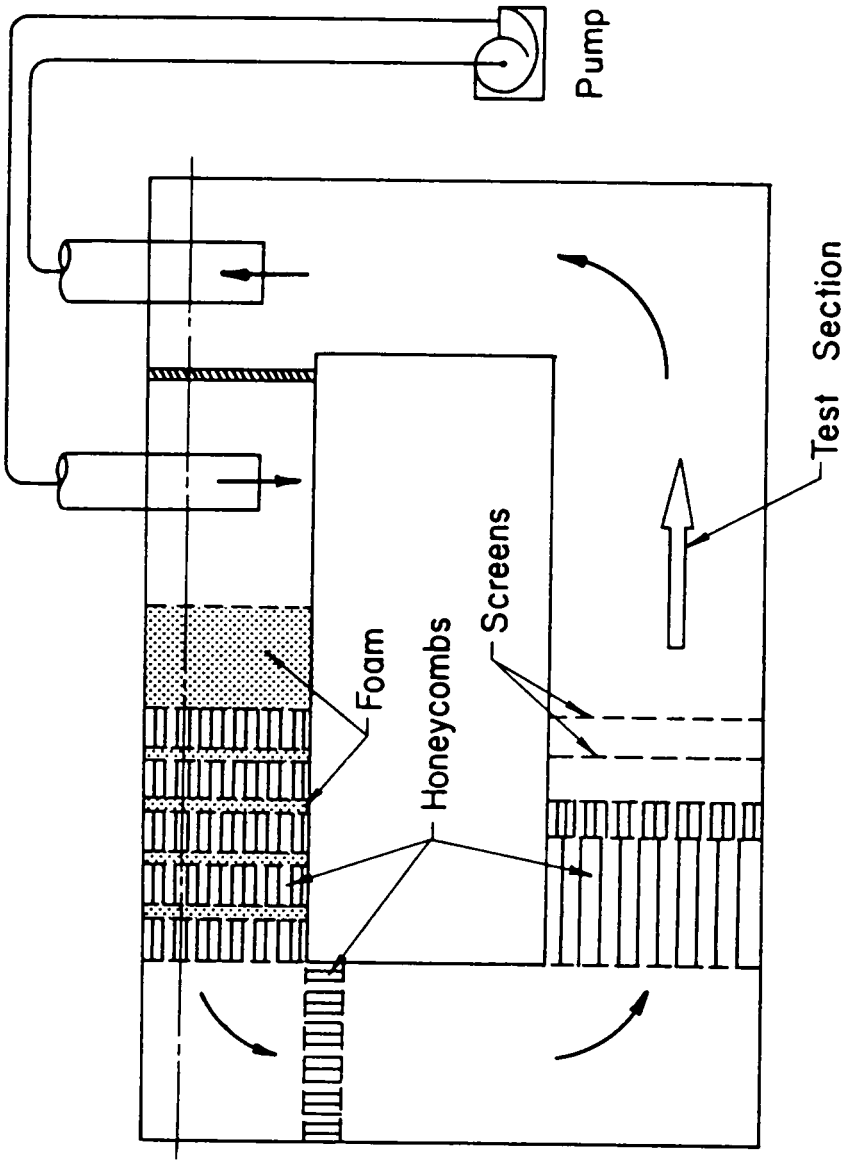

Fig. 3.1 Schematic representation of the water tunnel.

large scale vortices could not be eliminated using the foam. A sequence of honeycombs and plastic porous materials were placed downstream of the foam and prior to the test section to eliminate the large scale vortices. Finally, immediately before the test section, two screens were placed to reduce the high-frequency turbulence introduced by the honeycombs.

Figure 3.2 shows a spectrum of the flow after the aforementioned means for turbulence reduction were placed. The velocity was obtained by a one-channel LDV system and the signal was analyzed in the frequency domain by a FFT digital machine. The turbulence level was measured by a RSM voltmeter (Schlumberger). A disturbance frequency at 17 Hz appeared at the first run. It was found that the disturbance was created by the water pump and transmitted to the flow through the return pipe connecting the tunnel to the intake of the pump. Isolating the tube with rubber material resulted in a considerable decrease of the amplitude of this frequency. The turbulence level was finally reduced with this arrangement to about 0.4% at 4 cm/sec. Freestream velocities were achieved with the disturbances mainly concentrated around low frequencies. For speeds over 4 cm/sec, the design is not adequate to insure high quality flow. Based on the length of the body, the Reynolds number at this speed is about 2000, which along with the low turbulence level guarantees laminar flow all along the surface of the model.

3.3 The Model

The body chosen for the study of streamline pattern was a prolate spheroid with axis ratios of 1 to 4. The model was machined out of

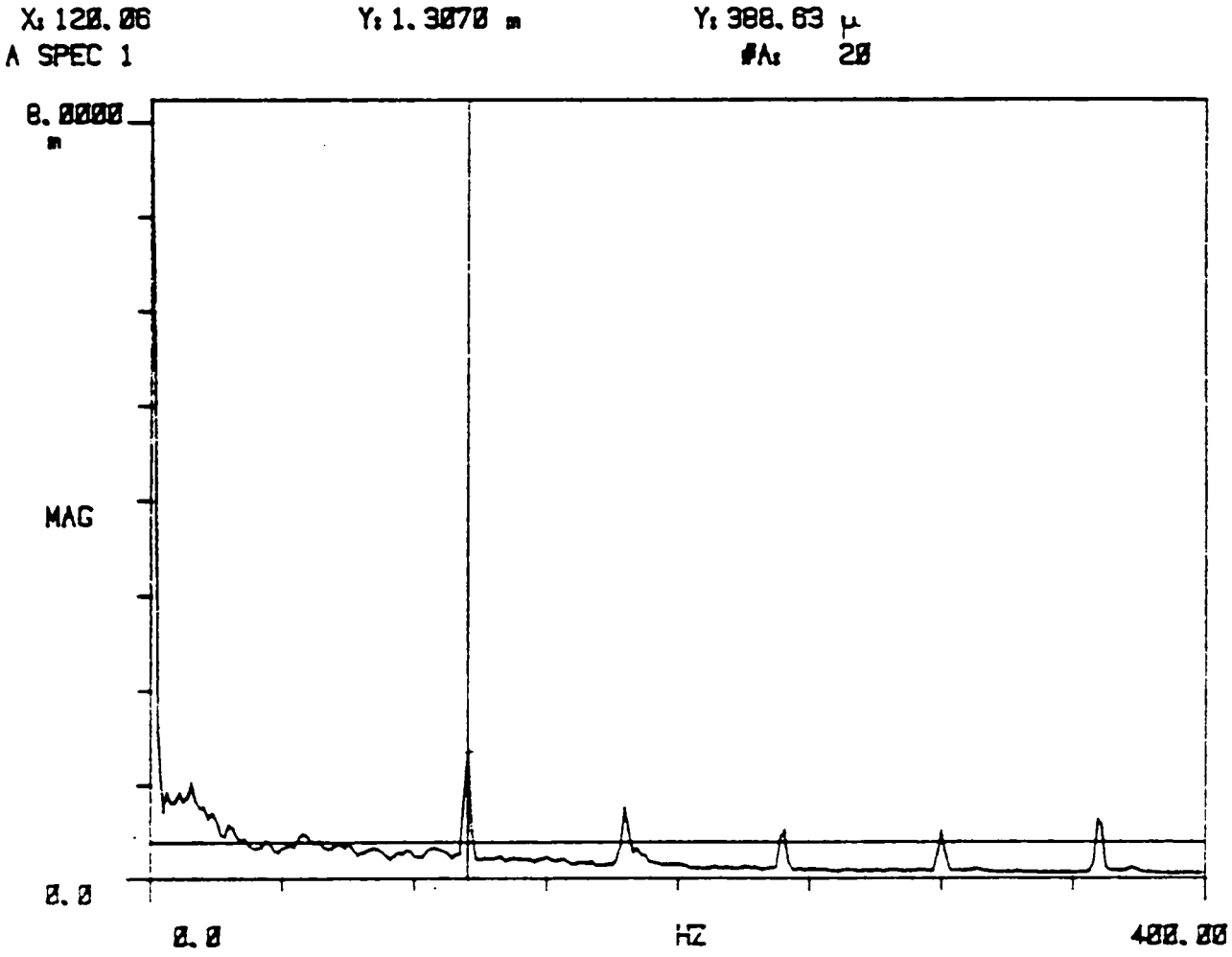

Fig. 3.2 RMS spectrum of the velocity fluctuation. If the low frequencies (less than 4 Hz) are eliminated, then the turbulence level is less than 0.1%. The spikes in the spectrum correspond to the 60 Hz and its multiples and are due to the power supply.

aluminum. Aluminum was selected because it is easy to be machined and smoothed. The length of the model was 8 inches. The model was hollowed and was mounted by a strut from the one end. Dye ports were drilled at six points on the model. Three of them were drilled near the front nose and the other three were drilled at about the middle of the model. Two small flexible hoses supplied color dyes at every drilled port. Color dyes were released at the surface of the model. Dyes were also released at a small distance above the surface of the body. This was achieved by mounting hypodermic needles with heights approximately equal to the anticipated thickness of the boundary layer. In this way, skin-friction lines and inviscid streamlines, emanating from the same stations on the surface can be compared. Hypodermic syringes were used to supply the dyes and control the exit pressure. Cloth and food color-water solutions were used as dyes. Color photographs were taken from views corresponding to approximate inclinations θ = 0°, 90°, 120°, and 180°. These correspond to windward, side, oblique, and leeward views respectively. A mirror was used for the leeward view.

3.4 Skin-Friction Line Visualization

Experiments were conducted for angles of attack α = 3°, 6°, 10°, 15°, 20° and 30°. The results confirmed the fact that for very low and very high angles of attack, here for α = 3° and for α > 30°, the line of separation is closed around the body. In this case, two critical points can be identified on the line of separation and the general pattern fits nicely one of the models described by Maskell (see discussion in Wang,

1975), namely the bubble model. This in the more common terminology is the case of closed separation.

In Figs. 3.3 - 3.6 we display flow visualizations of different views of the flow about a prolate spheroid at angles of attack of 3°, 6°, 10° and 20°, respectively. In Fig. 3.3, a well-behaved closed separation pattern is identified in agreement with all analytical predictions.

For angles of attack $6° \leq \alpha \leq 30°$ the evidence clearly indicates that there are two lines of open separation. However, details of the flow uncovered for the first time here shed light to controversial interpretations of earlier numerical results. For this range of angles of attack, it appears that the basic skin-friction line pattern is qualitatively the same. Three distince regions difficult to be accessed by the freestream become quickly apparent and may be erroneously interpreted as regions of separated flow. The first region is covering the lee side and appears dark in the top view of Fig. 3.5. It should be emphasized that all the darkened area in this figure is due to dye that has been emitted at only one port in the front part of the model. In the same figure the two lighted areas on the two sides in the aft of the body are strongly suggesting the existence of two separated regions. The pattern could be sketched approximately as in Fig. 3.7. The two side lobes would then appear to have the shape described by Cebeci et al. (1981).

What has been known for a long time is that, in fact, the flow remains attached on the leeward plane of symmetry and in its neighborhood. This is corroborated by the fact that the dye stays on

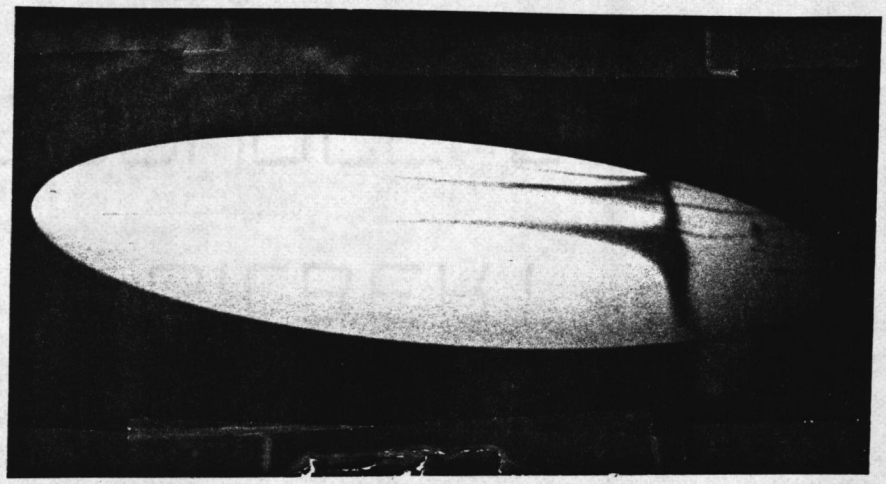

(a)

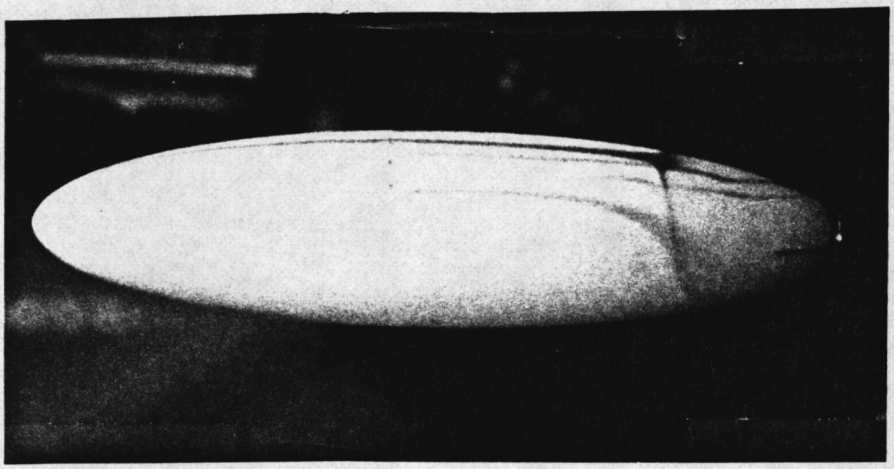

(b)

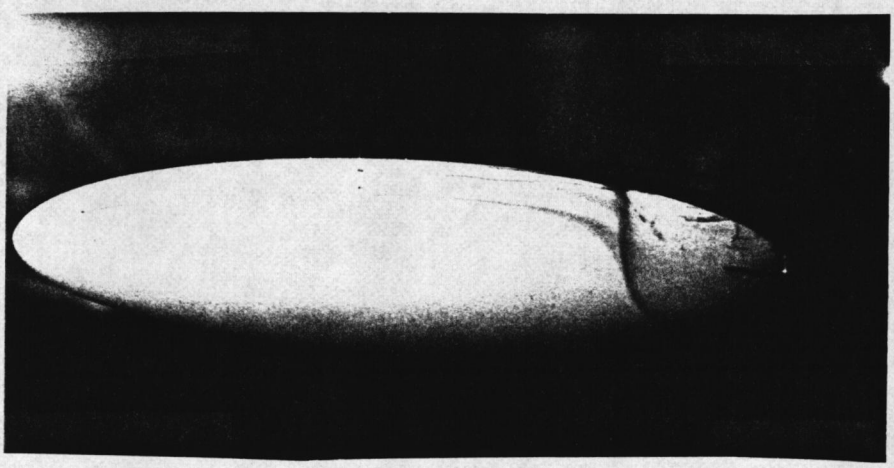

(c)

Fig. 3.3 Skin friction lines for $\alpha = 3°$. (a) Leeward view, (b) View from $\phi = 120°$, (c) Side view.

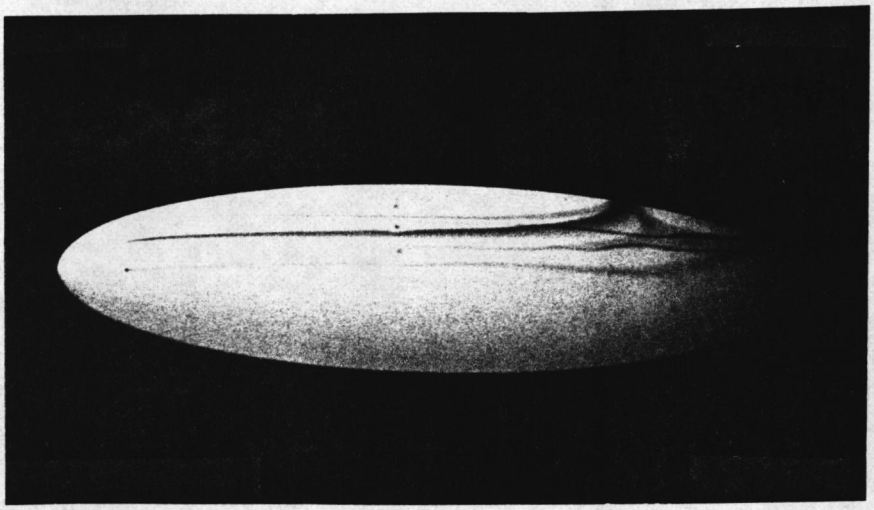

(a)

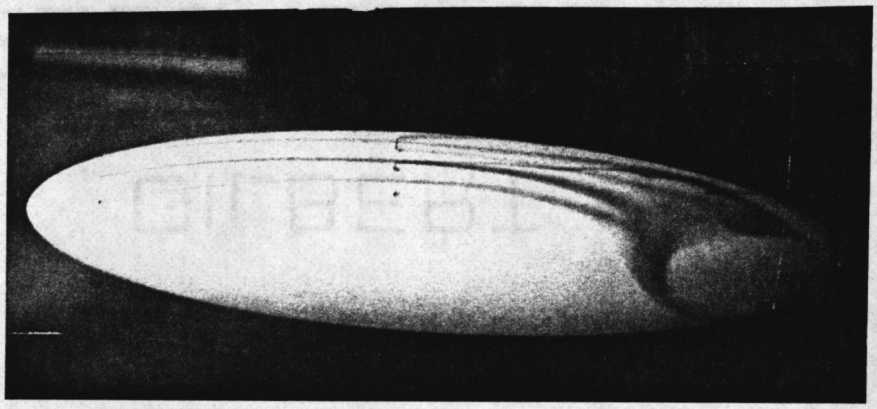

(b)

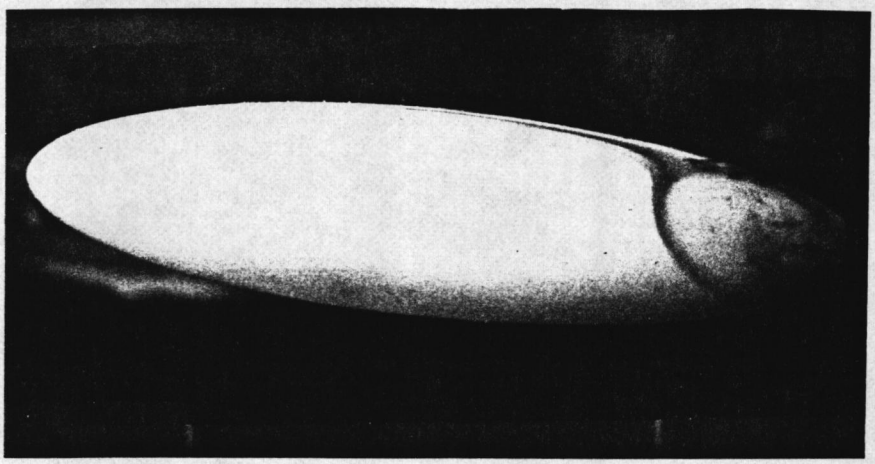

(c)

Fig. 3.4 Skin friction lines for $\alpha = 6°$. (a) Leeward view, (b) View from $\phi = 120°$, (c) Side view.

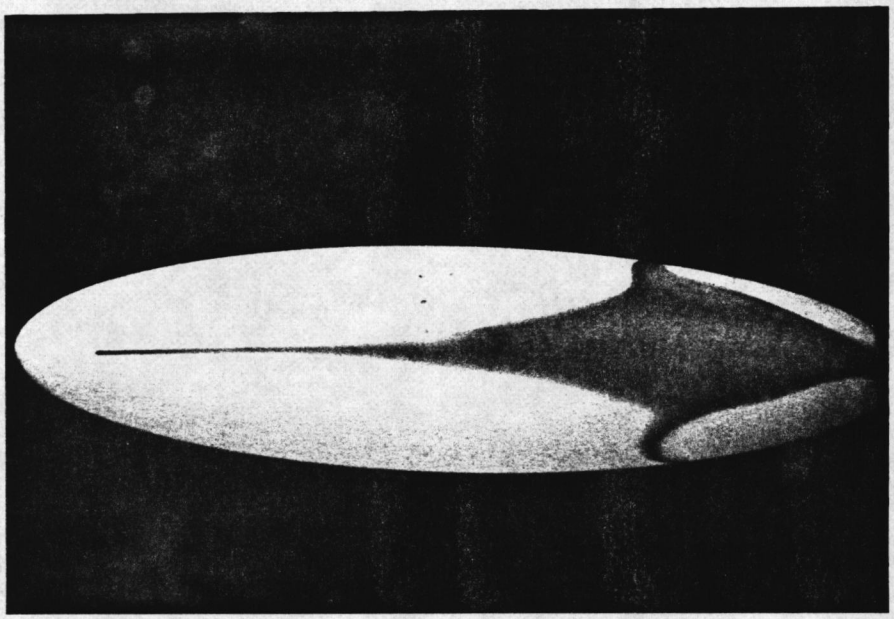

(a)

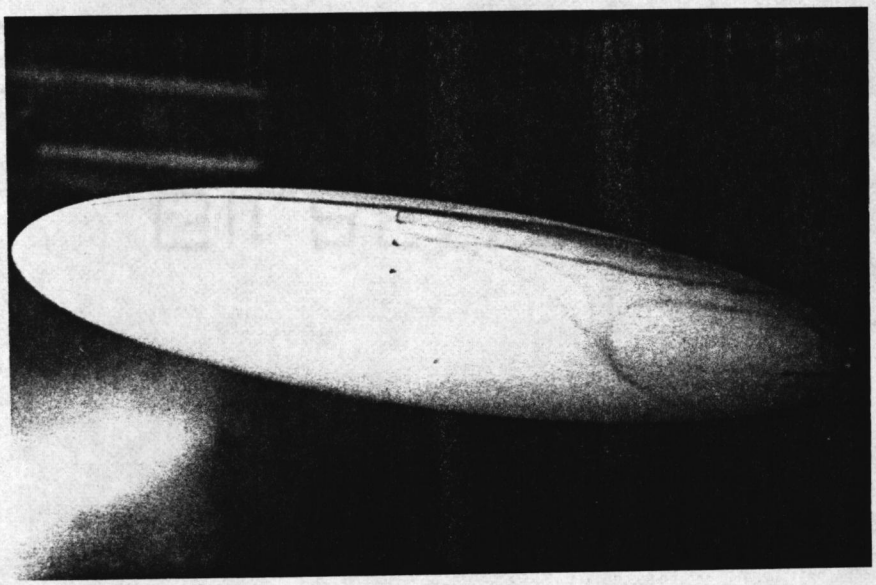

(b)

Fig. 3.5 Skin friction and inviscid lines for $\alpha = 10°$. (a) Leeward view, (b) View from $\phi = 120°$.

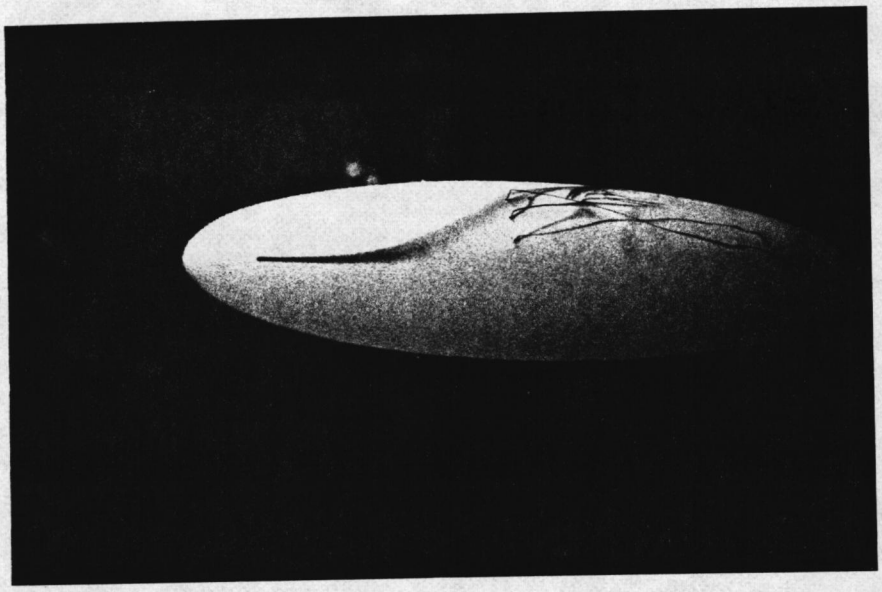

(a)

(b)

Fig. 3.6 Skin friction and inviscid lines for α = 20°. (a) Leeward view, (b) View from ϕ = 120°.

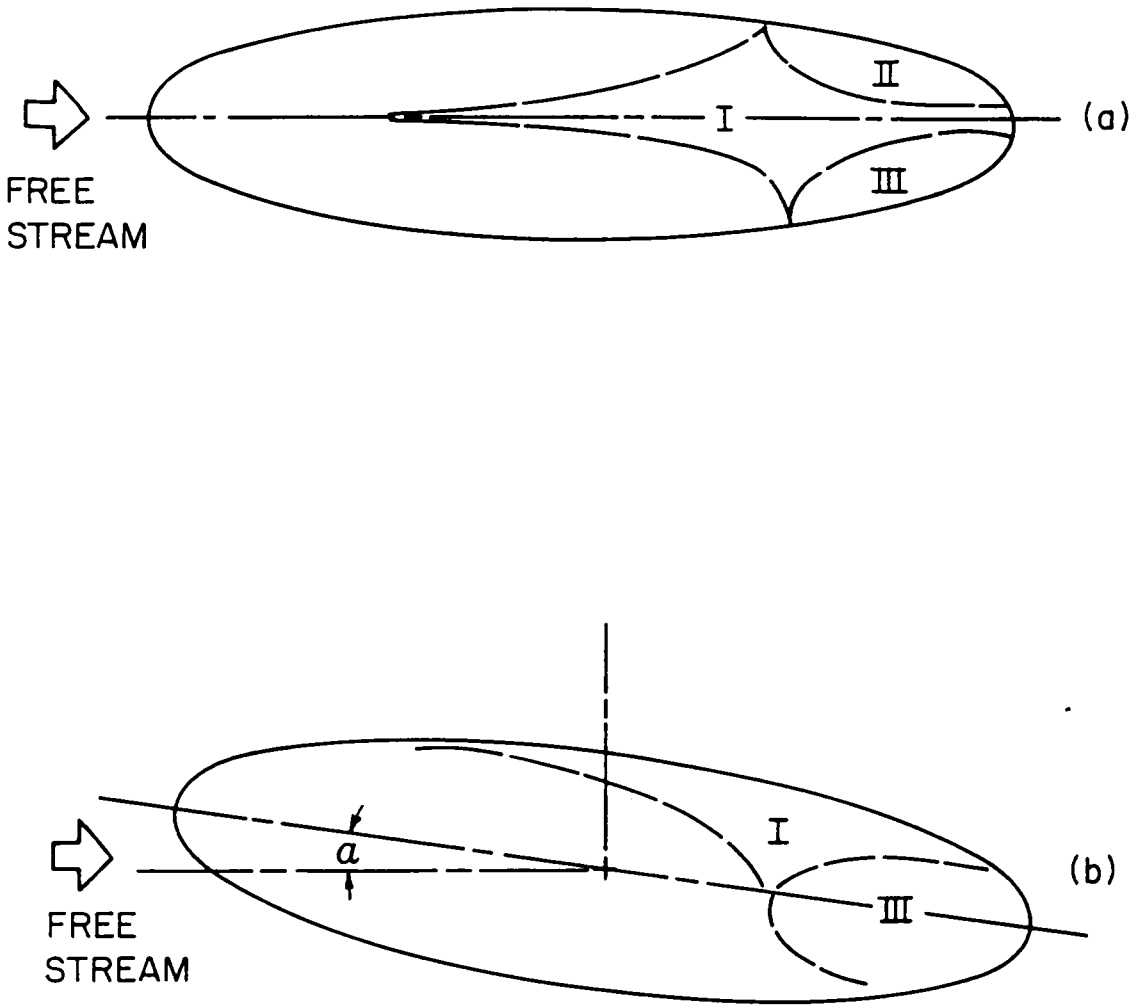

Fig. 3.7 The three regions of difficult accessibility for $\alpha = 10°$.
(a) Leeward view, (b) View from $\phi = 120°$.

the wall until it reaches the small mount at the aft of the body. However, our evidence indicates that what appear as side-separation lobes are actually regions of incredibly large cross flows. This is shown more clearly in Fig. 3.8. In this figure the inviscid streamlines as well are marked by dyes released at the edge of the boundary layer.

A very large number of flow visualizations obtained point very clearly to a pattern of viscous streamlines shown in Figs. 3.9 and 3.10 for α = 10° and 20°, respectively. These patterns have been drawn carefully by an artist who traced the edges of the dye lines from a large number of flow visualizations.

Our evidence as shown in Figs. 3.4-6 and the interpretations shown in Figs. 3.9 and 3.10 indicates that for these angles of attack, the separation line is of the open type. In fact, the dyes lift off from the body only along the envelope of the skin friction line. This has been observed by the present investigators, but so far it appeared difficult to photograph except in Fig. 3.8. However, the inviscid streamlines of Figs. 3.6 and 3.8 also indicate that the inviscid streamline in the neighborhood of the separation line lift off by a rather large angle with respect to the body.

In view of this evidence, we feel that Cebeci et al. (1981) simply reached or rather came very close to the point of zero axial shear stress when they were forced to abandon their integration on the leeside of the body. This possibility was already identified in their presentation. Apparently, the locus of such points may be impossible to pass over with conventional numerical schemes or, in their terminology, such flows are "incalculable." Evidence from the flow visualizations

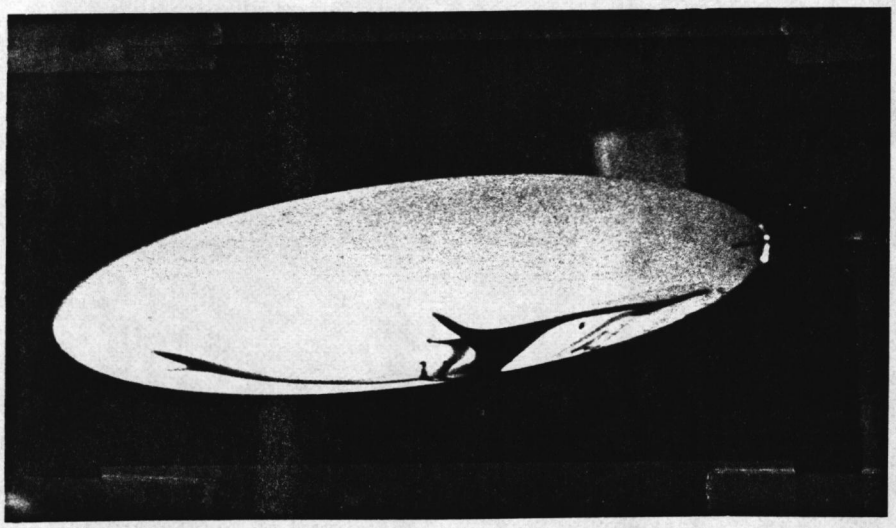

(a)

(b)

Fig. 3.8 Skin friction and inviscid lines for $\alpha = 30°$. (a) Leeward view, (b) View from $\phi = 120°$.

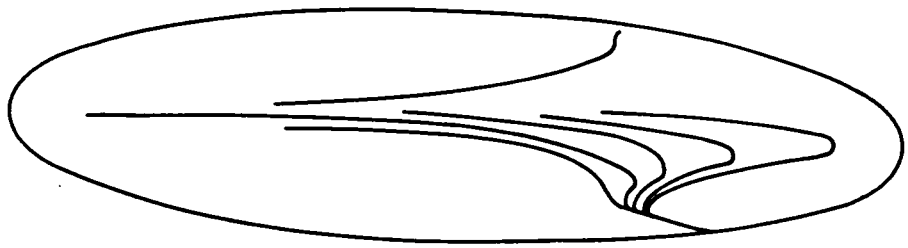

(a)

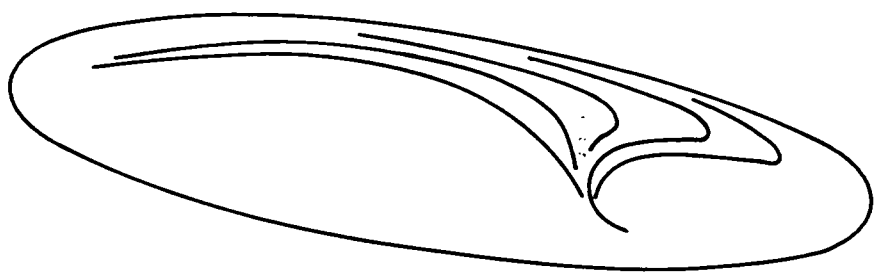

(b)

Fig. 3.9 Approximate form of skin friction lines for $\alpha = 10°$.
(a) Leeward view, (b) View from $\phi = 120°$.

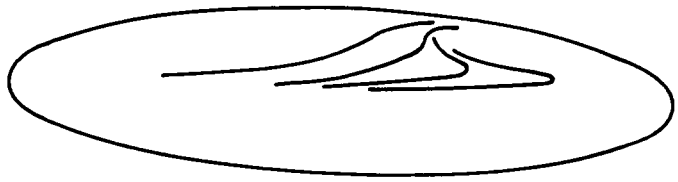

(a)

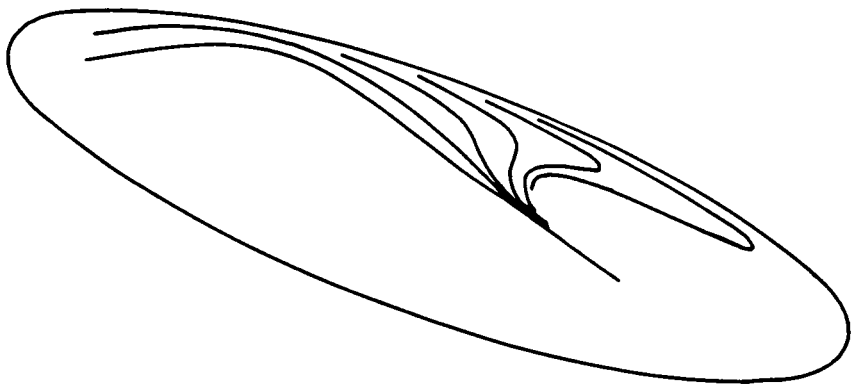

(b)

Fig. 3.10 Approximate form of skin friction lines for $\alpha = 20°$.
(a) Leeward view, (b) View from $\phi = 120°$.

presented here as well as the very large number of data which are not included, indicate that in this region the crossflow angles may reach values of the order of 150°. It is our strong conviction that in the case studied by Cebeci and his co-workers, the skin-friction lines have the qualitative pattern shown in Fig. 3.11.

3.5 Vortex Sheet Visualization

Flowfield visualization is of common use in 2-D flow experiments. Particles in the flow or color dyes can provide useful information on the flowfield. However the visualization and most importantly, photographic documentation of 3-D flowfields is not an easy task. Particles in the flow cannot be used, since the ones in the undistrubed stream may be confused with the ones affected by the presence of the body. Moreover a 2-D picture cannot depict the three-dimensional flow pattern. On the other hand, color dyes may give a general picture of the flow, but quantitative conclusions on the geometry of the flow cannot be derived easily.

In the present study, dye injection could offer limited information about the external flow over the prolate spheroid. A special method was then invented which provides useful qualitative information and has the potential to generate quantitative information as well. The method was found to be particularly successful for the prolate spheroid under an angle of attack.

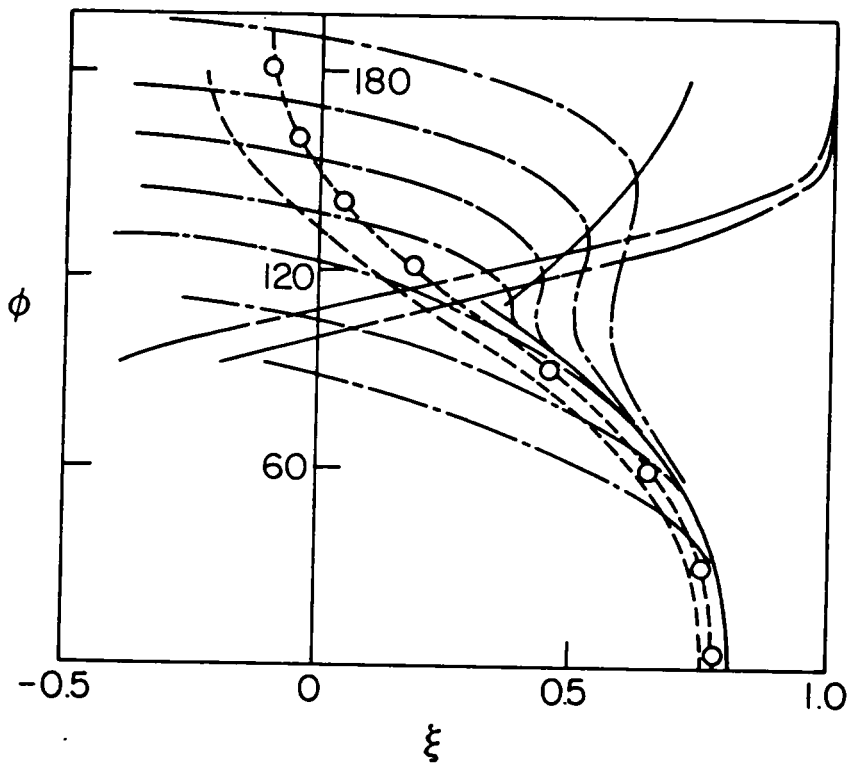

Fig. 3.11 Qualitative shape of skin-friction lines superimposed on a figure from Cebeci et al. (1981). _____, line of accessibility; ___ _ ___, inviscid streamline, Cebeci et al. (1981). __ _ __ _; skin friction lines conjectured by the present author.

It was found during the skin-friction line experiments that color dye injected from a part located on the upper meridional plane and in the front part of the body can reach any point of the external flow immediately above the lines of separation. The fact that dye injected in the flow from one point is dispersed in such a way that an entire region can be visualized is a feature of the external flow about the prolate spheroid. It cannot be stated that every 3-D body has the same feature. The colored dye, itself, cannot provide any quantitative information of the external flow, due to reasons discussed in the previous paragraph. Injection of particles is useful to visualize the direction of flow, but the information cannot be depicted in a 2-D picture. The technique that has been developed made use of laser velocimetry seeding and planes of laser light. Cross-sections of vortex sheets were thus generated.

A solution of laser-velocimetry seeding in water was injected from the port located in the upper meridional plane and in the front part of the body. The seeding consisted of 1 u silicone carbide particles which scatter the laser light. The solution injected at specific pressure reaches every point on the separation line and therefore lifts off and follows exactly the shape of the vortex sheets bounded by the two separation lines.

A laser beam is expanded into a plane of light by means of a cylindrical lens. The plane of light is positioned at various axial distances, perpendicular to the model axis. The particles in the lighted plane scatter the light strongly and thus two-dimensional cross sections of the separated vortex sheets can be clearly visualized. With

the plane of light directed normally to the main axis of the spheroid, the 2-D cross section can be used for the quantitative results to be concluded.

Pictures of cross-sections of the separated vortex sheets using the aforementioned method are presented in Figure 3.12 for 30° angle of attack and Re = 11700. It was found that the pattern of flow remains unchanged for Re up to 45000. However, this value may be a limit of our water tunnel, since a further increase of the freestream velocity is accompanied by a sharp increase of the turbulence level. The reason for that increase is the fact that in order to achieve higher speeds, the foam was removed, leaving only the honeycombs and the screens to reduce the turbulence level. It is very possible that a water tunnel with low turtulence level at high freestream speeds will be able to maintain laminar high quality flow and wake for Re above 45000.

Figures 3.12 presents side views of the cross-section while Fig. 3.13 presents the same laser cuts as viewed from directly downstream of the model. Figure 3.14 presents skin friction lines superimposed on the cross-sections of the external flow. Finally Fig. 3.15 presents a schematic but accurate picture of the external flow and streamline pattern, as obtained by the present flow visualization data.

The skin-friction line patterns indicate the presence of two side 'lobes.' These were denoted as regions II and III in Fig. 3.7. Using the external flow visualization technique it was found that the upper and lower boundaries of those lobes are actually separation lines. Two free-shear layers emanate from those separation lines in a direction almost tangent to the surface of the body. Fig. 3.13 shows clearly the

Fig. 3.12 Laser cuts of separating vortex sheets at different axial locations for a spheroid at $\alpha = 30°$.

Fig. 3.13 View from downstream of the field of Fig. 3.12.

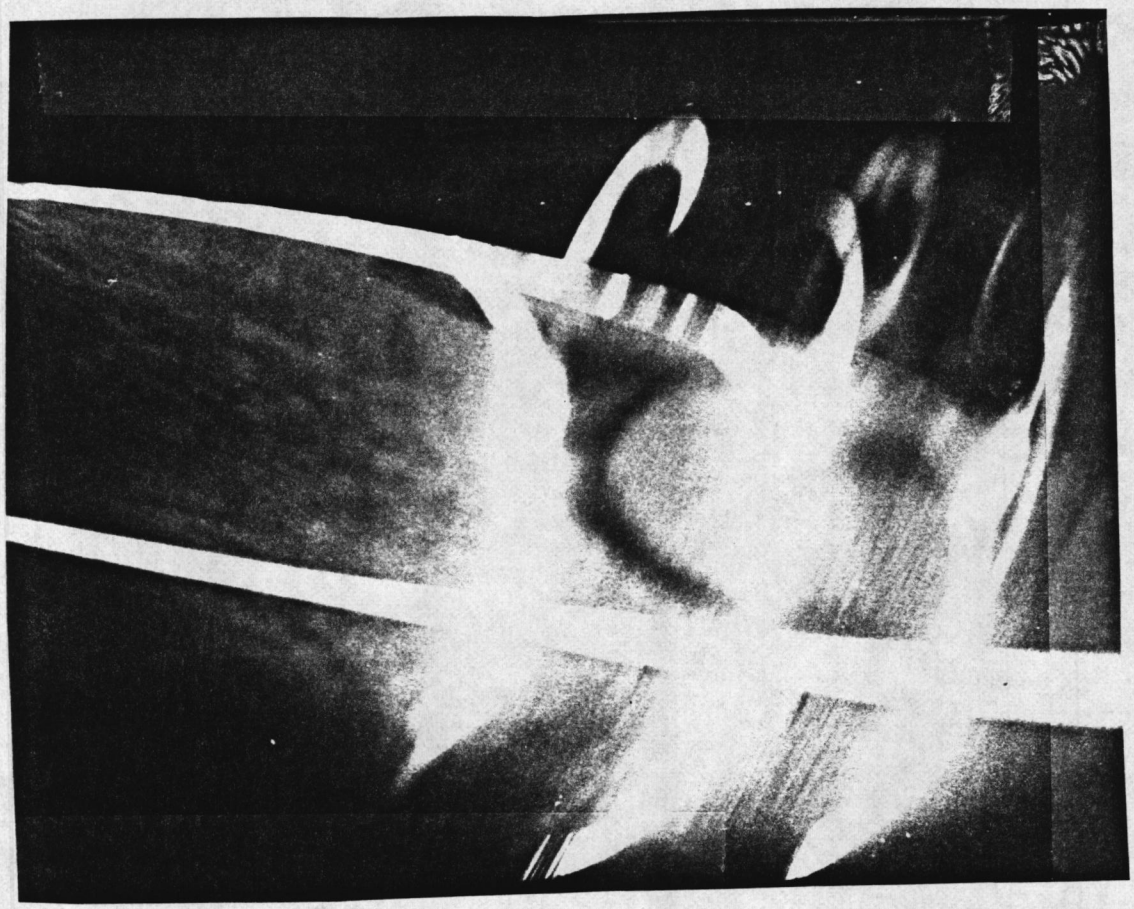

Fig. 3.14 Composite flow visualization of skin friction lines with vortex sheet cuts.

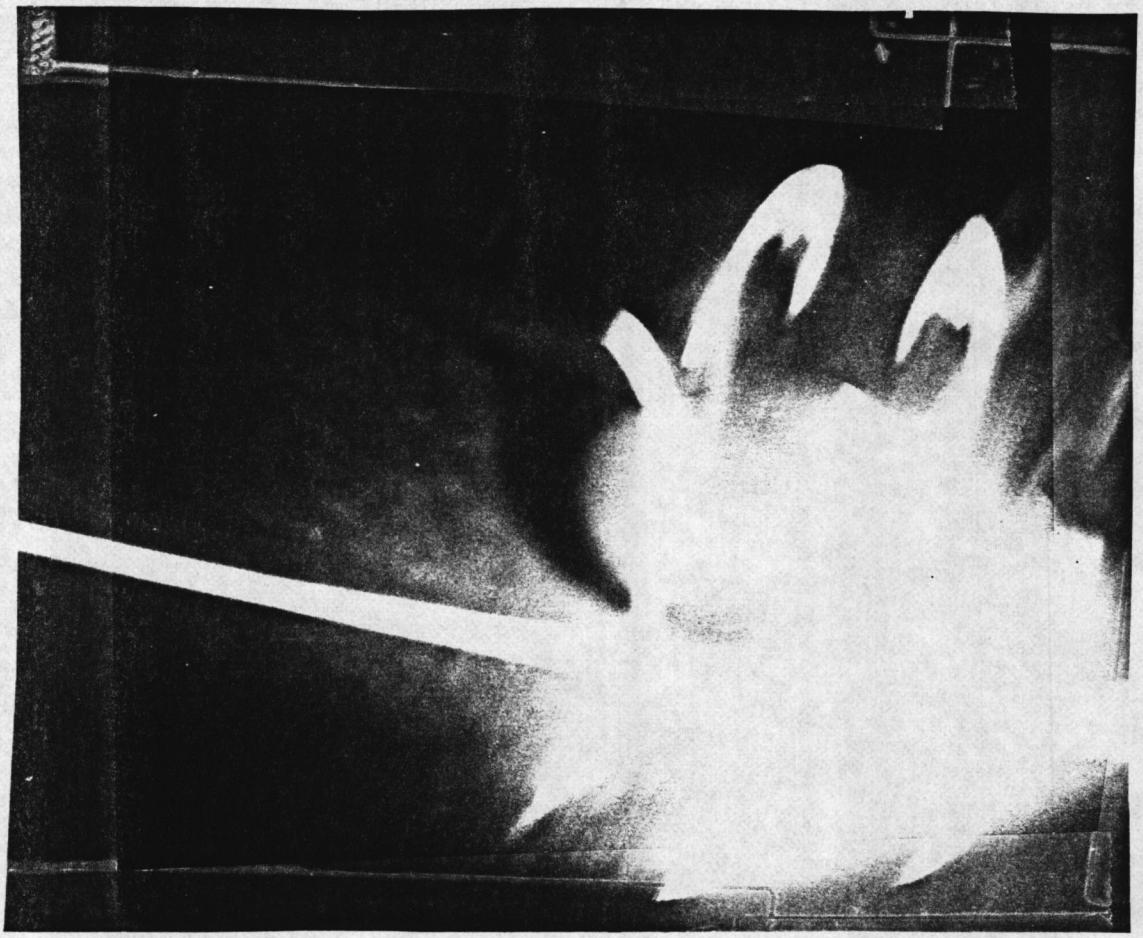

Fig. 3.14 (contd.)

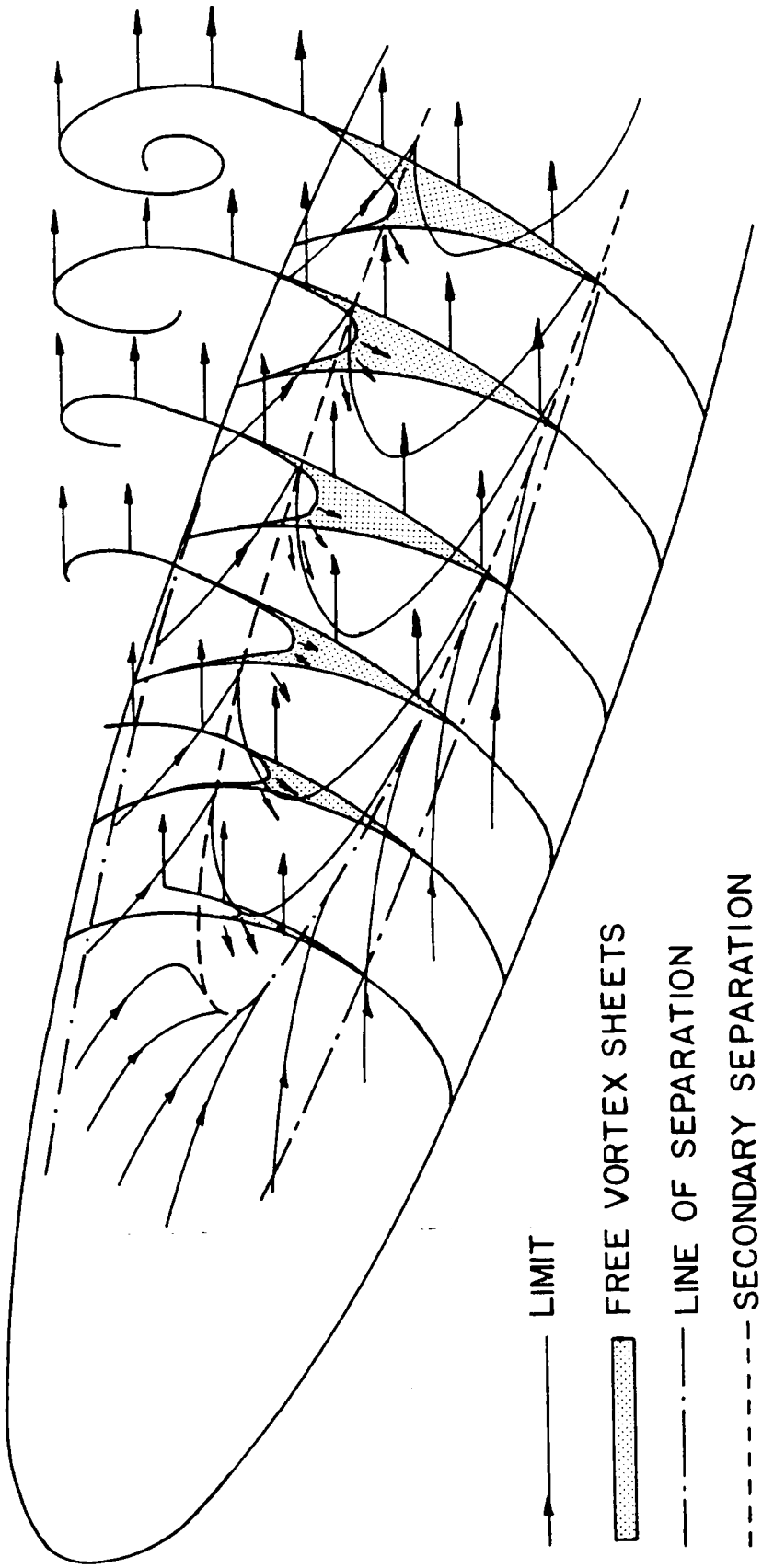

Fig. 3.15 Schematic Representation of the skin friction lines and vortex sheets as obtained by flow visualization.

two shear layers. However only in the lower boundary of the lobes the separation line is formed in the accepted way, that is by means of converging streamlines from both sides of the line. The separation line of the upper boundary of the lobes reveals an entirely new topography of skin friction and separation lines on a 3-D body. Skin friction lines converge to the upper boundary of the lobes moving in the direction of the flow and approaching the boundary. However the skin-friction lines inside the lobes move away from the upper boundary and in the opposite direction than the free stream. The upper boundary of the 'lobes' which is a line of secondary separation is also a line of incredibly strong reversing of the flow, approaching a 360° turn.

The 'lobe' is a region of recirculating motion of fluid particles, bounded by the two shear layers. The front part of the 'lobes' has very small thickness but very soon the two shear layers become curvilinear space boundaries which form a curvilinear triangle, the cross section of the flow region of the 'lobes.' These curvilinear triangles are shaded in Fig. 3.15.

It is obvious that using a boundary-layer code the regions of the flow, inside the lobes cannot be calculated. This is not only because of the strong reversal of the flow in the upper boundary, but also because of the separating shear layers in the boundaries of the 'lobes.' Even solving the full N-S equations may be a difficult problem, because of very sharp changes of both magnitudes and directions of the flow properties in regions which are not known a priori. Vorticity and hybrid methods may be most appropriate for the solution of the problem.

CHAPTER IV

VELOCITY MEASUREMENTS

4.1 Introduction

Experimental data for the case of a prolate spheroid at incidence are given by Meier et al. (1980) who studied the flow over a prolate spheroid of axis ratio 1 to 6 in a wind tunnel at various high Reynolds numbers. They determined the wall shear stress using a specially constructed probe. Meier and Kreplin studied the transition for the flow about the model and presented flow visualization pictures revealing the skin-friction line pattern. Using a specially constructed three-hole probe they studied the boundary-layer development (1980), as well as the developing vortex flow over the prolate spheroid (1981). Their experimental techniques were greatly simplified by the axisymmetry of the body.

Ramaprian and Patel (1981) obtained detailed information on three-dimensional velocity profiles using also a three-hole probe, but for the case of a rather arbitrarily defined body of revolution. For that body, which was a combination of hemisphere and half prolate spheroid, other features of the flow were also obtained. Numerous experimental data have been obtained for 3-D boundary-layer flows. However, the work of Meier's group offers an excellent benchmark case for the study of the boundary layer in connection to separation in three dimensions.

Laser-Doppler Velocimetry has not yet been used in measuring three-dimensional boundary-layer flows. Moreover, with the exception of Meier's group, who measured velocities with three-hole probes, and only at 2 axial positions, no one has measured velocity profiles on a prolate spheroid.

The present effort employs for the first time a noninvasive method, the Laser-Doppler Velocimeter to measure 2 components of the velocity at many stations and many meridional locations over a prolate spheroid. The present study provides useful information to analyticians who encounter great difficulties in the leeward side of a prolate spheroid at an angle of attack.

4.2 The Design of the Optical Arrangement

The basic consideration for the design of the data acquisition system is that at least two components of velocity are needed in a three-dimensional boundary layer. These components must be parallel to a plane tangent to the body surface at the point of interest. It is also necessary that the measuring volume be allowed to approach the wall without blockage of any of the beams by the model. To meet these requirements, three laser beams were generated in the same plane as shown in fig. 4.1. With proper polarization of these beams, it is possible to receive scattering signals from beams 1 and 2, and 2 and 3 respectively, In this way, the components of the velocity in the directions normal to the bisectors can be obtained.

One limitation is imposed when moving the plane of the beams. The central beam, that is laser beam 2 must be always perpendicular to the

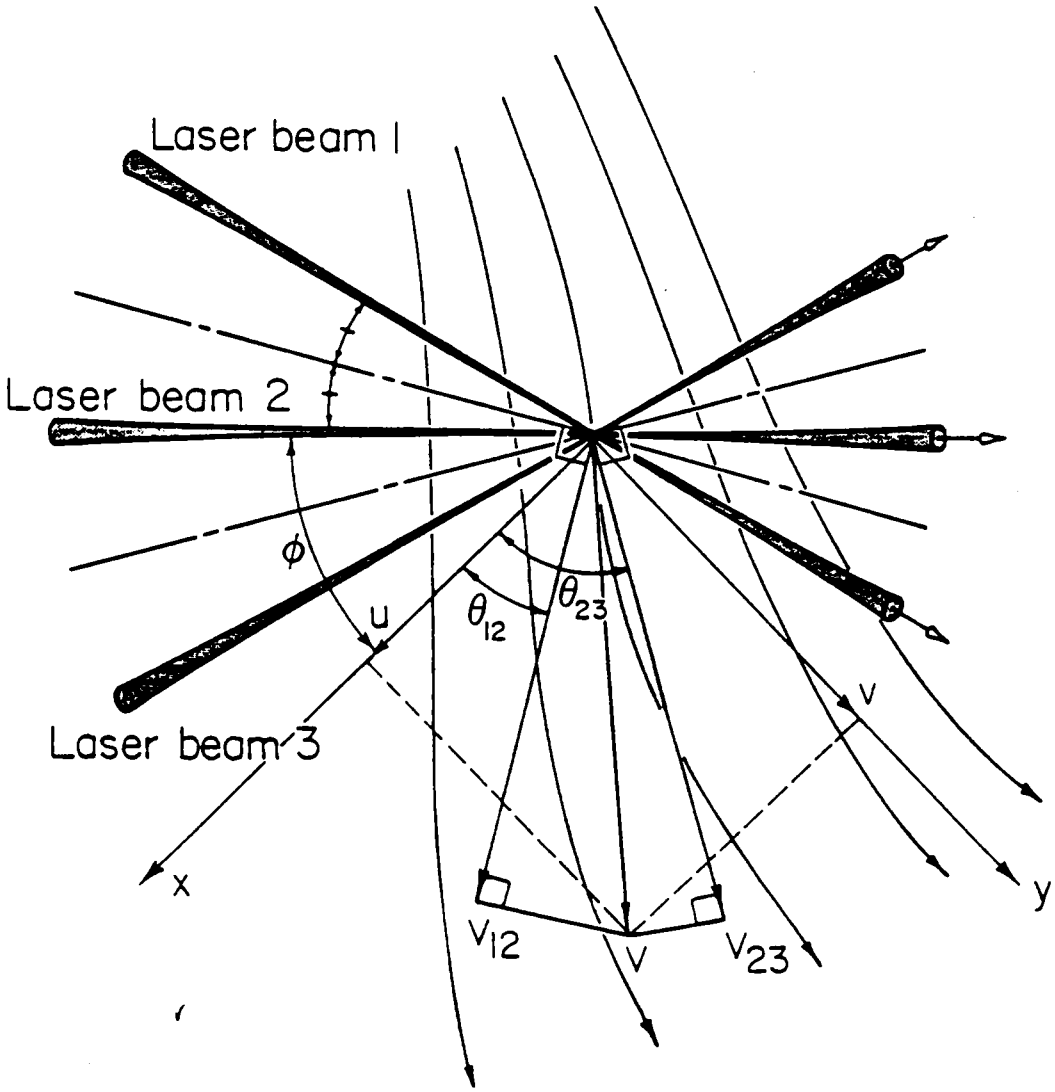

Fig. 4.1 Schematic representation of the crossing of 3 beams. All 3 beams are in the same plane. Interference between beam 1 and 2 generates the velocity component V_{12} and interference between 2 and 3 generates the component V_{23}.

sidewalls of the test section. This is important, because only then, the defraction angles of the side beams remain constant at all times. This limitation is also dictated by the need to insure that the three beams meet at the same point in the water, forming the measuring volume. The velocity components u and v for the general system of coordinates are given in terms of the measured quantities and the angles defined in Fig. 4.1 by virtue of the following straightforward relationships

$$V_{12} = u \cos \theta_{12} + v \sin \theta_{12} \qquad (4.2.1)$$

$$v_{23} = u \sin \theta_{23} + v \cos \theta_{23} \qquad (4.2.2)$$

Errors in the magnitude of the velocity component v_{12} and v_{23} may be anticipated on the order of 0.5% of the mean. However, the error anticipated in the circumferential direction is much larger than the actual measurement error. In Fig. 4.2, if ΔV_{12} and ΔV_{23} is the actual measuring error of the two components v_{12} and v_{23} then ABCDA represents the error in the measurement of the resultant velocity. If the angle ϕ is small then BD is small, namely approximately equal to the magnitude of the actual measurement error. However, in the present work AC was approximately equal to 9% of the mean axial velocity. Considering the fact that the velocity component in this direction may be rather low, this error is sometimes considerable.

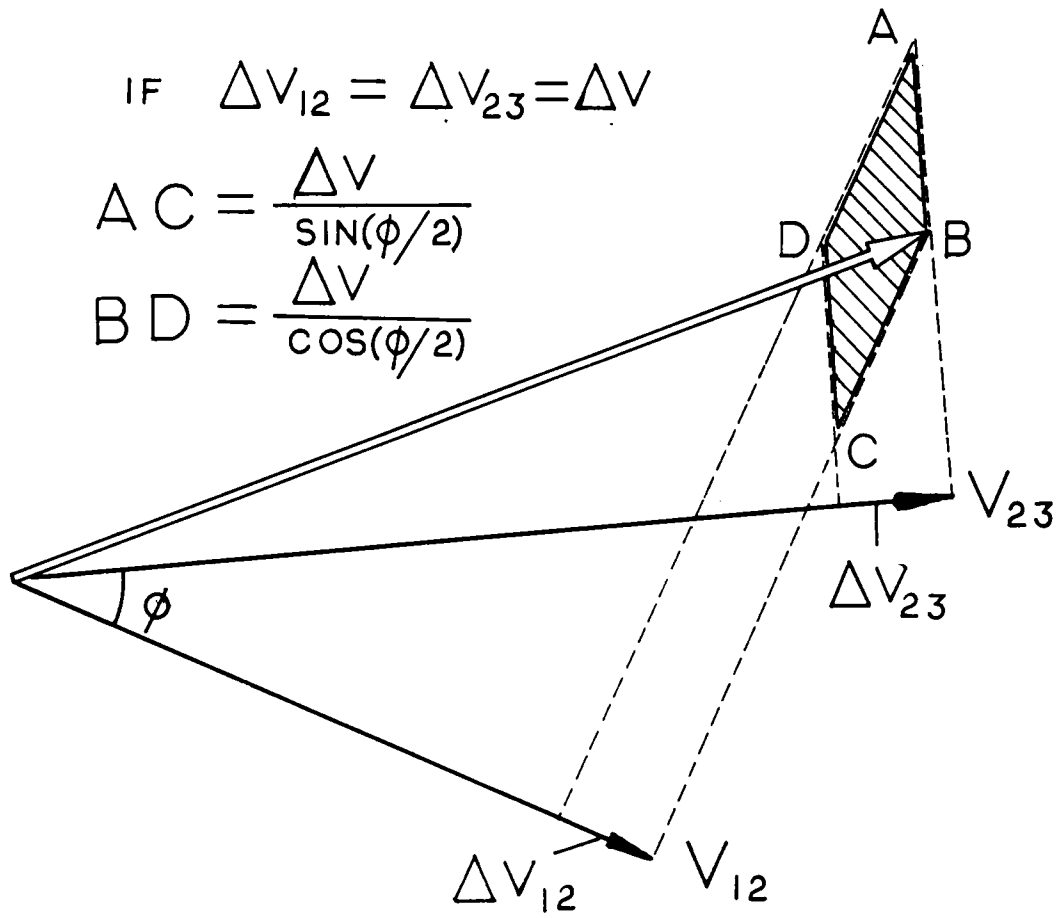

Fig. 4.2 Schematic representation of errors inolved in 3-beam LDV system, or 2 velocity component measurements.

4.3 The Traversing Mechanism

A special optical bench was constructed. The bench was mounted on traversing towers which permit rotation about the optical axis of the Laser-Doppler Velocimeter as well as translation in the horizontal, vertical as well as in the direction parallel to the axis of the LDV (Fig. 4.3). The key feature of the system is that traversing is permitted perpendicular to the local tangent plane of the body. This is the natural boundary-layer coordinate. Moreover, the two components parallel to the wall surface can be measured all the way down to the wall. This is possible because all three beams are in one plane.

Using the traversing towers the plane of the beams can be placed at any position inside the tunnel. Care was taken for the central beam to remain always normal to the side wall of the test section. A stepping motor connected to one of the traversing towers allowed accurate traversing across the boundary layer, by displacing the optical bench in the direction normal to the plane of the beams.

It is obvious that since the plane of the beams is always normal to the side walls of the test section, boundary-layer measurements can be performed for a given position of the model, only for the most upper or the most lower points of its surface. For the measuring volume to reach any point of the surface, it is necessary to rotate the model.

A special support for the model has been constructed (Fig. 4.4). The model was mounted by its end at the strut BD. This strut was attached to the axle CO by means of the bracket BC. By rotating the strut and the bracket around points B and C the model can be placed at any angle of attack in the flow. The axle CO can rotate about its axis

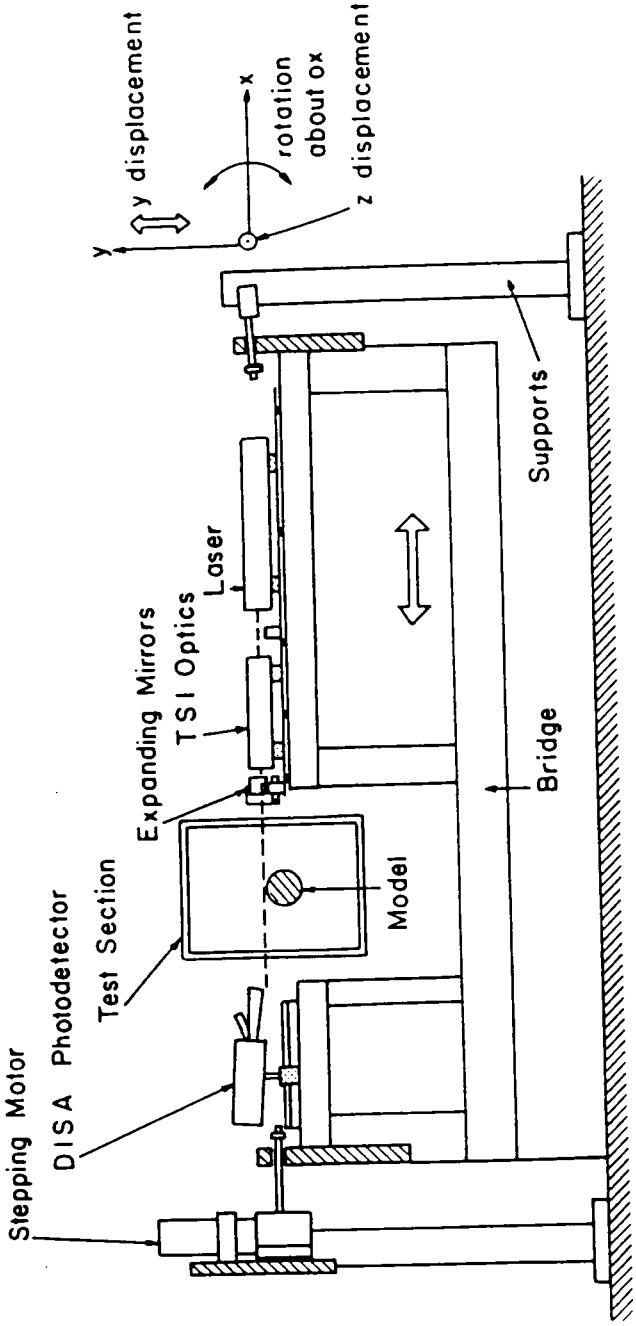

Fig. 4.3 Schematic of the optical bench, optical equipment and traversing options.

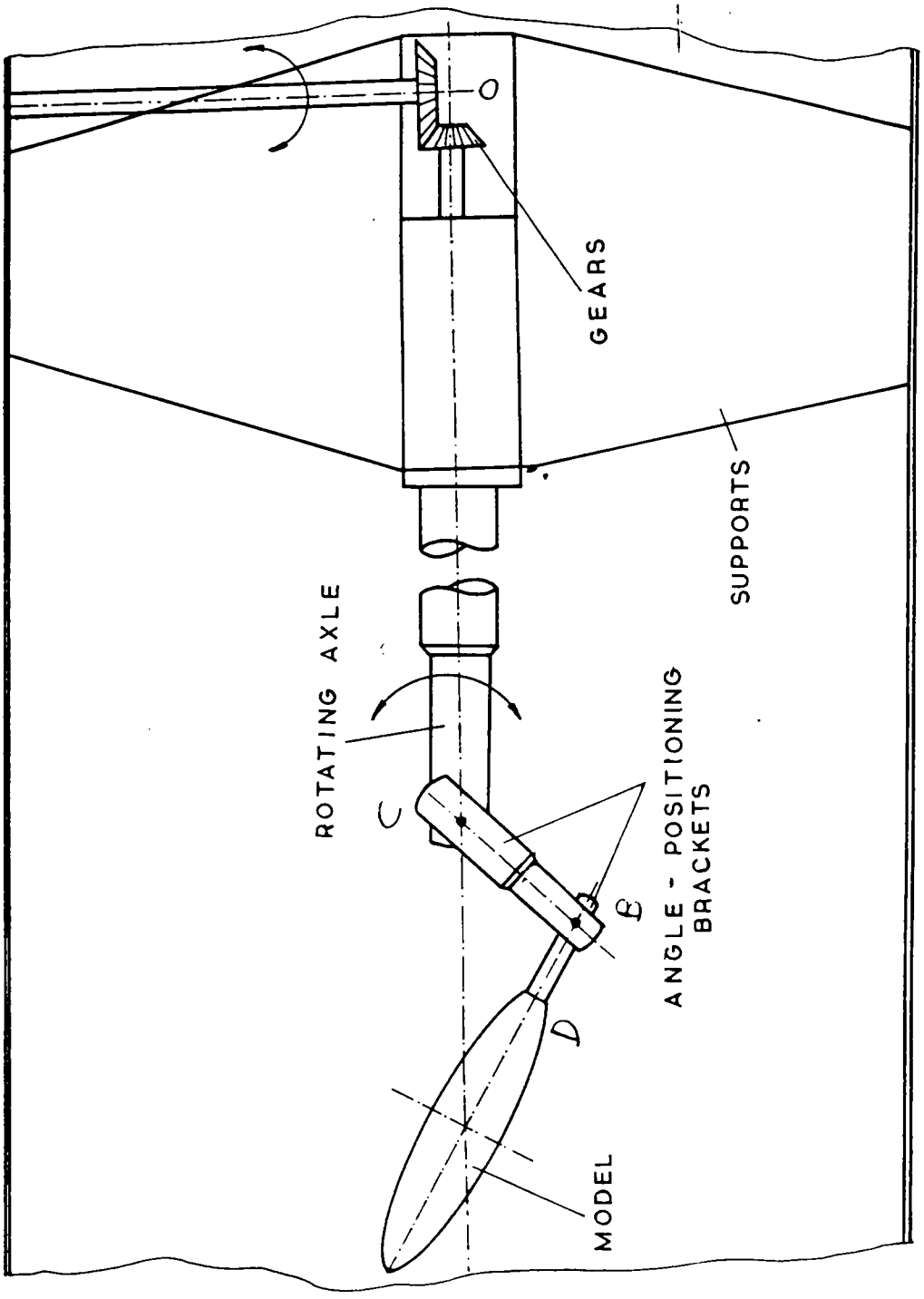

Fig. 4.4 Model support.

via the gears at O from a position outside of the tunnel. Since the axis of rotation is parallel to the direction of the flow, the model can be rotated, maintaining always the same angle of attack. In this way, any point on its surface can be accessed by the plane of the beams and boundary-layer measurements can be performed anywhere.

The crucial step in Laser-Doppler measurements is the determination of the location of the measuring volume. This was accomplished as follows. The location of the model in the test section was first determined optically by virtue of a telescope having a cross-hair positioner. The space coordinates of the front and tail nose of the spheroid were recorded with respect to reference points on the side and upper walls of the test section. The optical bench was then displaced and rotated until the plane of the beams became tangent to the model and the point of the beam intersection was brought as close as possible to the model surface. The location of the intersections of the three beams with the two side walls of the tunnel were then determined and stored. The location of the nose and tail of the model, with respect to the walls of the test section, the analytical expression of the model geometry and the points of intersection of the beams with the side walls were used as input to a computer program. The program then estimated the location of the measuring volume of the model as well as the direction of the measuring velocity components with respect to the general system of coordinates. The model and the beams were reconstructed and plotted to provide an extra check of errors in the position of the model and the measuring volume. An example of this

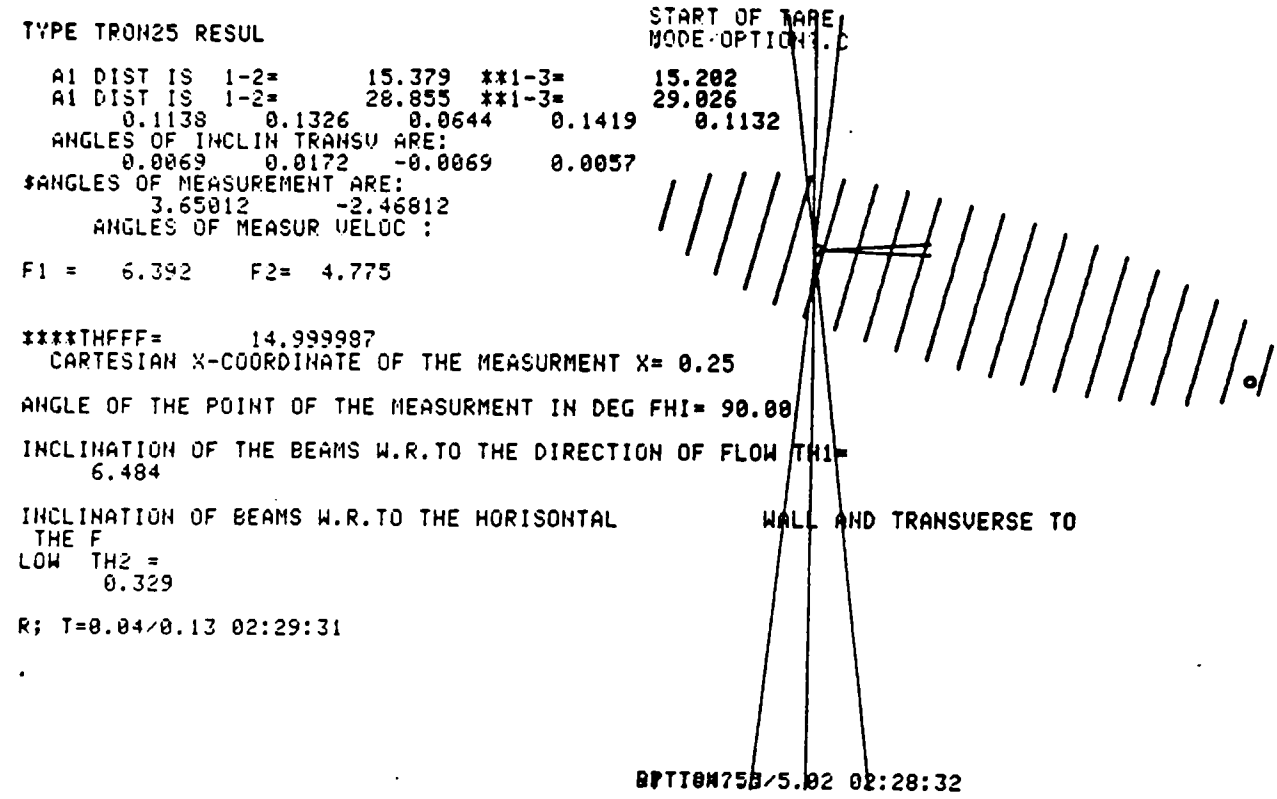

Fig. 4.5 Example of laser beam locations with respect to the body and output of program for the calculation of measuring position.

geometry is shown in Fig. 4.5. Any angle or position required for data reduction is provided as output from this program

The method allows the operator to position the system as close as possible to the surface. The final position of the measuring volume on the model is then recorded. Traversing across the boundary layer is performed perpendicular to the model surface, in steps controlled by the stepping motor. It was estimated that the error of positioning the measuring volume on the body in circumferential or axial location is less than 1% of the length of the model. Errors in vertical displacements should be less than 1% of the average thickness of the boundary layer.

In all other methods used to measure 3-D boundary layers, the traversing mechanism was part of the model. Therefore, expensive and sophisticated models had to be constructed. In the present method, the measuring device can approach the model at any point from any direction without interfering with the model. Our model is simple and can be easily mounted on the strut. Velocity measurements can be performed for a wide variety of geometries, using low cost models.

4.4 Optical and Electronic Equipment

A 5 mW laser source was used. The train of the sending optics consisted of various elements. Immediately after the laser source, a variable beam splitter split the main beam into two beams (Fig. 4.6), one of which continued on the direction of the main beam and the other displaced vertically. The power of the two beams was adjusted at 66% and 33% of the power of the main beam reespectively. A 50-50

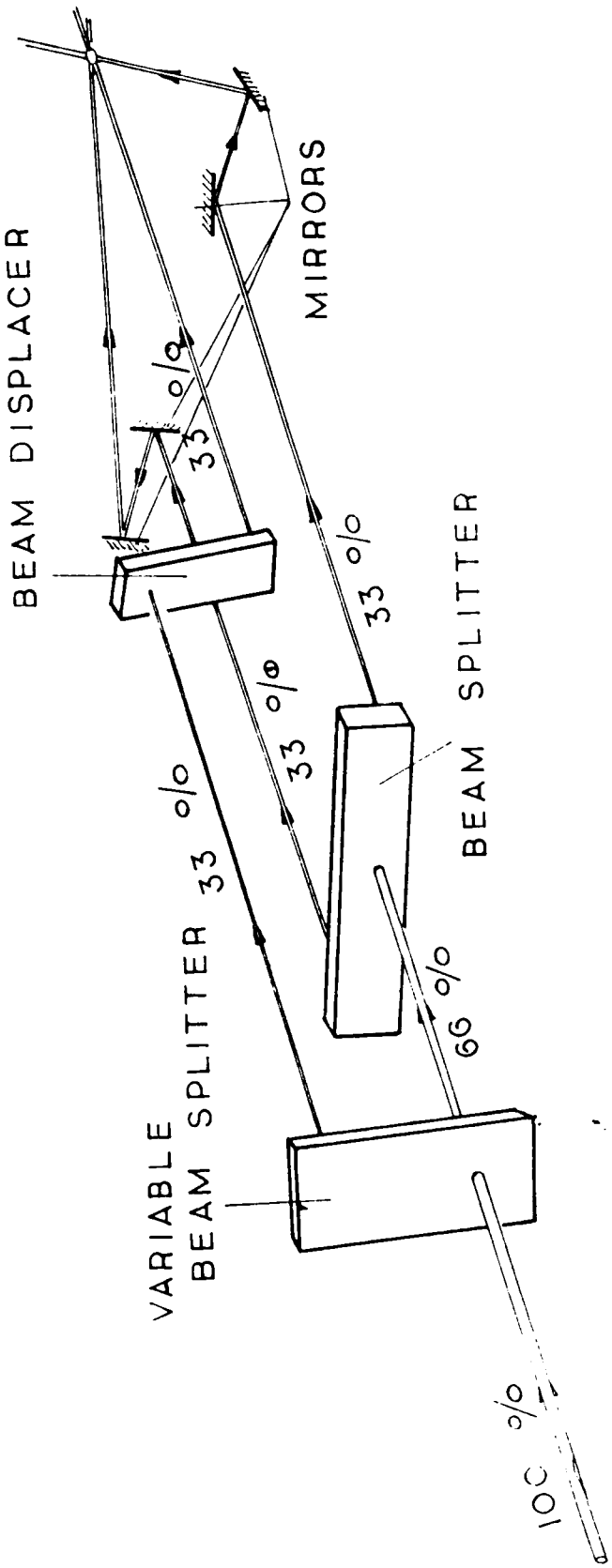

Fig. 4.6 Arrangement of sending optics.

beam splitter was used to divide the central beam into two beams of equal power and displace them sidewise. In this way, after the second beam splitter three beams of equal power were created, two of them at the same level of the main but displaced sidewise and one vertically displaced.

At the end of the train of sending optics, a lens was placed to generate beam wastes at the measuring volume. A system of mirrors was placed after the sending optics. They were used to further displace the side beams and therefore increase the angle of the beams and consequently decrease the error in the cross-flow velocity measurement. The standard photodetector tubes were placed on the other part of the optical bench in a foward scattering mode. A schematic of the sending and receiving optics is shown in Fig. 4.7.

The electronic equipment consisted of devices to excite the laser source, move the stepper motor, and analyze the signal of the photodetectors. A MINC computer was used to control the entire experiment.

No simultaneous measurements were performed. Instead, two blinders activated by solenoids were employed to block the side beams sequentially. The two photodetectors were focused on the measuring volume. The heart of the data acquisition system was a very inexpensive mechanical time switch. The use of the switch was dictated by the large power requirements of solenoids that control the blinders of the laser beams. Measurements were obtained sequentially as follows:

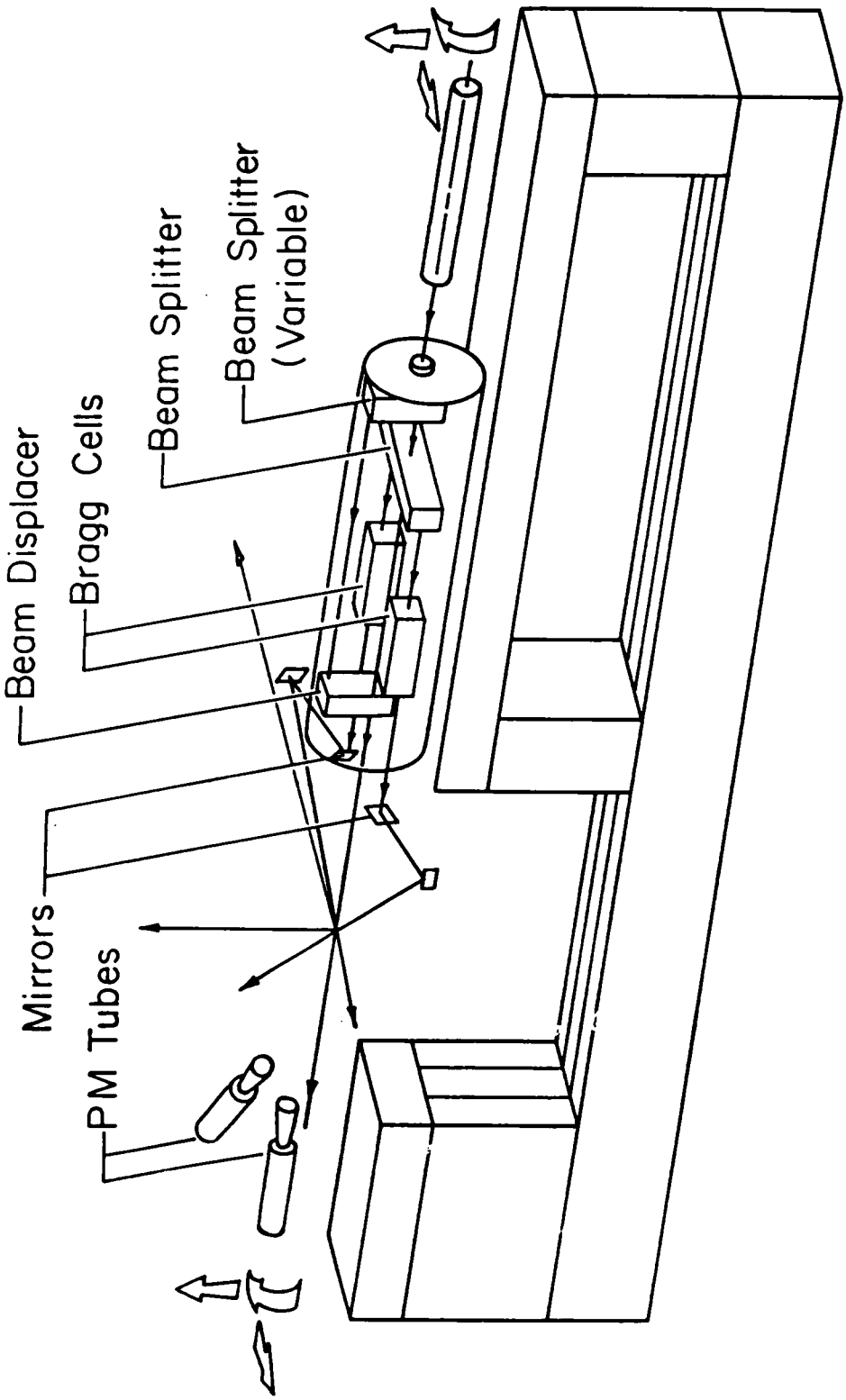

Fig. 4.7 The optical bench for the measurement of 2 components.

A blinder blocked beam 1 and therefore the component V_{23} (Fig. 4.1) could be measured. The photodetector placed between beams 2 and 3 was connected through the time switch to the counter signal processor and the frequency of its signal was obtained by the counter. The time switch then sent a message to the computer to obtain a measurement. Beam 3 was then blocked, the second photodetector was connected to the counter, and the computer was signaled to measure and store the value of the component V_{12}. The measurements of the velocity components were checked by the computer and in case of inconsistent measurement, the process was repeated at the same point in the boundary layer. Finally, a signal from the time switch to the computer in turn sent pulses to the stepper motor. The traversing mechanism thus displaced the measuring volume to a new point in the boundary layer and the process was repeated. The number of pulses was defined in the program to allow fine steps near the wall. With speeds as low as 3 to 10 cm/sec, it was possible to generate boundary layers with thicknesses of a few millimeters on a model 20 cm long. In such boundary layers 40 to 50 data points were obtained usually, but 60 to 70 points can be easily obtained by cutting the traversing step. Two counter signal processors were used, and the two velocity component signals were fed simultaneously into the computer. After the necessary reliability tests of the measurement, the actual velocity components were calculated and stored.

4.5 Data Reduction

The location of each point in the boundary layer was measured starting from the first point near the wall where measurement was possible. The two components V_{12} and V_{23} along with their location were stored. Figure 4.8 shows a plot of the raw data of the components V_{12} and V_{23} of the velocity. The data stored in magnetic discs were transferred to the IBM 3081 mainframe computer for further reduction. The scatter in the experimental data may influence heavily the accuracy of the crossflow reduced component of the velocity. A standard cubic-spline smoothing routine was employed to generate velocity profiles from the discrete experimental data. To this end, nowhere the smoothing routine was allowed to alter the value of the velocities by more than 5% with respect to the mean stream. Fig. 4.8 shows discrete raw data, and the corresponding smoothed curves.

The smoothed profiles were then extrapolated to locate the position of the wall. This was determined as the point where the two velocity profiles coincide. Otherwise, the mean value of the two extrapolations was used as the position of the wall. In this way, two smoothed profiles were generated from the discrete experimental data corresponding to the components V_{12} and V_{23}. At this point, the geometry of the system regarding the location of the beams and the body as determined by the technique described in section 5.2 were inserted in the program. Having the angles θ_{12} and θ_{23}, the calculation of the components of the velocities u and v with respect to the system of coordinates x and ϕ were calculated by virtue of Eqs. (4.1.1) and (4.1.2).

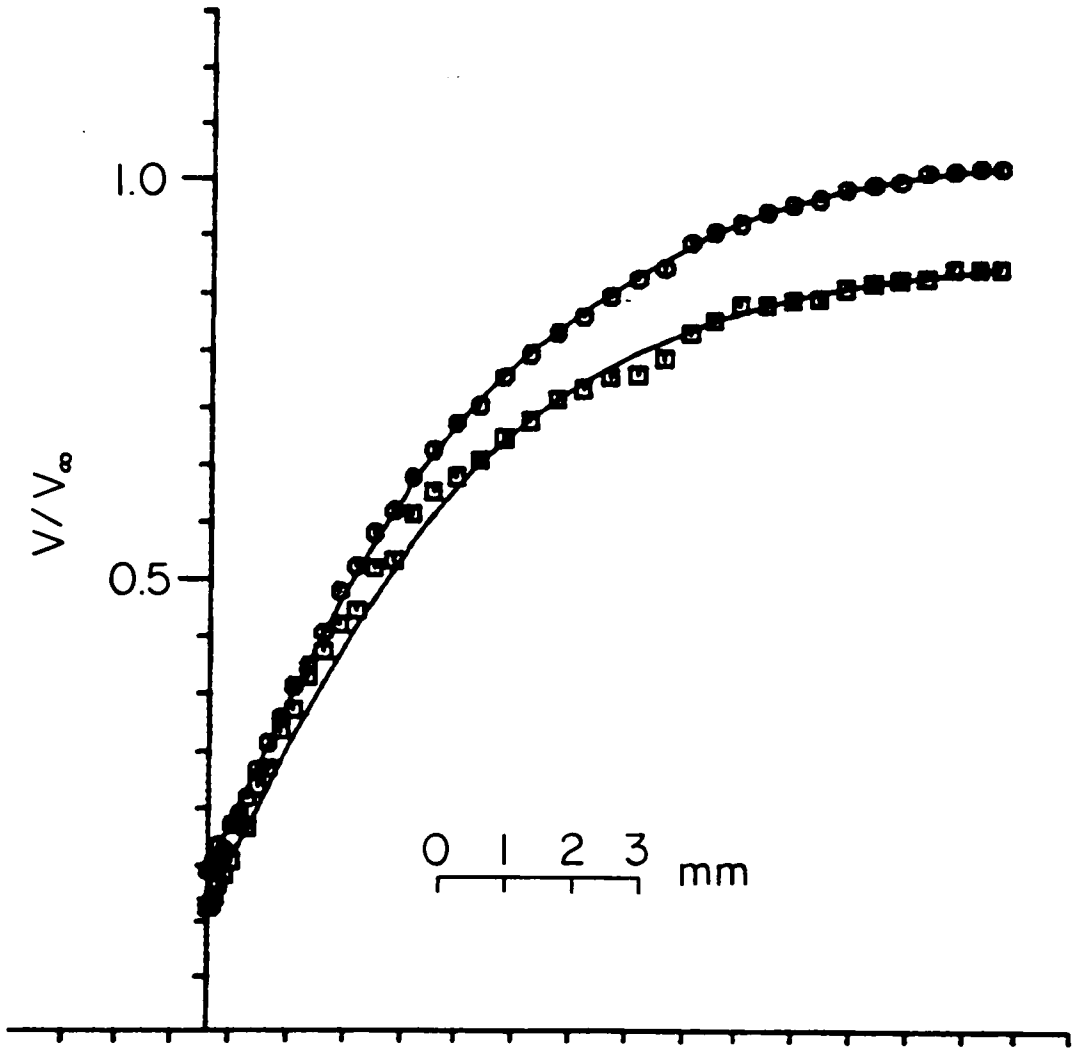

Fig. 4.8 The actual experimental points shown together with the smoothed profile on the leeward side at the fourth station, V_{12}; V_{23}.

It was difficult to obtain data in the immediate vicinity of the wall. This was attributed to the fact that the size of the measuring volume was not very small compared to the thickness of the boundary layer. The situation was more critical for axial stations near the nose, where the thickness of the boundary layer is very small. In such regions up to 10% of the velocity profiles is void of experimental data. The other reason for the inability to obtain data near the wall was that since no Bragg cells were used, the counter signal processor could not handle low frequency signals which correspond to velocity values of a few mm/sec. Those problems can be overcome if Bragg cells and a smaller size pinhole in the photodetector are used.

Data were obtained in this way at five axial stations and five circumferential positions. To facilitate comparison with the numerical results of Patel & Baek (1983), the present experimental results are presented in an outlay similar to the one included in this reference. The present experimental results and the numerical results of Patel & Baek are shown in Figs. 4.9 and 4.10, respectively. It should be noticed that the position of the experimental profiles does not coincide with integral values of coordinates. This is due to difficulties encountered in positioning the measuring volume on the surface of the model. The origin of the velocity profile in this figure is positioned at the point in the x-ϕ plane with the coordinates of the $z=0$ position of the measuring volume.

Patel and Baek (1983) found very abrupt changes in the thickness of the boundary layer and the shape of the velocity profile in the neighborhood of the line of separation, namely, between the angles θ =

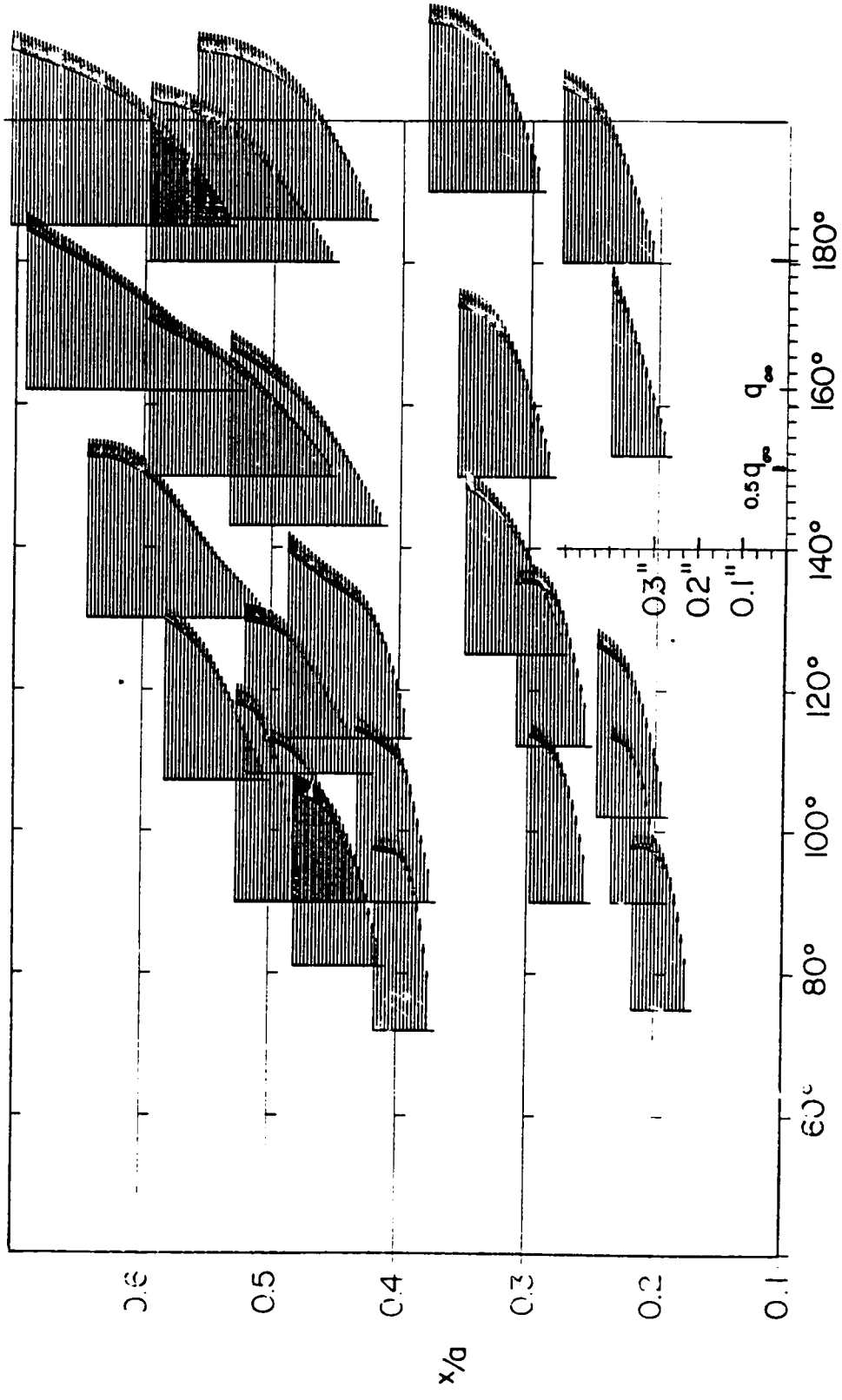

Fig. 4.9 The u-component velocity profile. Horizontal and vertical scales are marked in tenths of free stream velocity and increments of 1/10" (and 0.85 mm) respectively.

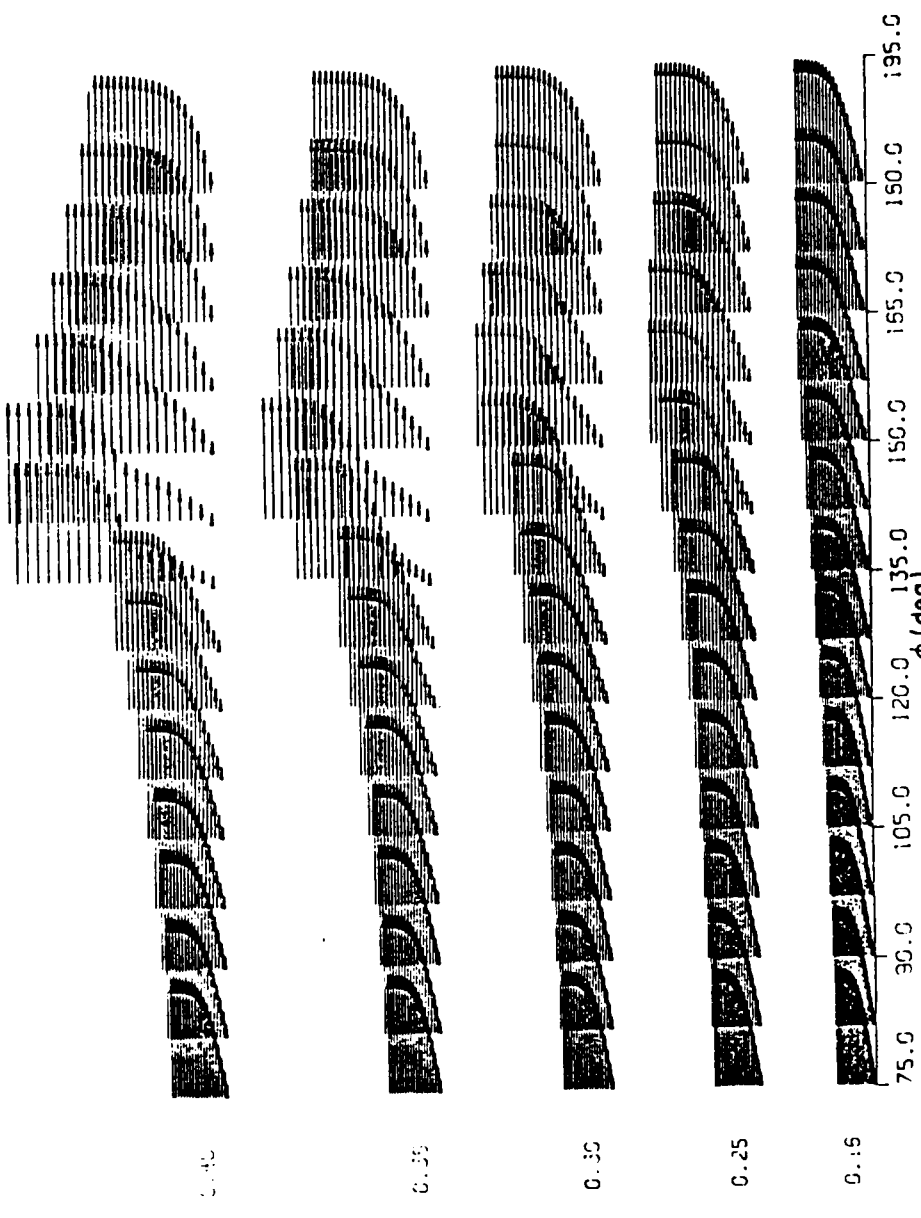

Fig. 4.10 The u-component velocity profile calculated by Patel and Baek.

135° and 140°. The velocity profile in the region beyond separation shows clear indications of an inflectional shape. This agrees at least qualitatively with our experimental data. Indeed, the first inflectional profile appears at $\phi \simeq 130°$ but not until $x/a = 0.4$. However, the abrupt change of the thickness of the boundary layer is not present. Apparently, the boundary layer equations are an insufficient model for describing exactly the physical situation in the neighborhood of separation much like the two-dimensional case.

The careful numerical calculations of Patel and Baek indicate in the forward half of the body thicker boundary layers closer to the windward side than the experiments. Indeed, the same trend is indicated by the calculations of Cebeci, Khattab and Stewartson (1981). However, this pattern is reversed for the aft portion of the body.

Both components of the velocity in the axial and circumferential direction are plotted in Figs. 4.11-15 for four axial stations along the model. The reader is cautioned to the fact that in these figures, five different scales of measurement are being employed. The position x,ϕ of the point on the ellipsoid where the data were obtained is the origin of the profile axis. The detailed markings on the orthogonal system shown in each figure provide the velocity scales and the scale in the vertical axis. The two velocity scales parallel to the x and ϕ directions, respectively, should not be confused with the corresponding length scales in these directions. Both velocity scales are marked in tenths of the freestream velocity, whereas the unit length in the z axis corresponds to 1/10 in. or 0.85 mm.

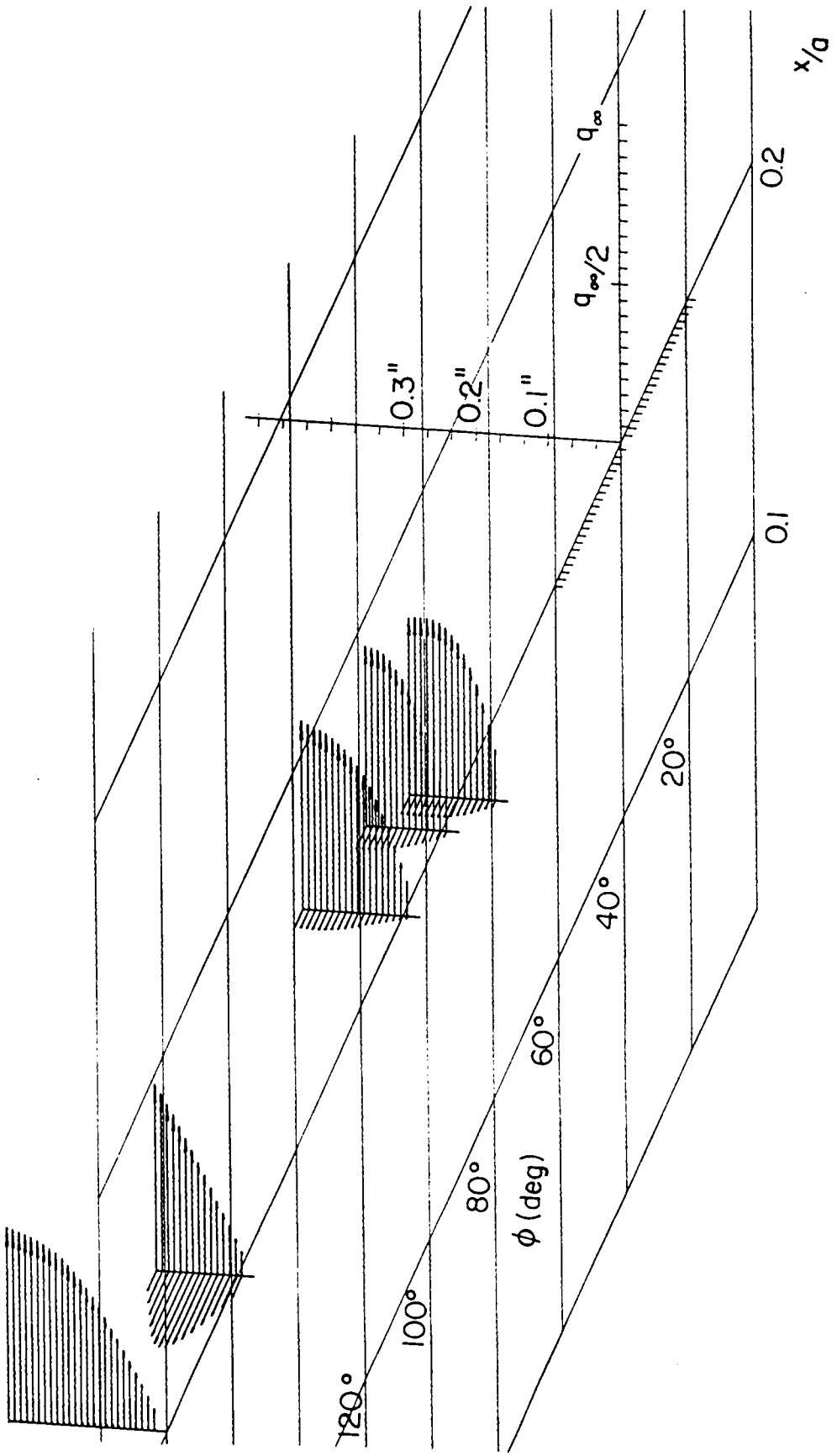

Fig. 4.11 The u- and v-velocity components at the first station of measurement.

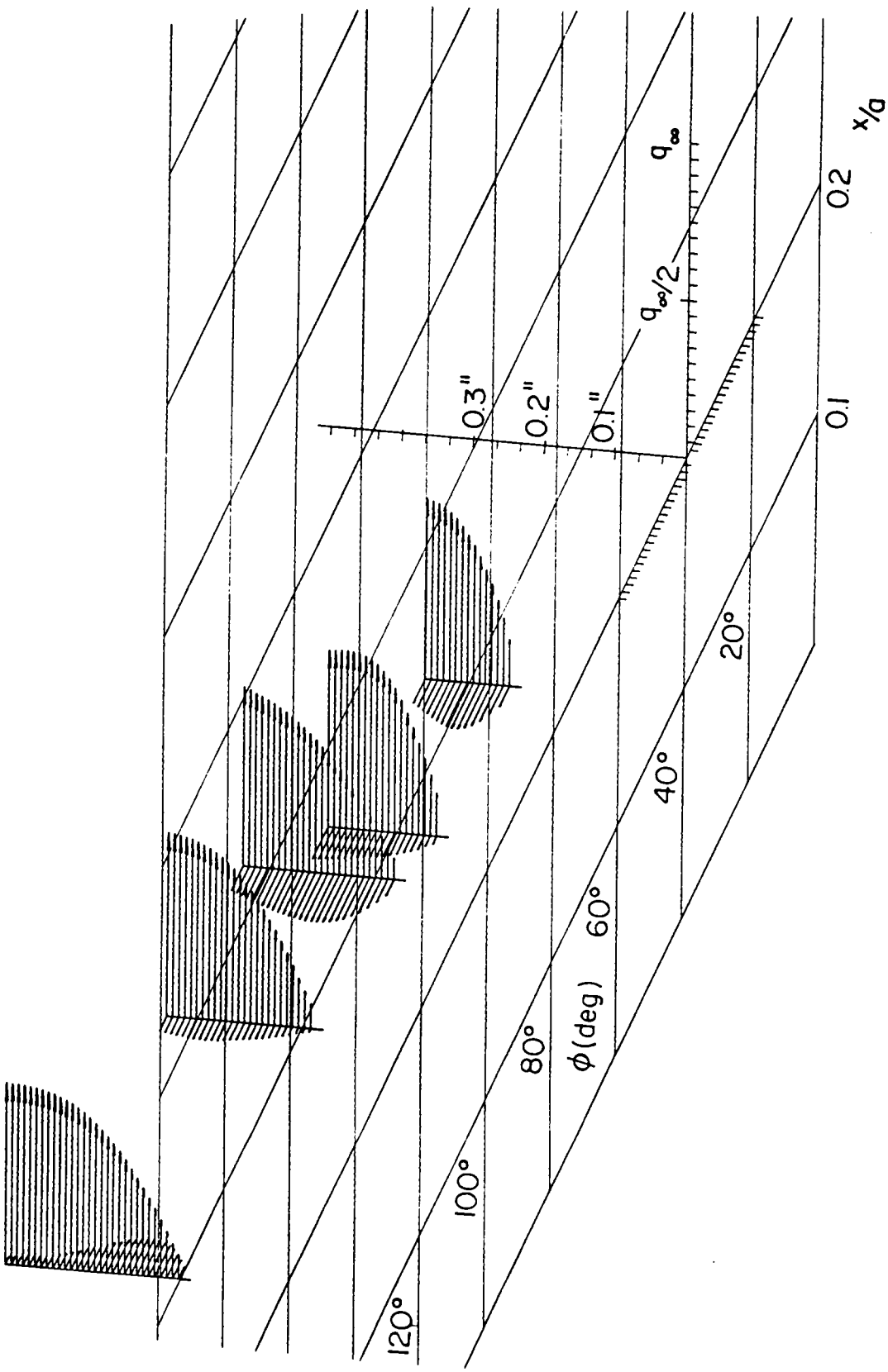

Fig. 4.12 The u- and v-velocity components at the second station of measurement.

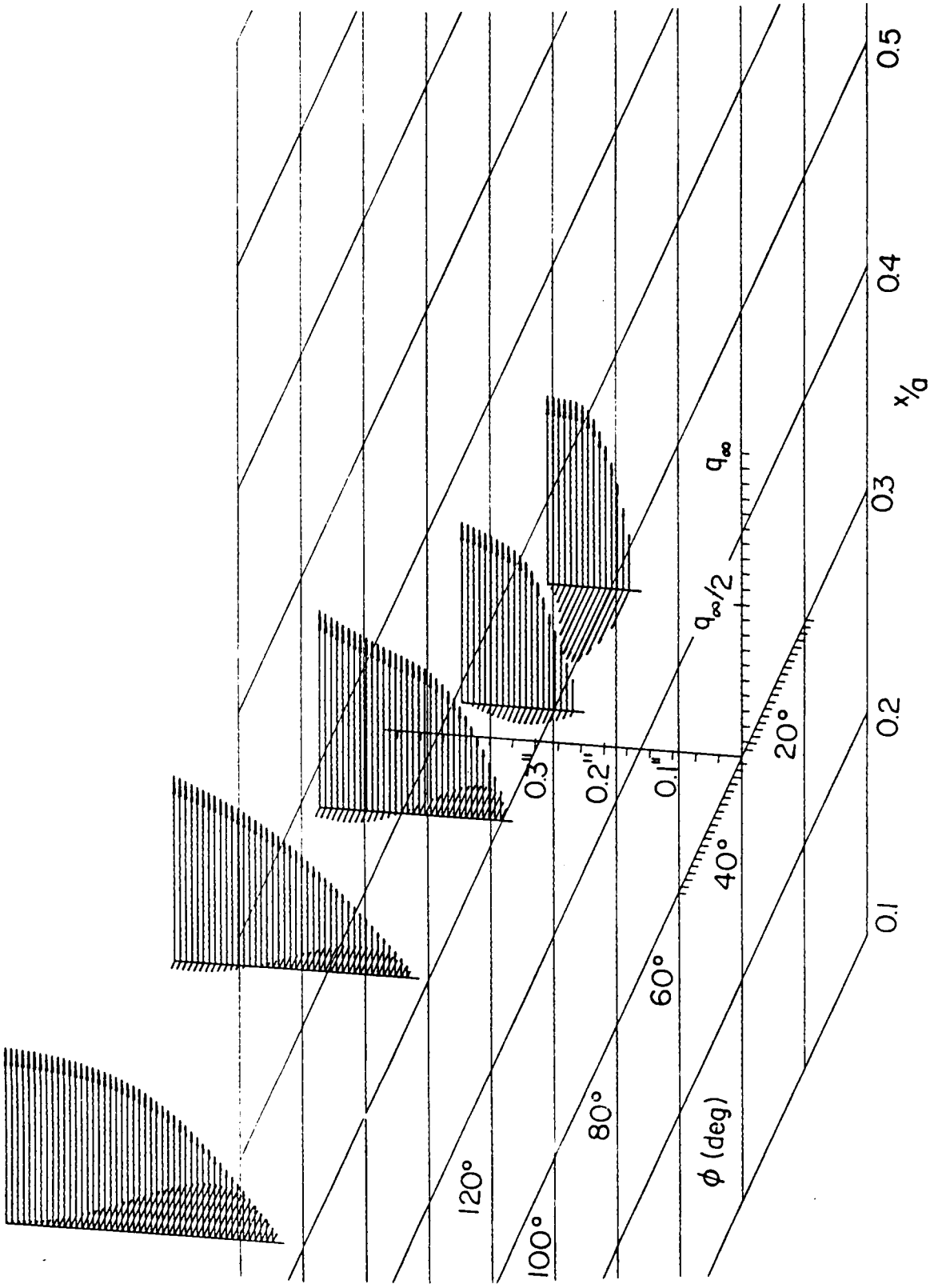

Fig. 4.13 The u- and v-velocity components at the third station of measurement.

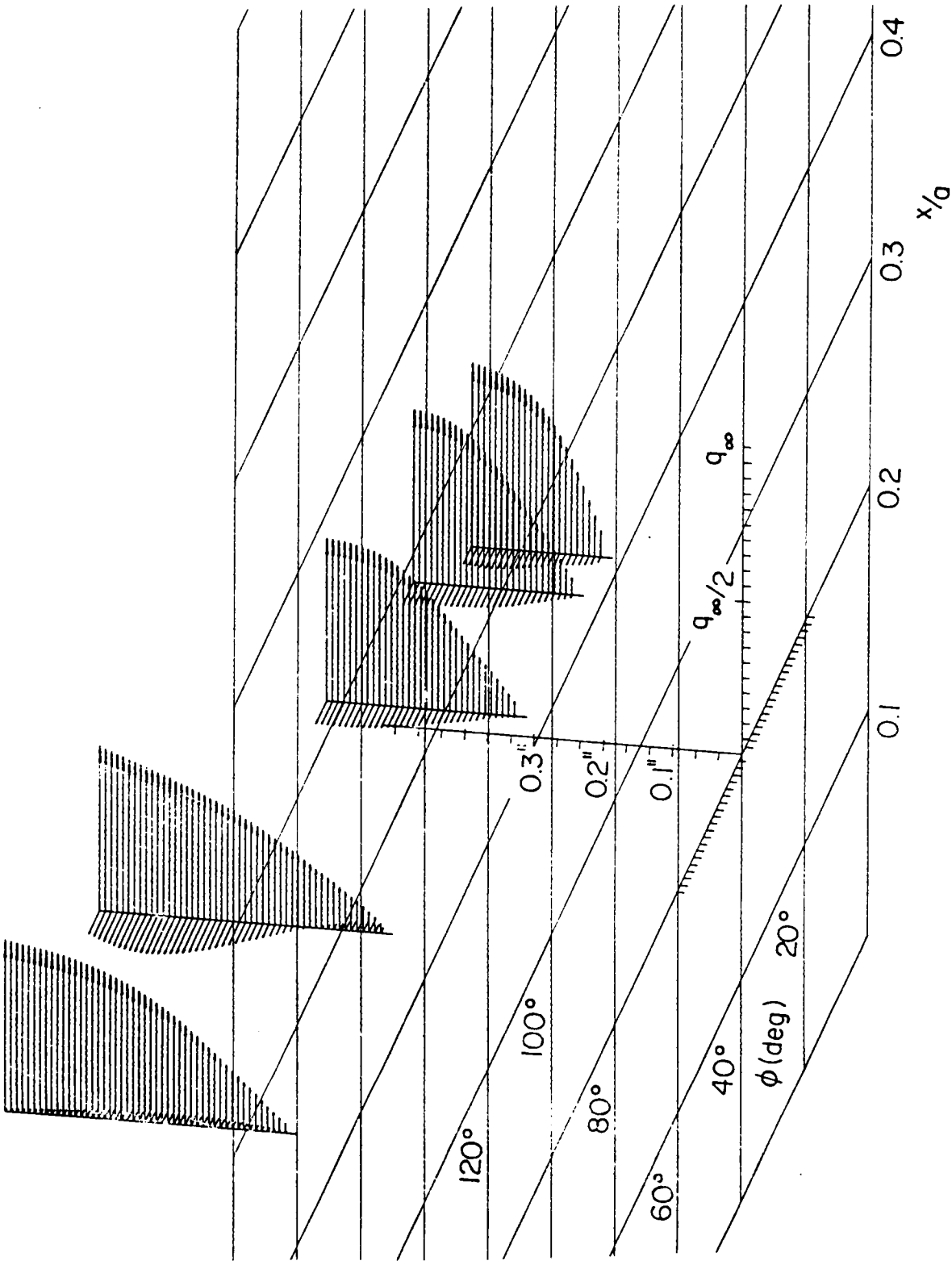

Fig. 4.14 The u- and v-velocity components at the fourth station of measurement.

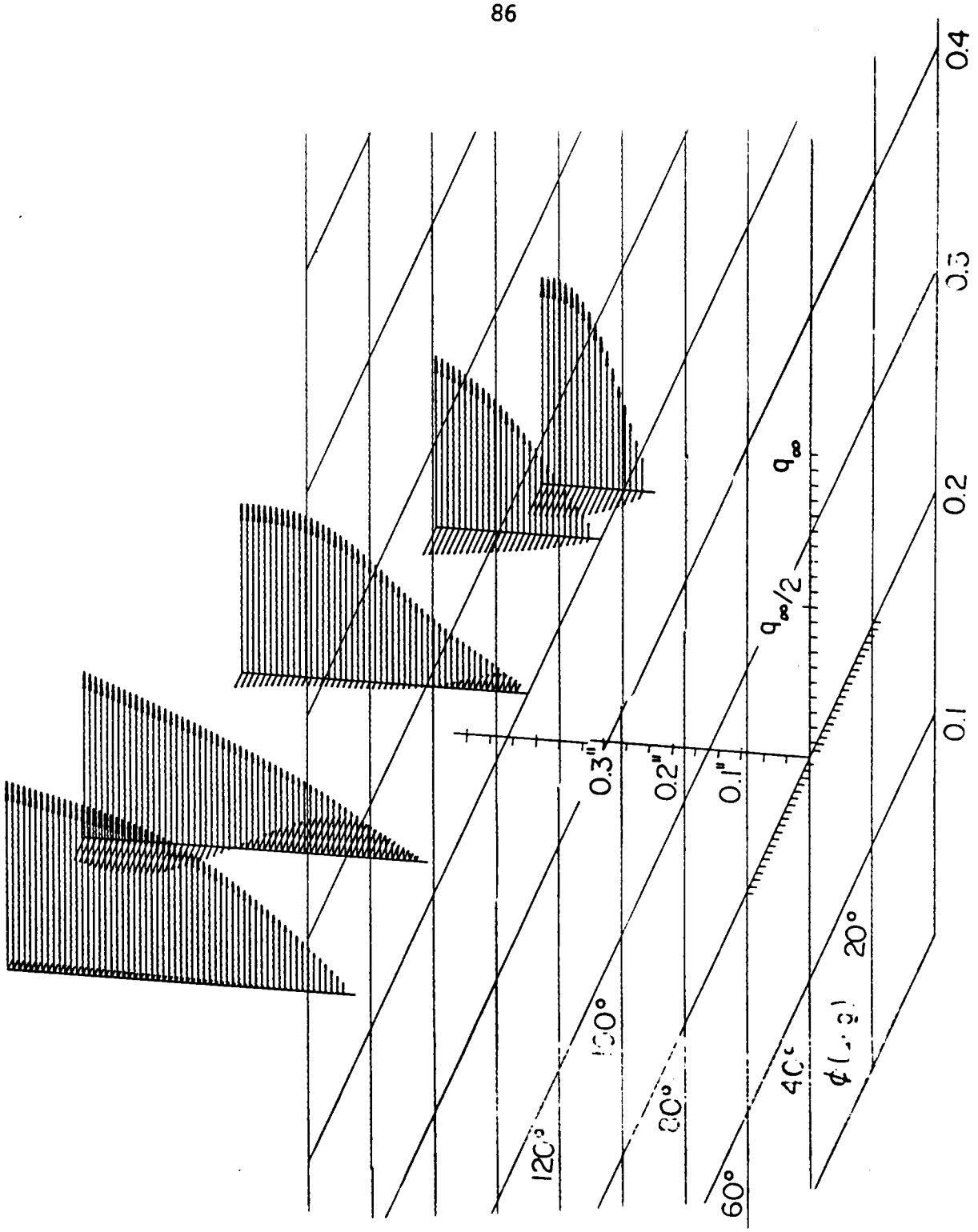

Fig. 4.15 The u- and v-velocity components at the fifth station of measurement.

Finally, a collection of all the experimental data obtained is presented in a three-dimensional outlay in Fig. 4.16. The figure is a composite of Figs. 4.12-15 and, therefore, the scales are identical to those employed previously.

The data presented in Figs. 4.11-16 were obtained at locations on the surface of the body which do not correspond to integral values of the coordinates x and ϕ. This is because of difficulties for positioning the LDV control volume at a specific location on the body. The data in these figures were smoothed only along the z-direction. To facilitate comparison with other methods and to obtain a clearer picture of the phenomena under investigation, we have used a cubic spline technique to smooth and interpolate the data over the x and ϕ domain as well. This method permits also the plotting at any location on the body. Integral values of x and ϕ stations were thus chosen.

The profiles generated in thie way were plotted first along fixed x station (Figs. 4.17 through 4.24) and then along fixed ϕ station (Figs. 4.25 through 4.31). Field view of interpolated profiles are presented in Figs. 4.32 and 4.33.

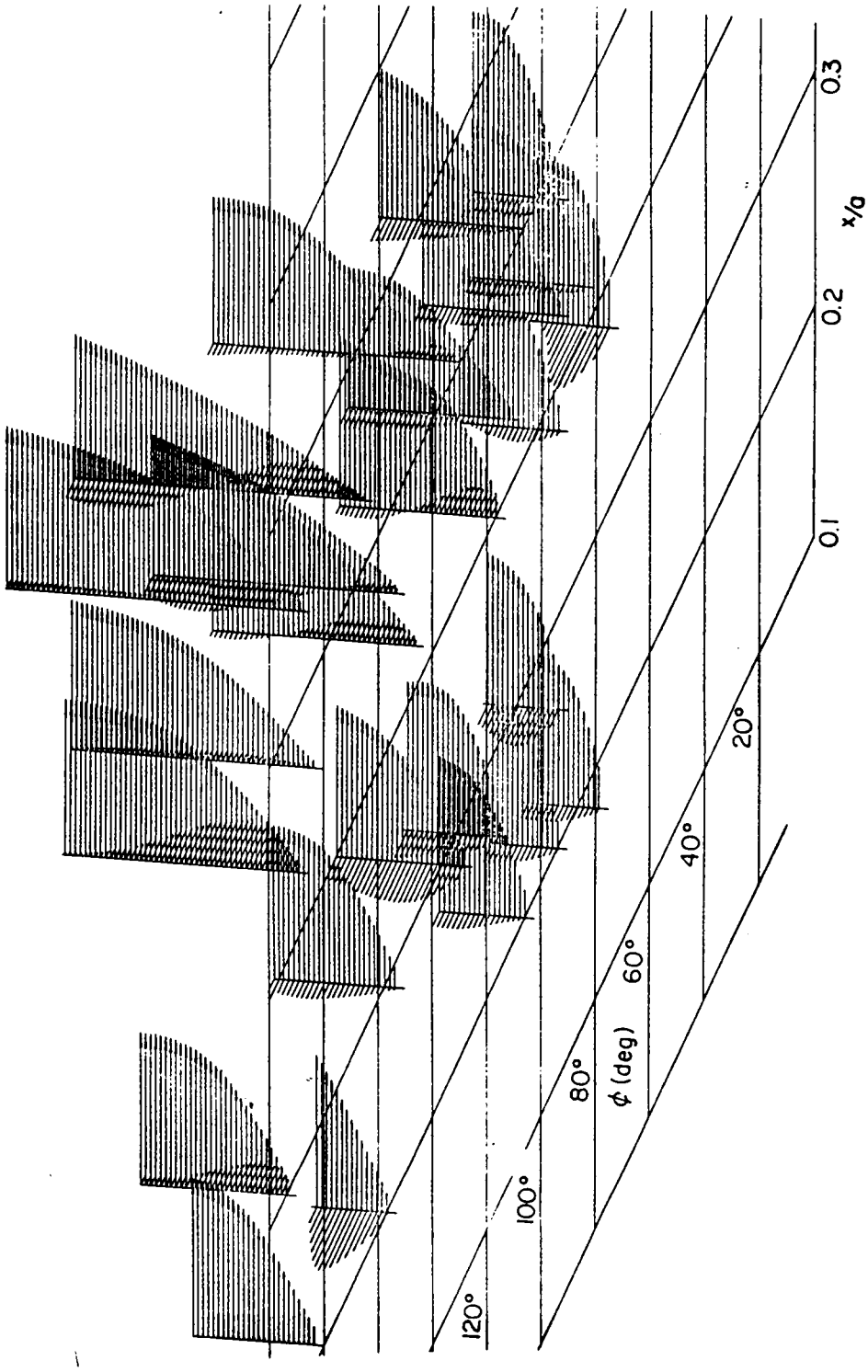

Fig. 4.16 Composite figure showing all the velocity profiles in the two-dimensional space of the ellipsoid surface.

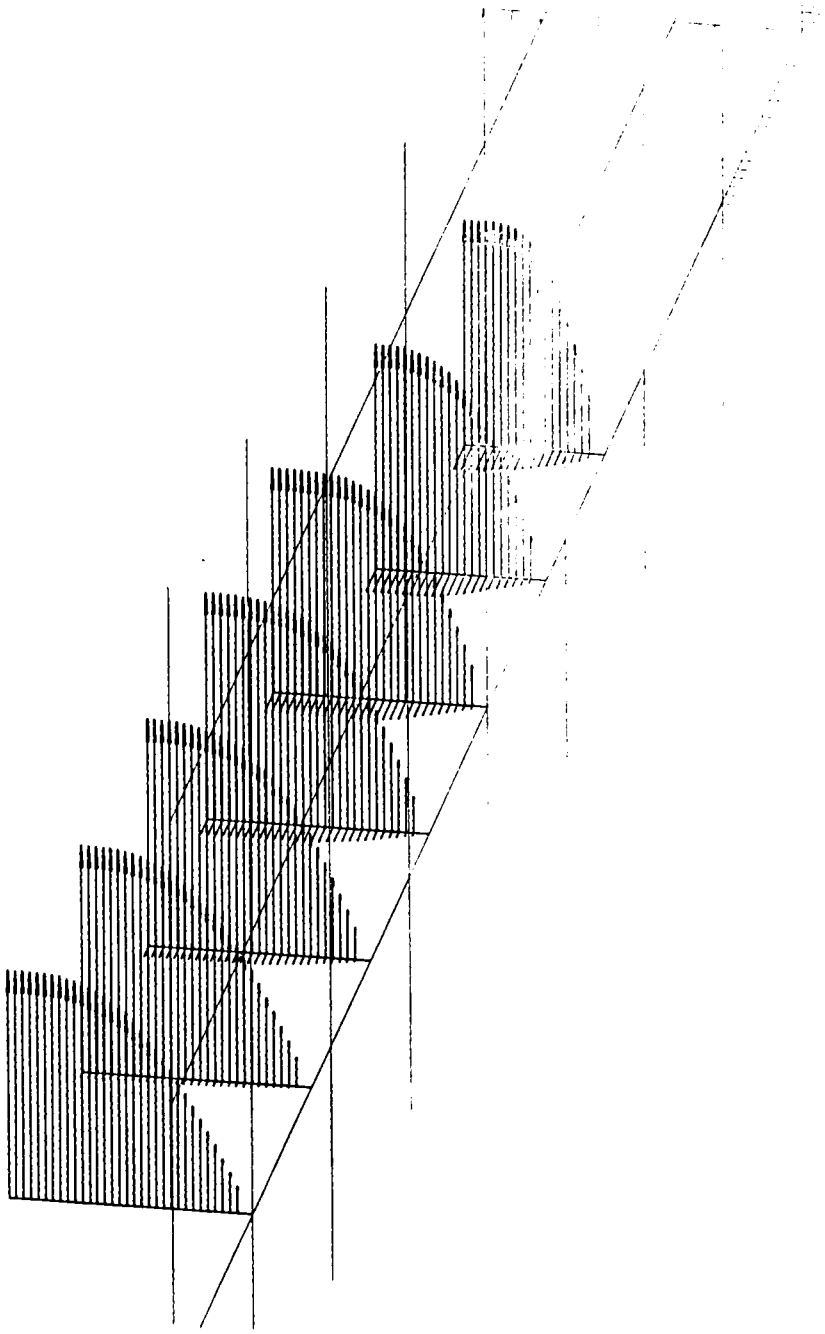

Fig. 4.17 Interpolated velocity profiles at x/a = 0.2

Fig. 4.17

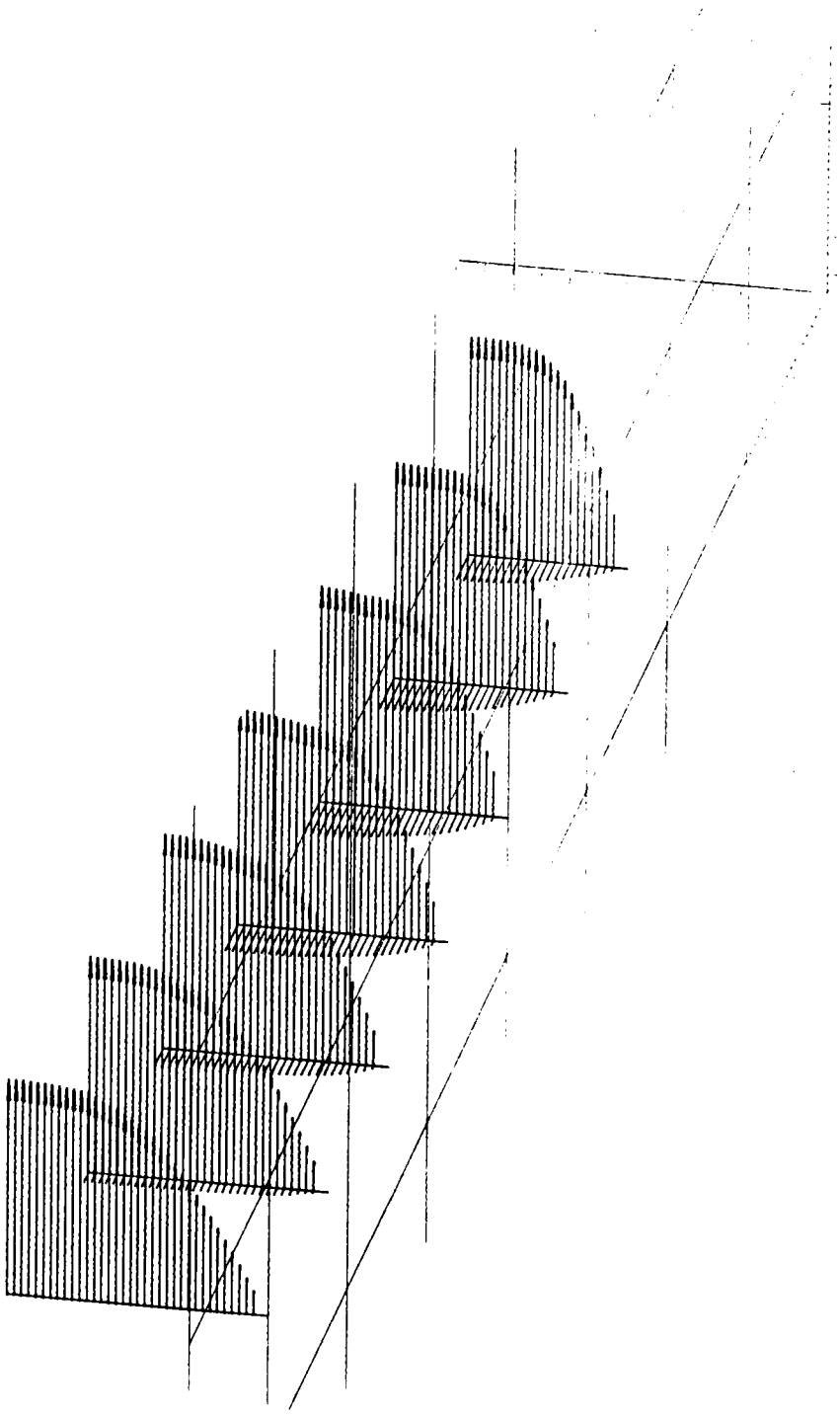

Fig. 4.18 Interpolated velocity profiles at x/a = 0.25

Fig. 4.18

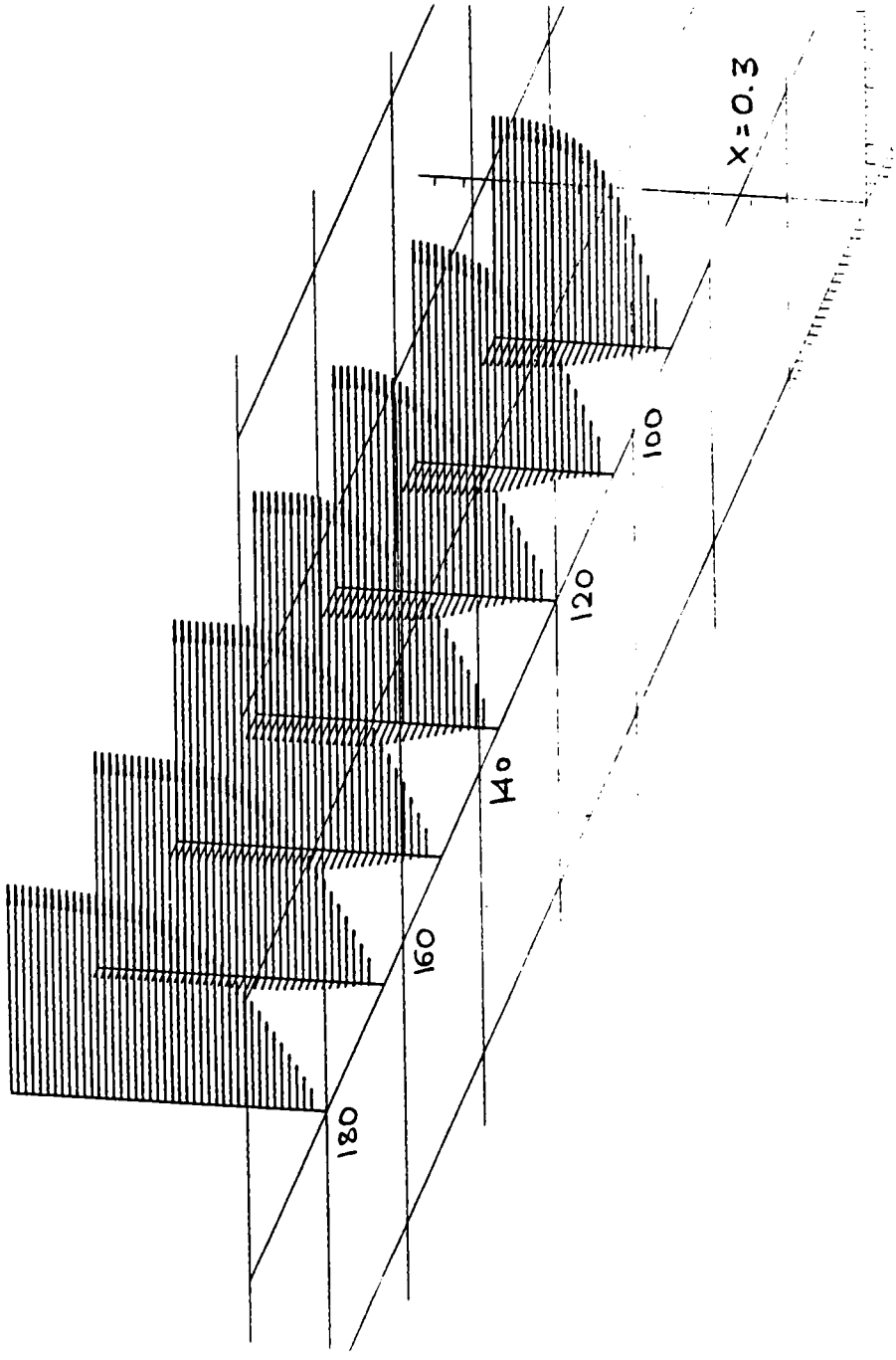

Fig. 4.19 Interpolated velocity profiles at x/a = 0.3

Fig. 4.19

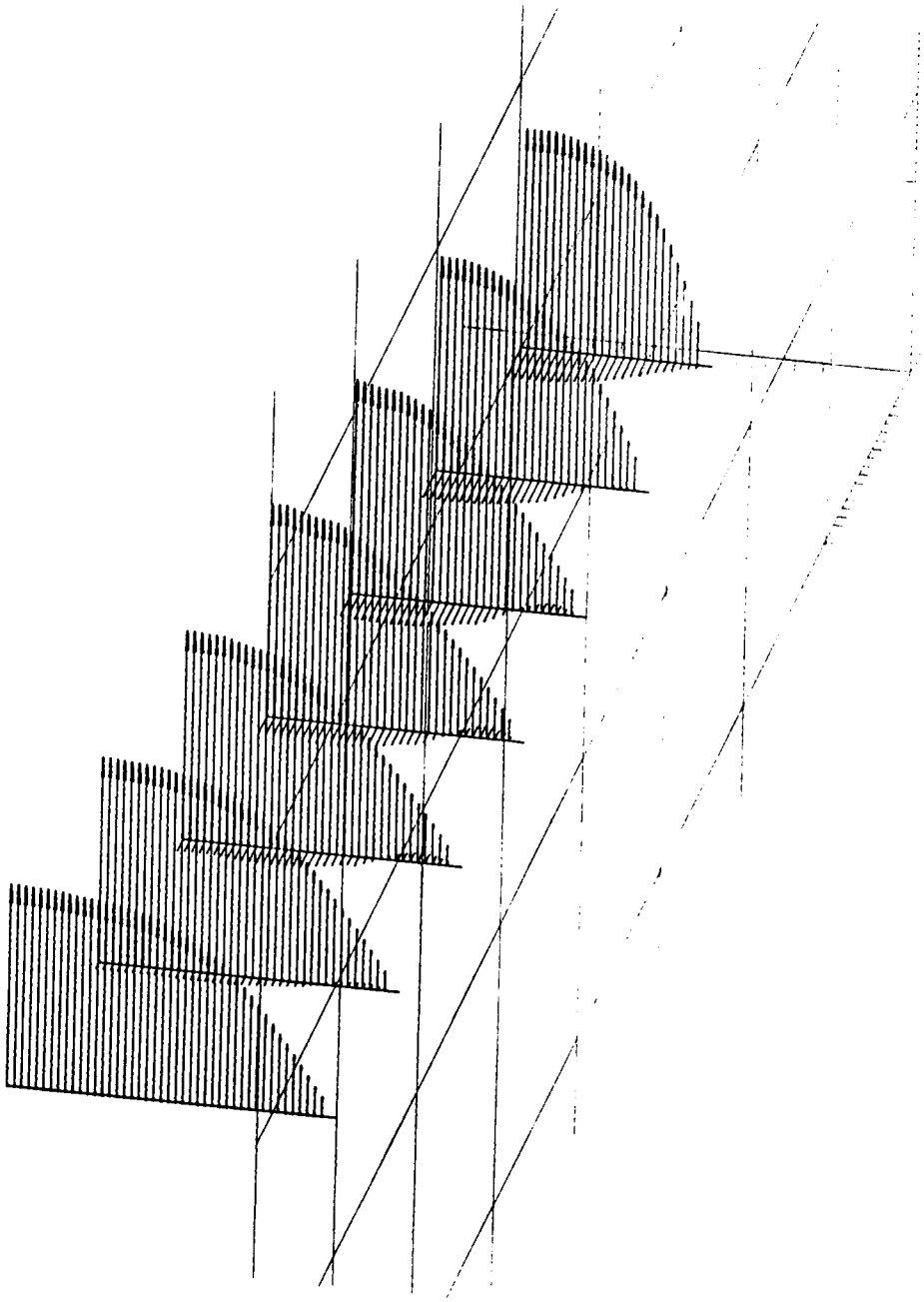

Fig. 4.20 Interpolated velocity profile at x/a = 0.35

Fig. 4.20

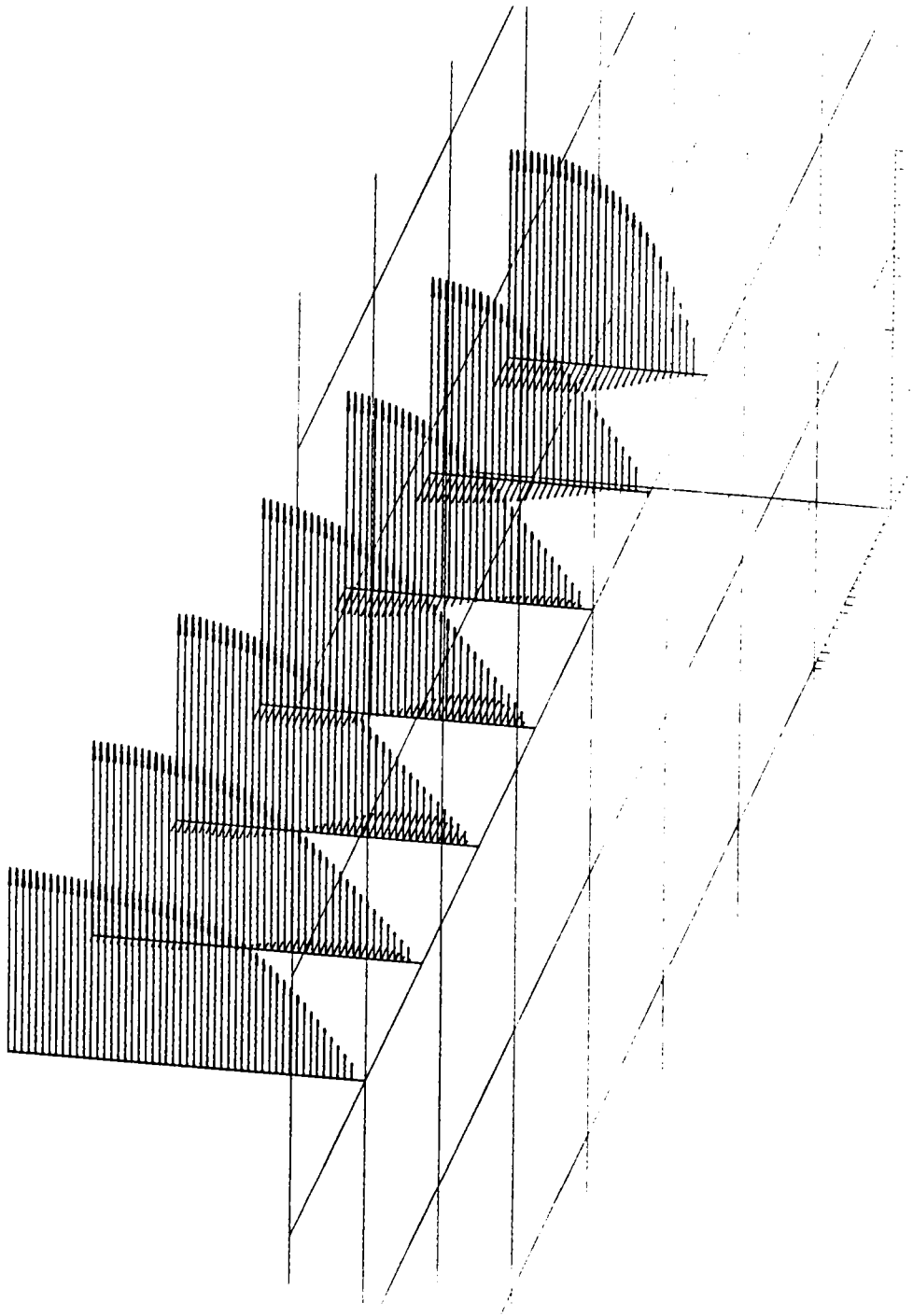

Fig. 4.21 Interpolated velocity profile at x/a = 0.4

Fig. 4.21

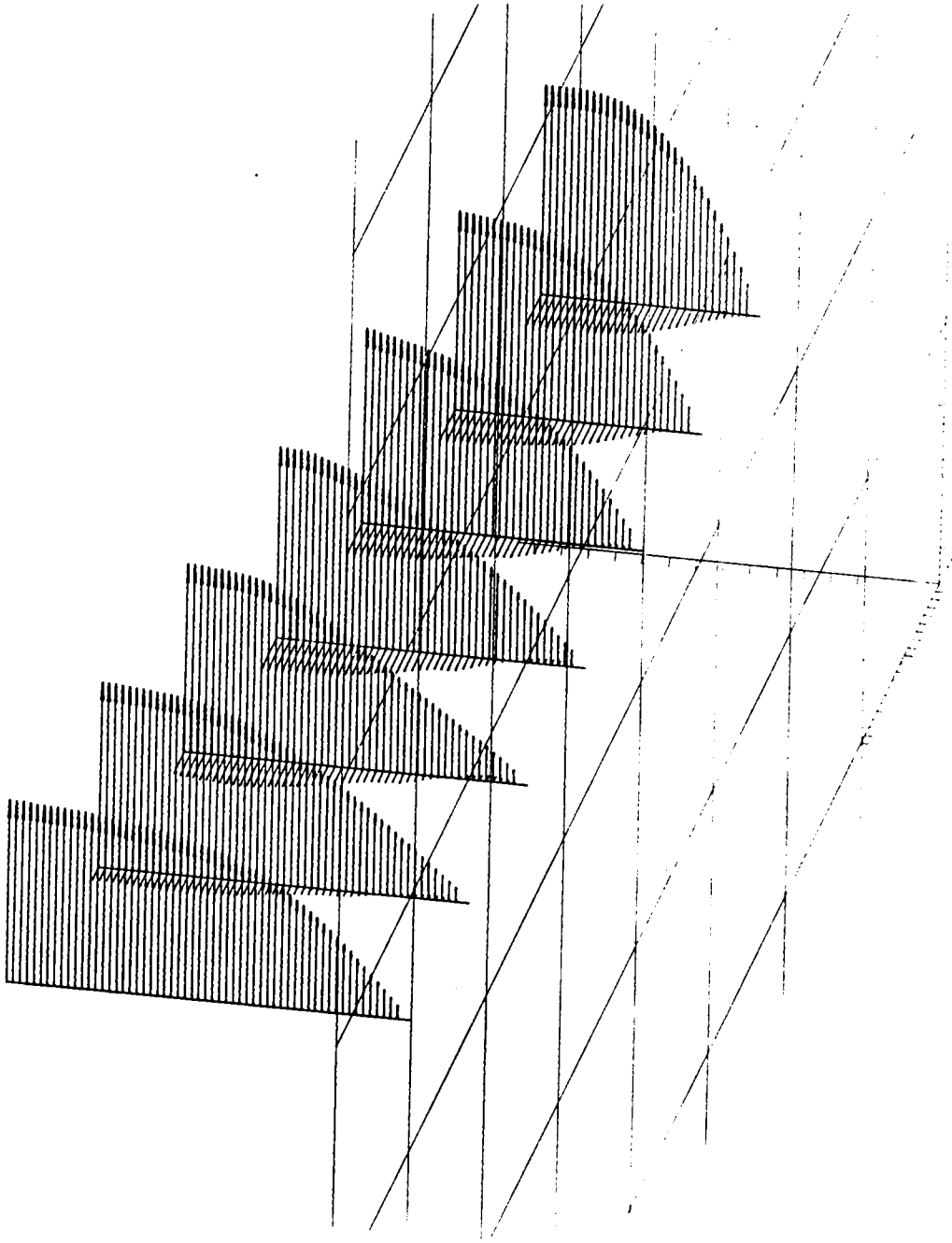

Fig. 4.22 Interpolated velocity profile at x/a = 0.45

Fig. 4.22

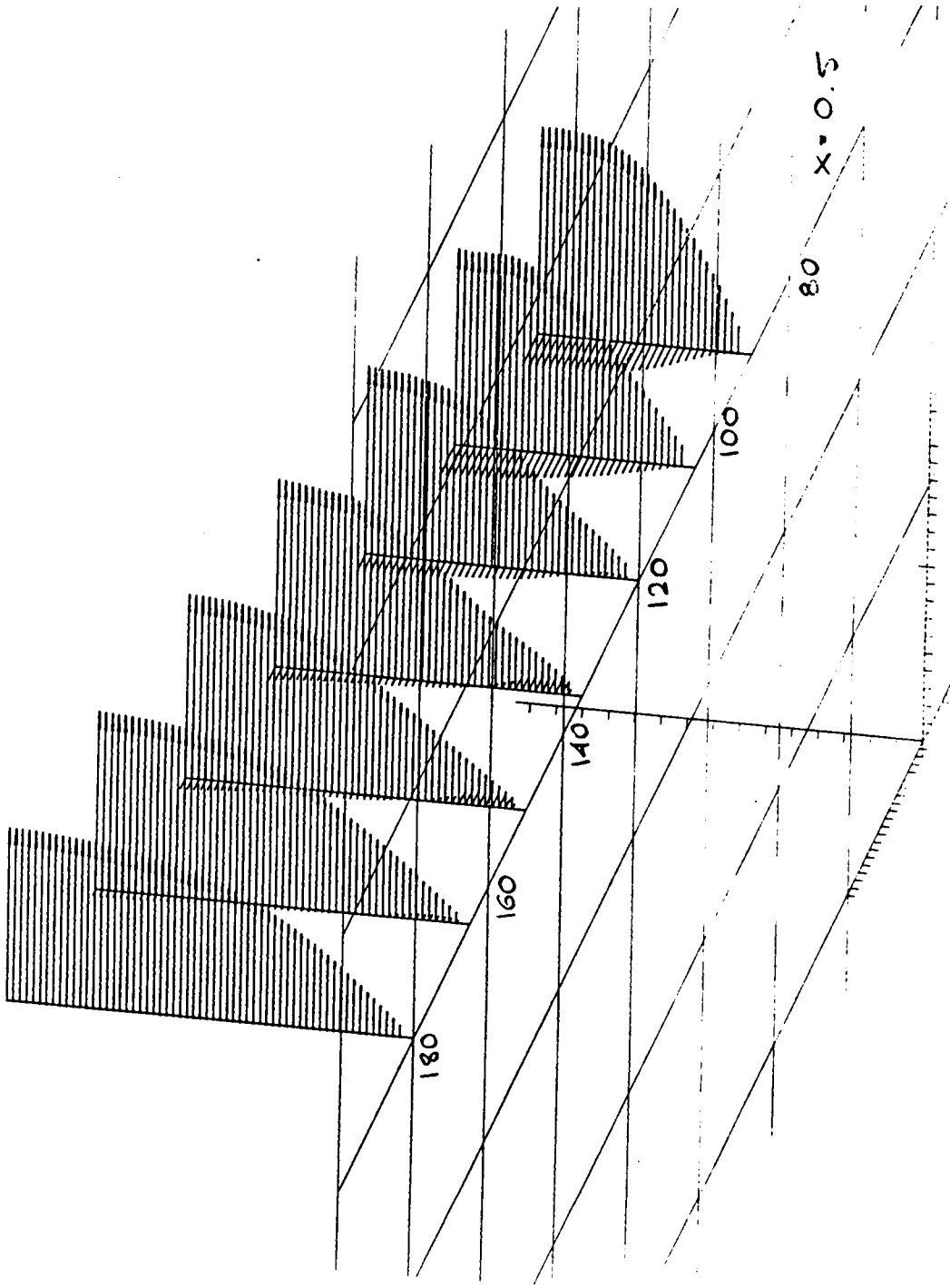

Fig. 4.23 Interpolated velocity profile at x/a = 0.5

Fig. 4.23

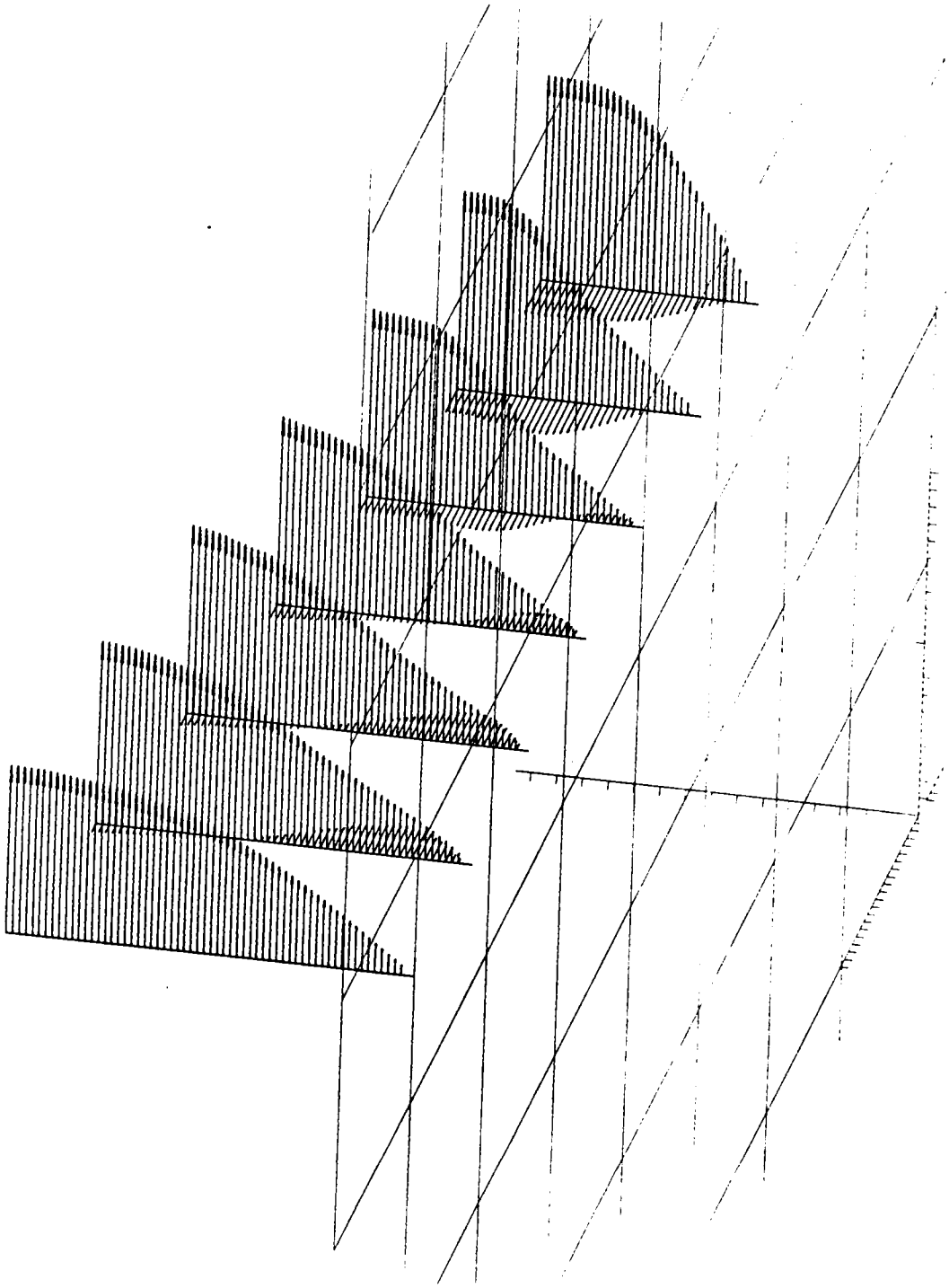

Fig. 4.24 Interpolated velocity profile at x/a = 0.55

Fig. 4.24

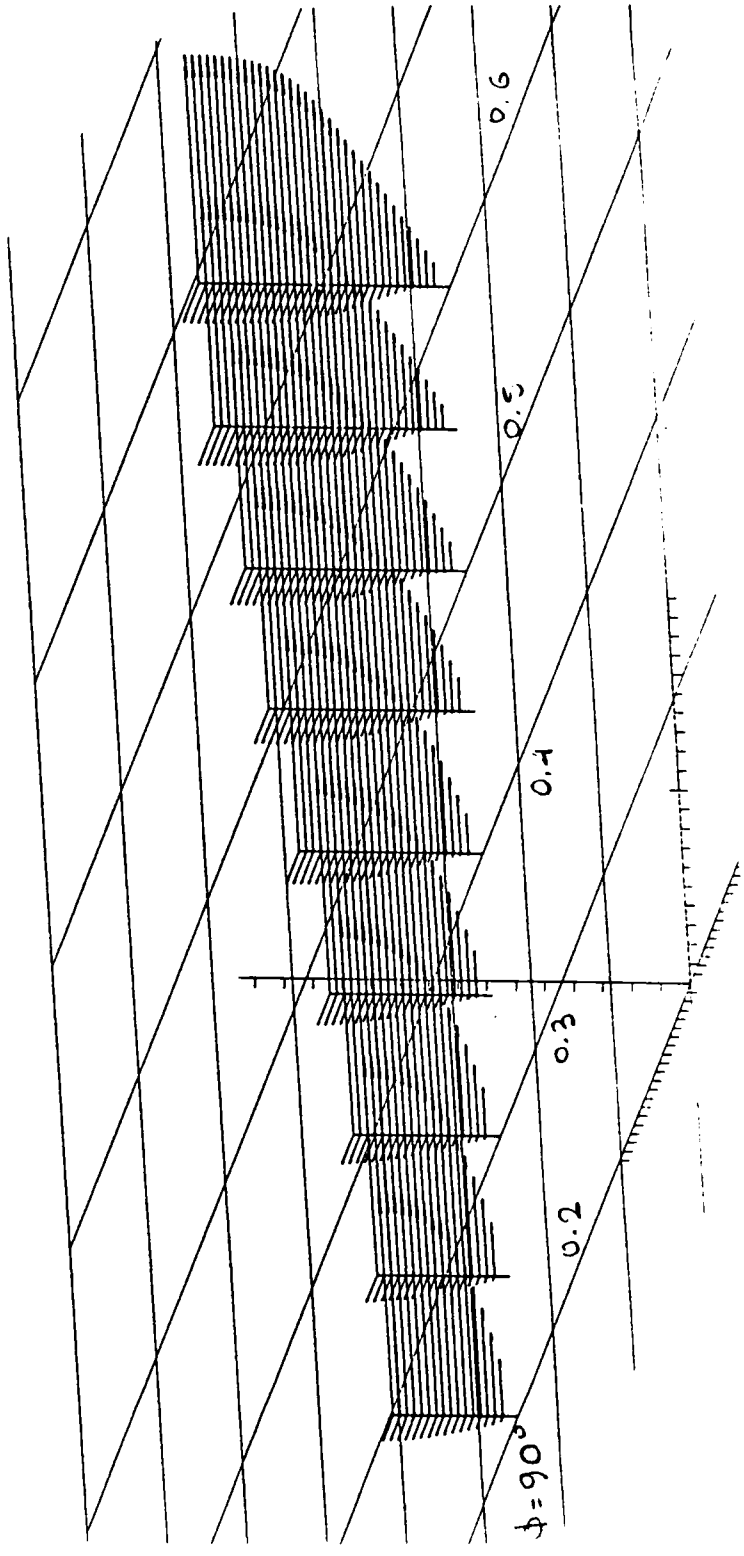

Fig. 4.25

Fig. 4.25 Interpolated velocity profile at $\phi = 90^\circ$.

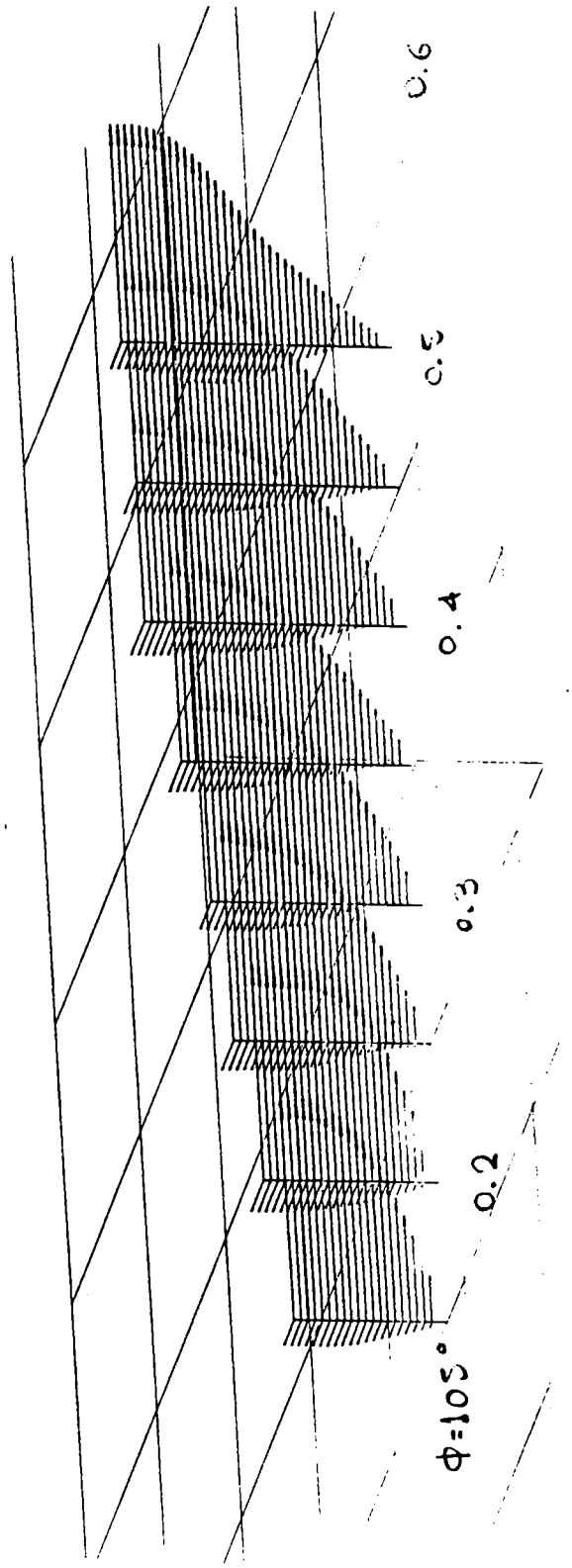

Fig. 4.26

Fig. 4.26 Interpolated velocity profile at ϕ = 105°

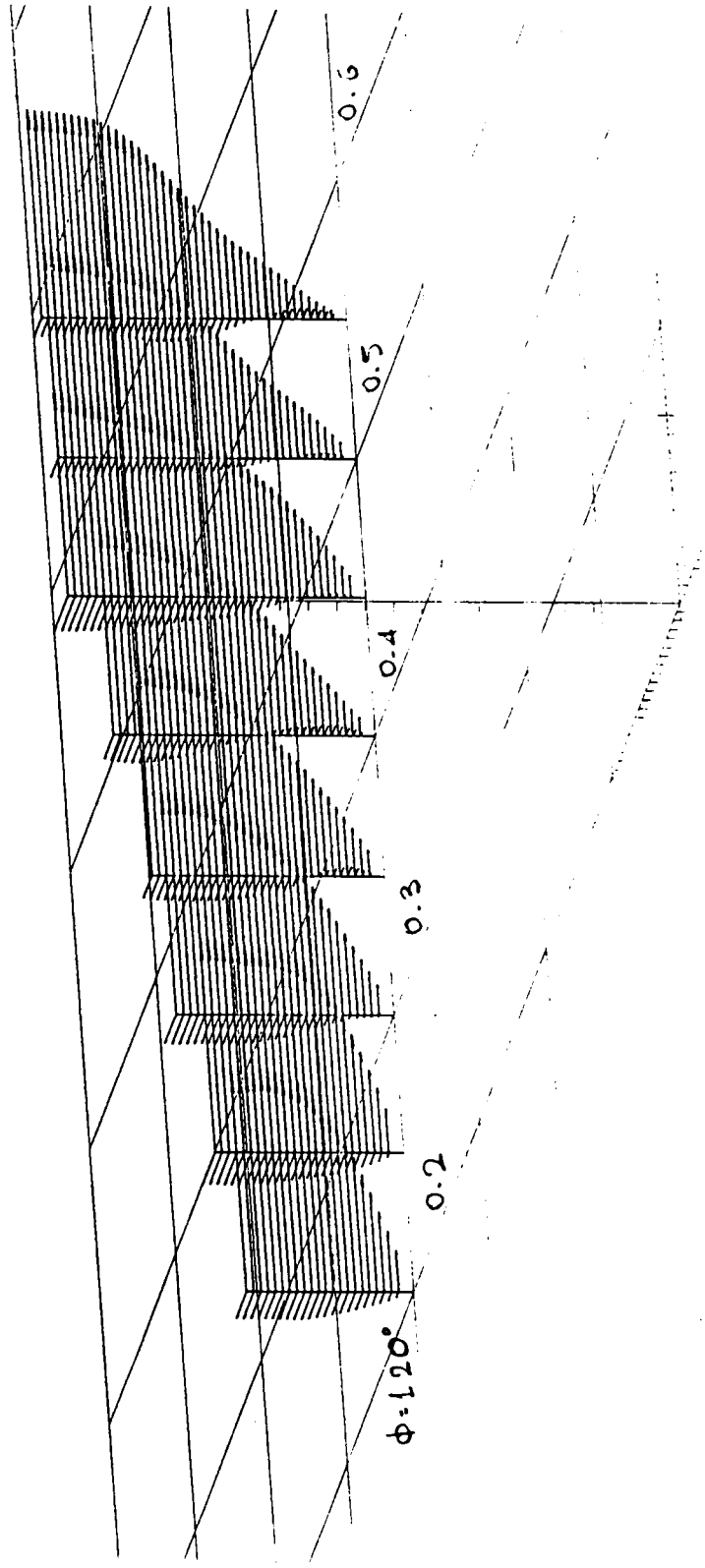

Fig. 4.27

Fig. 4.27 Interpolated velocity profile at ϕ = 120°

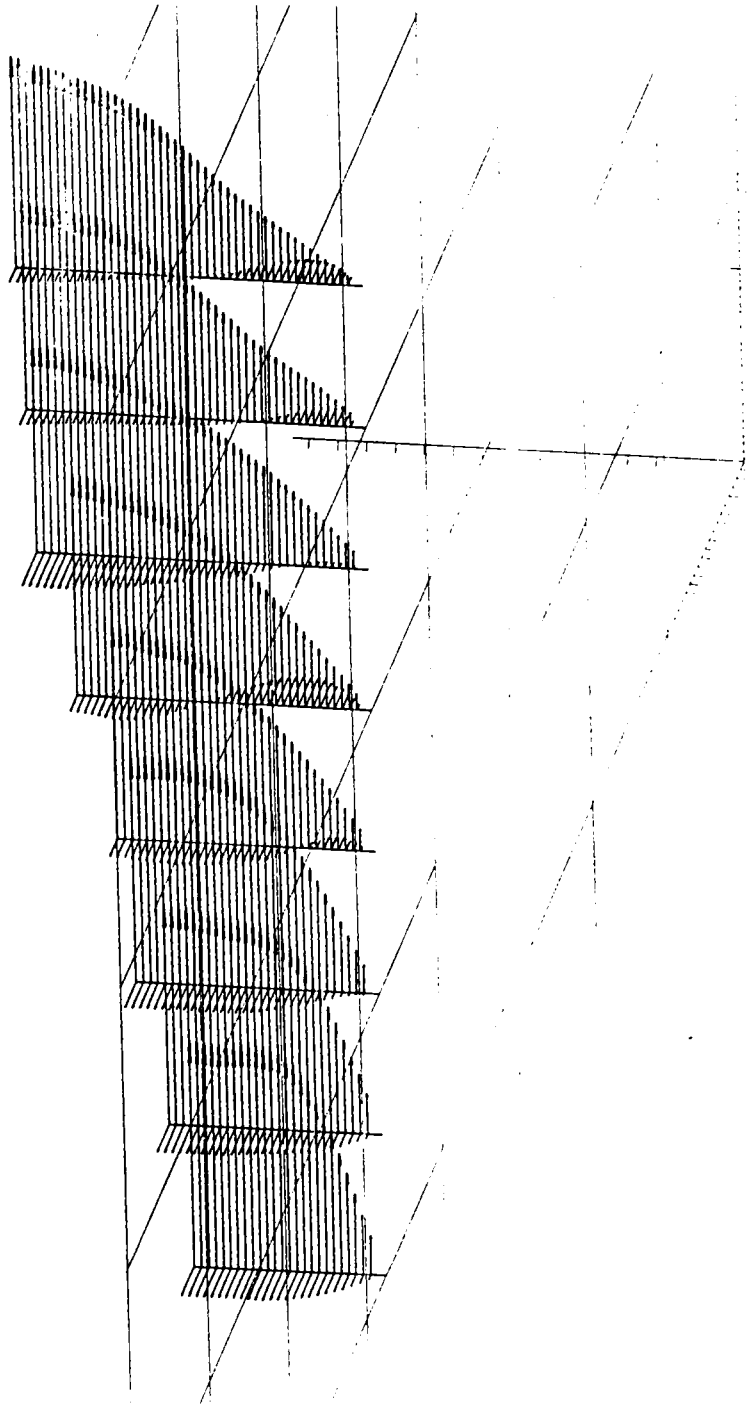

Fig. 4.28 Interpolated velocity profile at $\phi = 135°$.

Fig. 4.28

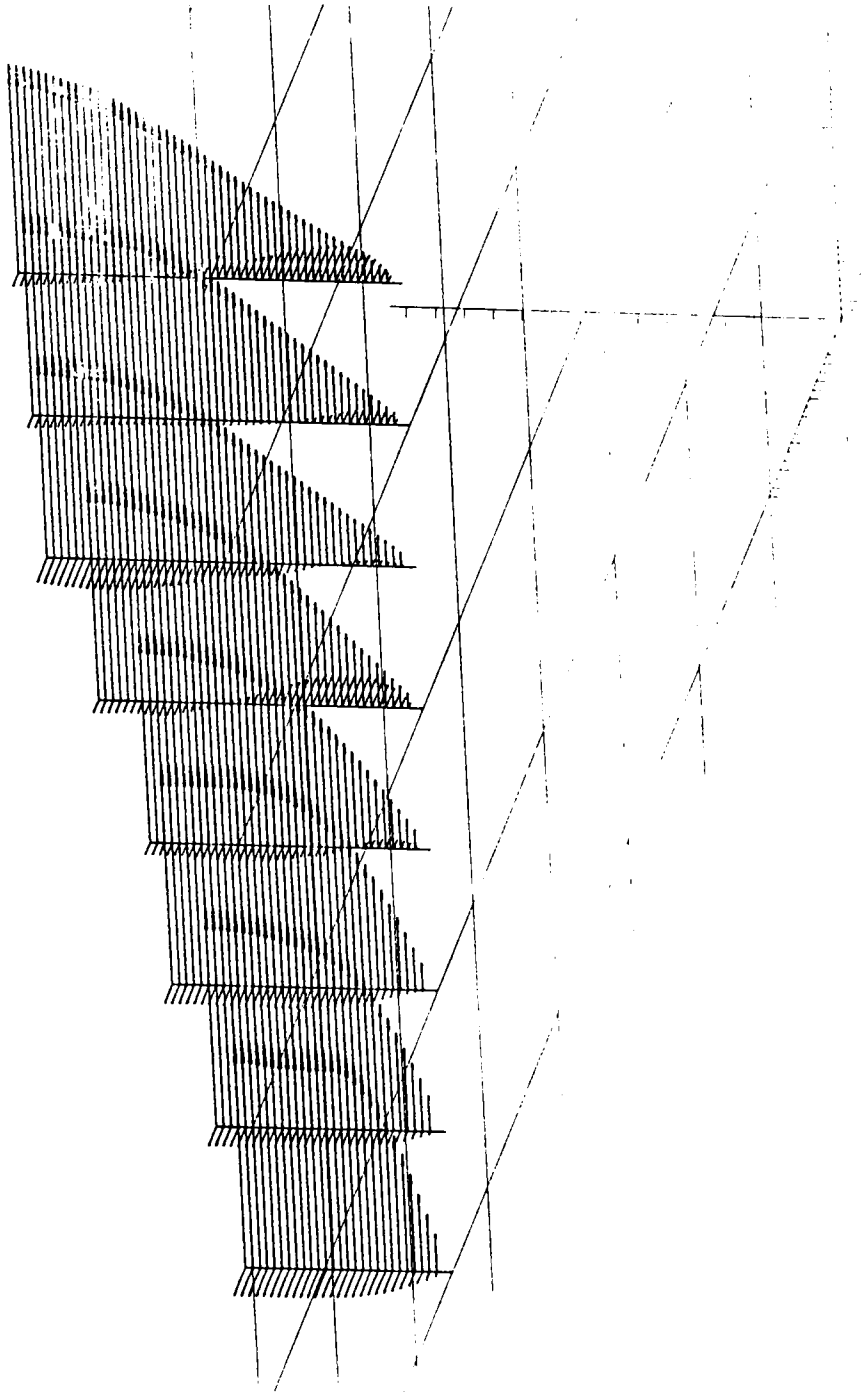

Fig. 4.29 Interpolated velocity profile at $\phi = 150^{\circ}$.

Fig. 4.29

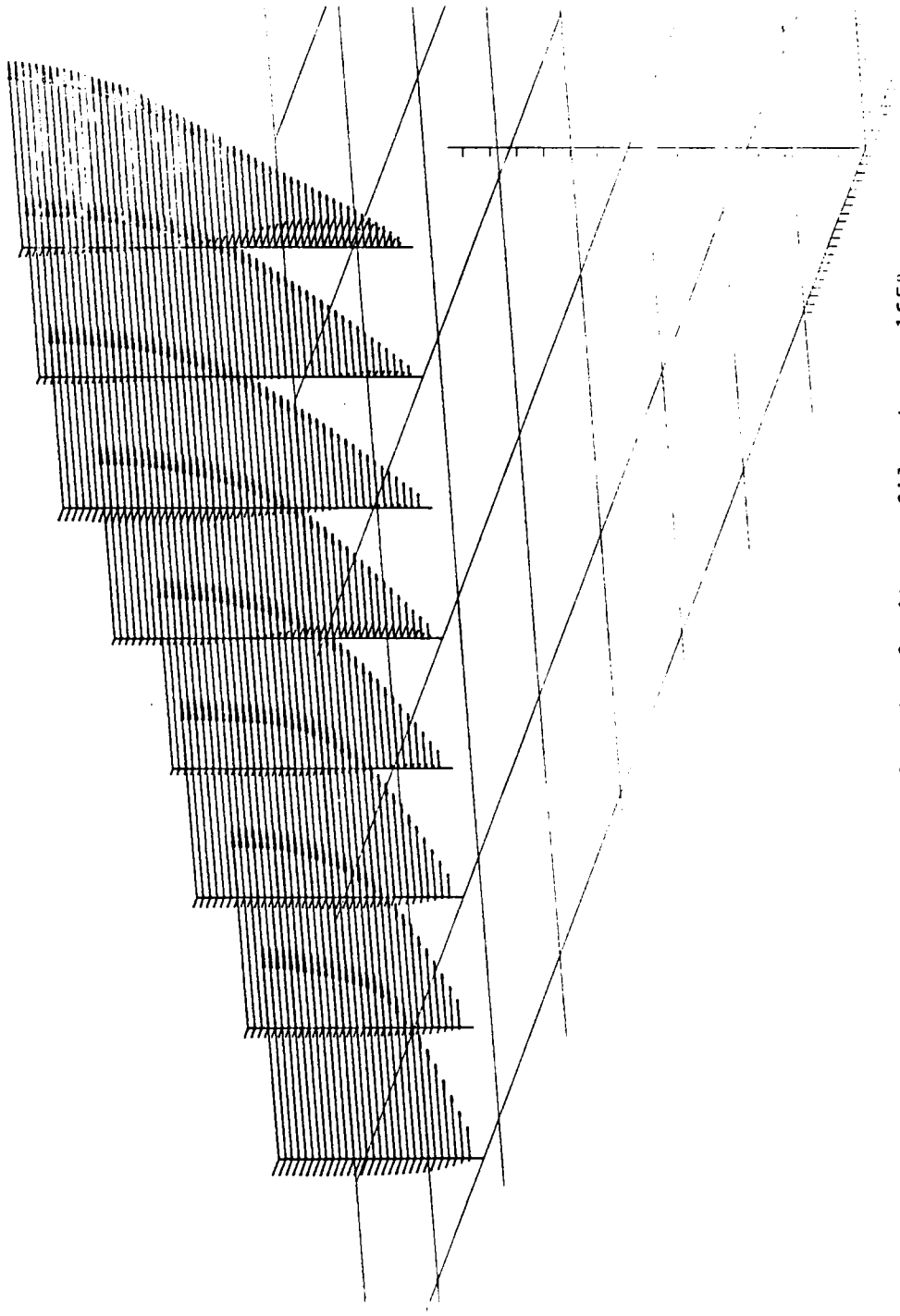

Fig. 4.30 Interpolated velocity profile at $\phi = 165°$.

Fig. 4.30

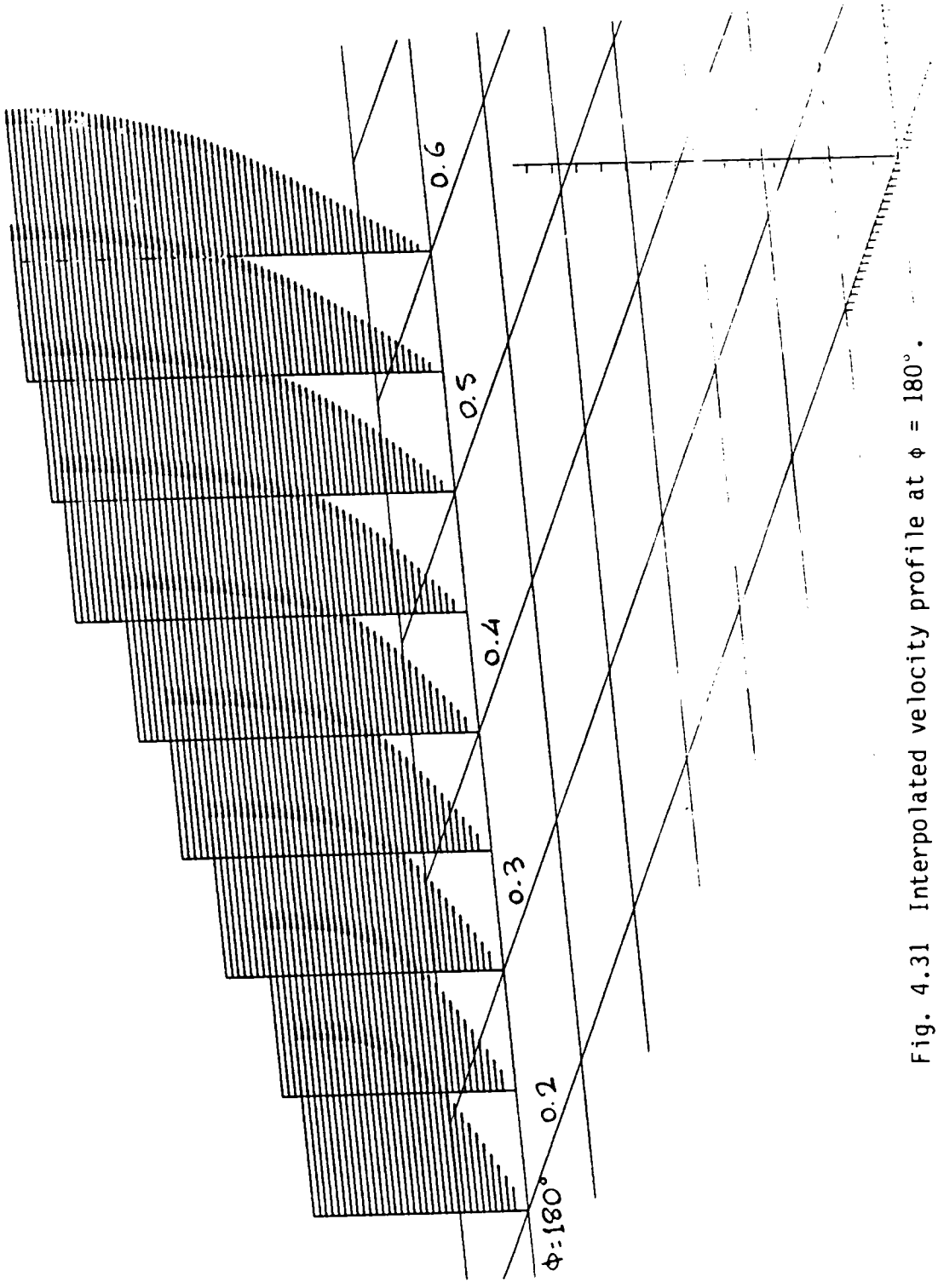

Fig. 4.31 Interpolated velocity profile at $\phi = 180°$.

Fig. 4.31

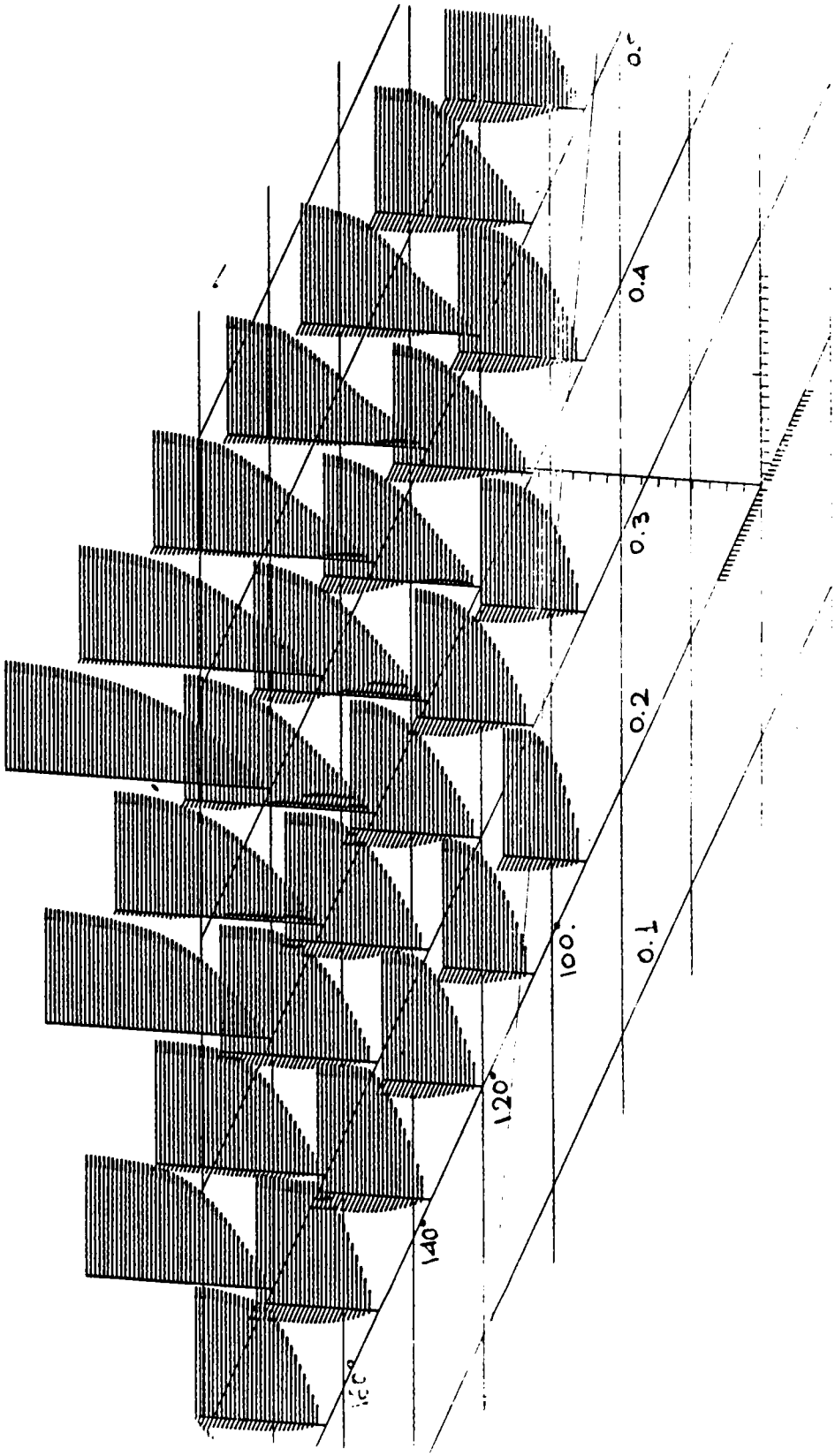

Fig. 4.32

Fig. 4.32 Composite of interpolated profiles at x/a = 0.2, 0.3, 0.4 and 0.5.

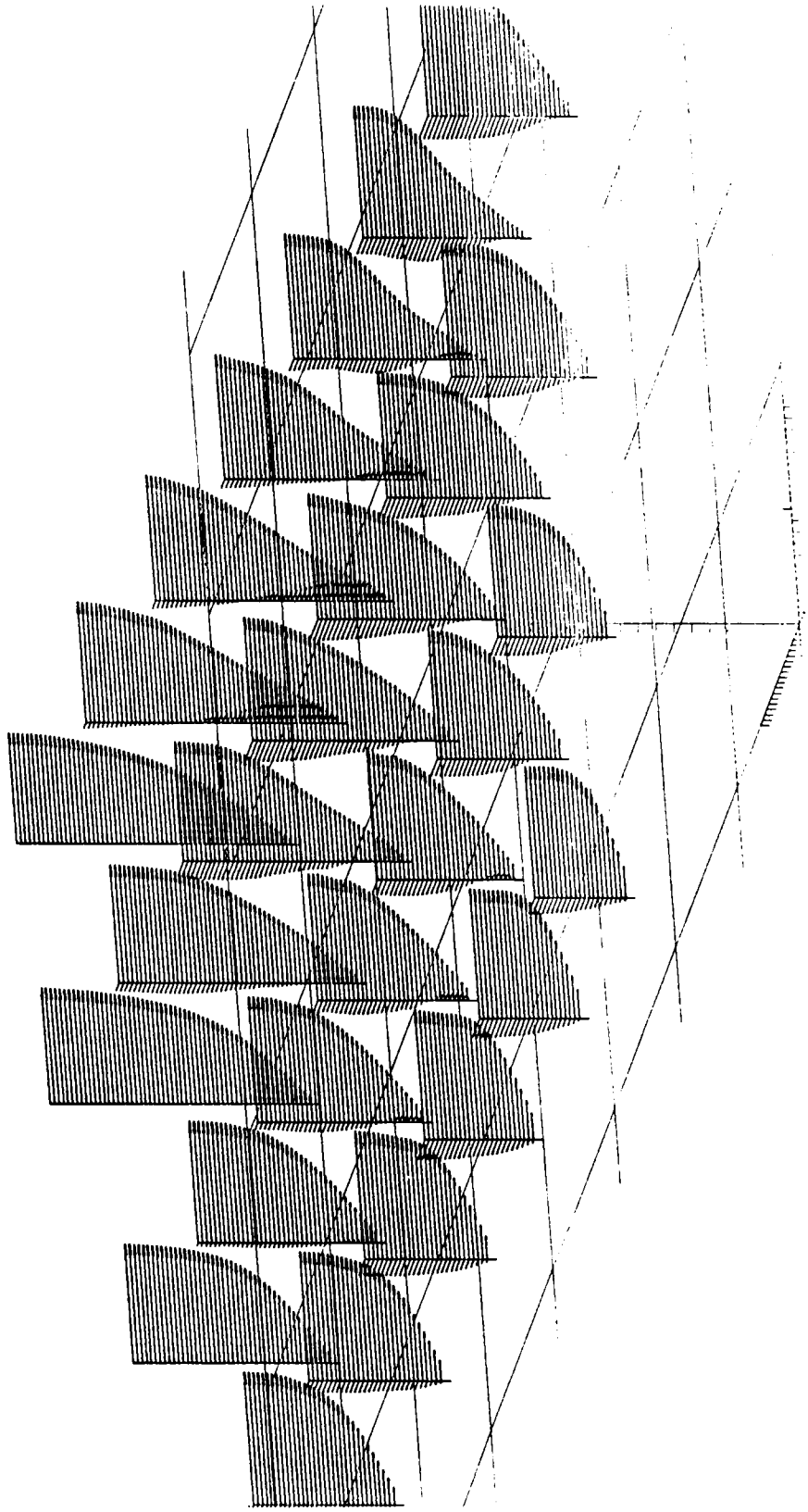

Fig. 4.33 Composite of interpolated profiles at x/a = 0.25, 0.35, 0.45 and 0.55.

Fig. 4.33

CHAPTER V

THE VORTEX LATTICE METHOD

5.1. Introduction

Aerodynamic problems involving massive regions of separated flow in 3 dimensions can be treated today numerically only by methods of discrete vortex dynamics. Navier-Stokes codes would require incredible amounts of computer time and space to generate the solution to a practical problem. In two dimensions, a variety of problems have been considered, as for example the stability of free-shear layers and the wake structures of thin plates or cornered bodies. More related to the present contribution are works considering the problem of separation over bluff bodies; the most popular case being the circular cylinder (Gerrard (1966), Sarpkaya (1968) and Sarpkaya and Schoaff (1979), Kuwahara (1978), Deffenbaugh (1974)). In fact the first efforts to consider separated regions over elongated three-dimensional bodies were based on the cross-flow-plane analogy which employs two-dimensional solutions in cross-sections of the body. Two-dimensional methods have been refined to include redistribution of vorticity, models for viscous dissipation, etc.

In three-dimensional problems, one set of such methods is known as "vortex-lattice methods". Problems involving sharp-edge separations have been treated in this way with considerable success for steady (Mook et al. (1974), Kandill et al. (1976), Zorea et al. (1978), Belotserkovskii (1966)) and unsteady (Atta et al. (1976), Thrasher et al. (1977), Levin & Katz (1980)) flows.

Three-dimensional flows involving separation over smooth surfaces have been considered only very recently. Fiddes (1980) expanded on a viscous-inviscid interacting method to solve the problem of three-dimensional separation over a cone. This is an elegant mathematical thesis and a revealing contribution which however is limited to slender body configurations and conical flows.

Thrasher (1983) studied the flow over a semi-infinite body with a tangent-ogive nose and a cylindrical afterbody. He employed an iteration version of a vortex-lattice scheme to solve the problem and assumed that the separation lines coincided with generators of the body. Almosnino and Rom (1983) have considered the flow about a very similar semi-infinite body and employed again an iteration method to achieve convergence of the wake vortices. However, they modeled the separated vortex sheets by only 4 vortex lines on each side emanating from very narrow segments aligned again with generators of the body.

In all investigations of three-dimensional bluff-body separated flows, the body was assumed to be semi-infinite. Moreover, with the exception of the degenerate case considered by Fiddes (1980), all other investigators assumed that the position of separation is known and that in fact it coincides with a meridional line of axisymmetric bodies. In the present paper we report on our initial efforts to relax the above restrictions. To this end, we have coupled the potential flow calculations with an approximate method of calculating the three-dimensional boundary layers. Moreover, we considered the unsteady development of the wake and allowed the viscous and inviscid fields to interact. The line of separation over a finite body was readjusted at each time step

and was found to tend to the position predicted experimentally for a fully developed flow.

5.2. Potential Flow Calculations

The outer flow and the separated vortex sheet are predicted by the vortex-lattice method. This is based on Biot-Savart's law which stipulates that the velocity vector $\bar{V}$ at position $\bar{r}$ induced by a vortex filament of strength Γ is given by

$$\bar{V}(\bar{r}) = \frac{\Gamma}{4\pi} \int \frac{d\bar{\ell} x (\bar{r}-\bar{s})}{|\bar{r}-\bar{s}|^3} \qquad (5.2.1)$$

where the variable $\bar{s}$ is a position vector of points along the vortex line. An equivalent formula for the present application gives the velocity induced by a vortex segment of finite length. With quantities defined in Fig. 5.1, the velocity is expressed as follows

$$\bar{V}(\bar{r}) = \bar{e} \frac{\Gamma}{4\pi h} (\cos\theta_1 - \cos\theta_2) \qquad (5.2.2)$$

where $\bar{e}$ is a unit vector normal to the plane defined by the point of interest and the vortex segment.

The velocity field calculated by the superposition of quantities of this form is irrotational except along the vortex lines which represent singularities of the solution. Appropriate distributions of vorticity along fixed or moving grids can be used to generate solutions of incompressible flows in 2 or 3 dimensions with or without separation. As a test for 3-dimensional bluff bodies we considered 3 basic problems which

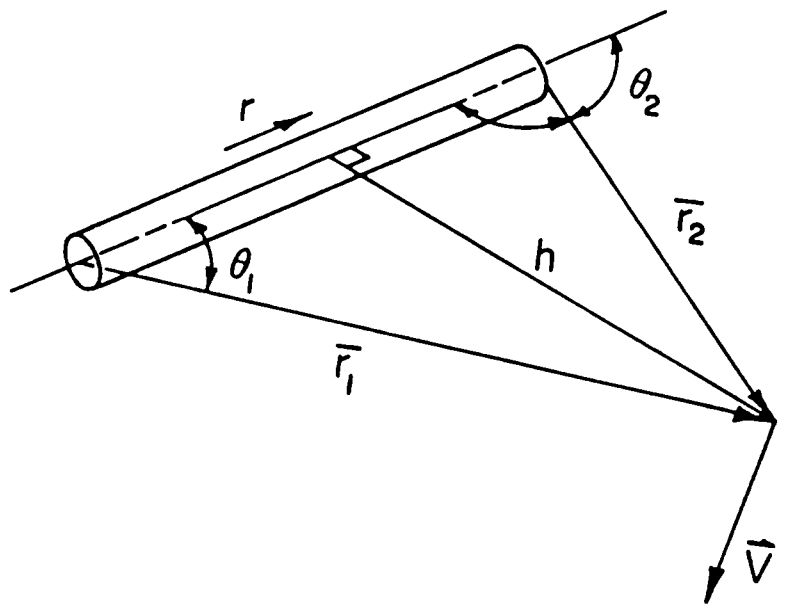

Fig. 5.1 Velocity induced at a point due to a vortex segment.

accept exact closed-form analytical solutions, readily available for comparison: the flow about (a) a sphere, (b) a prolate spheroid and (c) a general ellipsoid. To solve these problems, vortex-lattices have been defined with their nodes on the surface of the body as shown in Figs. 5.2 and 5.3. The strength of each vorticity segment, usually referred to as branch circulation is denoted by the symbol Γ. Most investigators working in this area (Mook et al. (1974), Kandil et al. (1976), Atta et al. (1976), Thrasher et al. (1977)) express Eq. (5.2.2) in terms of the loop circulation, G, around a panel of the vortex lattice. The branch circulation Γ is simply the difference of the loop circulations of its two neighboring panels, G_1 and G_2

$$\Gamma = G_1 - G_2 \tag{5.2.3}$$

The branch circulations thus defined automatically generate a divergence-free vortex sheet which is a classical property of vorticity.

For convenience of the notation, consider a case of N panels with N unknown loop circulations G_j, $j = 1,\ldots N$. These quantities can be specified by imposing the no-penetration condition at N points on the body. We chose here the "average control points", namely the centroids of the panels. However, we project these points on the actual surface of the body under cosideration. The influence matrix A_{ij} is first constructed. An element of this matrix is the value of the normal velocity at the ith control point due to vorticity distributed around the jth panel with a unit loop circulation. The no-penetration condition then is simply expressed as follows

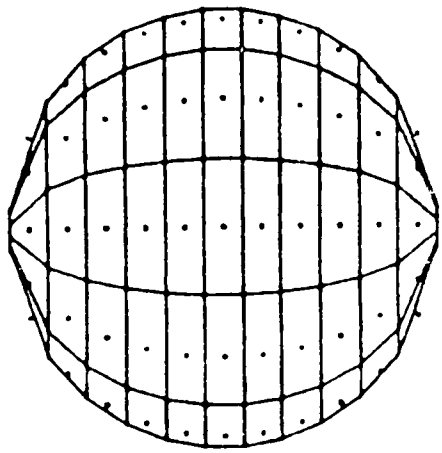

Fig. 5.2 Vortex lattice and control points for a sphere (10 circumferential and 11 axial panels).

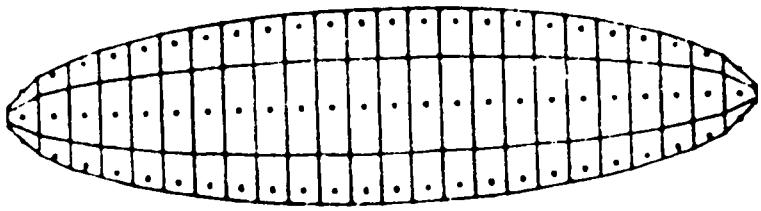

Fig. 5.3 Vortex lattice and control points for an ellipse with axes ratio 1:4 (6 circumferential and 25 axial panels).

$$\sum_{i=1}^{N} A_{ij} G_j = \bar{V}_\infty \cdot \bar{n}_i \qquad (5.2.4)$$

where $\bar{V}_\infty$ is the free stream and $\bar{n}_i$ is the normal to the body at the point i. The solution of this system for the quantities G_j can generate the flowfield about the body under consideration.

Typical results obtained by such calculations are shown in Figs. 5.4 and 5.5 where we compare the velocity distribution along a meridional calculated by the exact method and the vortex lattice method. The results displayed in these figures correspond to an optimum choice of panel dimensions. Surprisingly, the accuracy of the calculation is improved by adding elements in the axial direction alone. Excellent results were obtained for example with 27 panels in the axial direction and only 6 or even just 4 in the circumferential direction.

Separated flows can be calculated by approximating the separated vortex sheets again by vortex lattices (Fiddes (1980), Thrasher (1983), Almosnino & Rom (1983)). In the present case we chose to consider impulsively started flows. The steady state will then be obtained as a limit for large times. At present and mostly due to limitations in computing time, we have not obtained large time solutions. However, the present results display some very encouraging characteristics.

Kelvin-Helmholtz' theorem dictates that vorticity be transported with the local velocity. This condition automatically generates a force-free wake and is used here in a manner similar to the one descibed in earlier references (Atta (1976), Thrasher (1977), Levin (1980)). The main difference here is that the wake is initiated along a line of

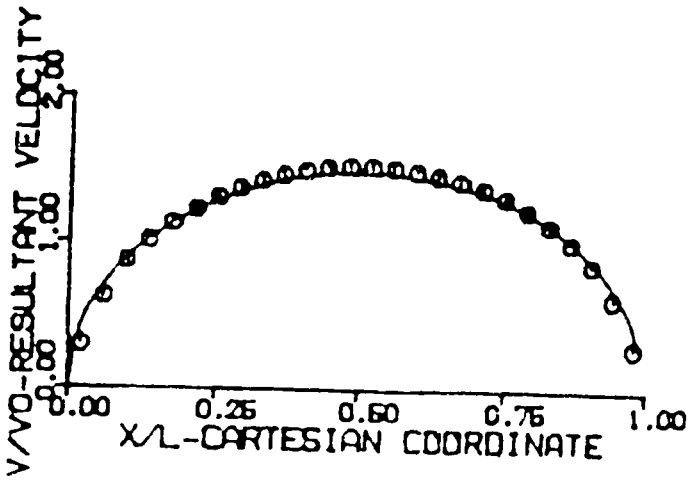

Fig.5.4 The velocity distribution along the meridional of a sphere. ———, exact solution; ∘, vortex lattice with 6x27 circumferential x axial panels.

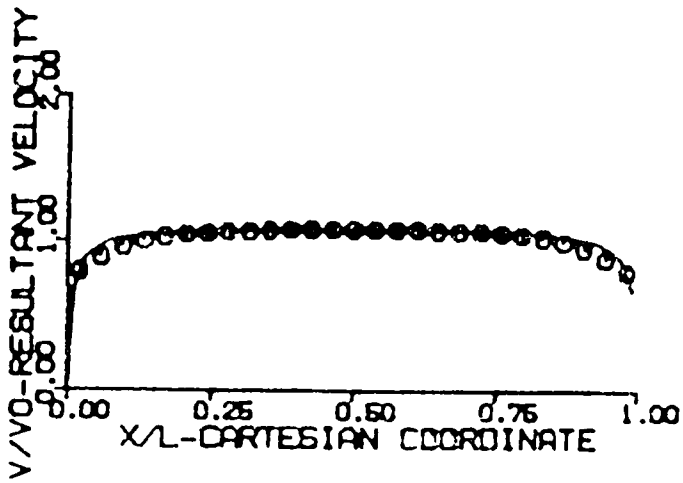

Fig.5.5 The velocity distribution along the meridional of a prolate spheroid at zero angle of attack. ———, exact solution; ∘, vortex lattice with 4x28 circumferential x axial panels.

separation which is determined by a viscous calculation and is free to readjust at each time step.

The shed vorticity in the form of 2 rows of panels at the root of the separated vortex sheets are determined at each time step from viscous-inviscid interaction as described in Section 5.3. In the next time step this row of panels is convected away from the body and a new row of panels is generated in the same way. The free vortex panels must be accounted for in the calculation of the velocity field. Equation (5.4) must be modified to include $\bar{V}_w$, the velocity induced by the wake

$$\sum_{i=1}^{N} A_{ij} G_j = (\bar{V}_\infty + \bar{V}_w) \cdot \bar{n}_i \qquad (5.2.5)$$

It should be noted that the matrix A_{ij} is universal for a certain body configuration, but the calculation of the velocity $\bar{V}_w$ although tedius and time consuming, must be repeated at each time step. Finally, the system of Equations (5.2.5) is non-singular and can be solved with the same routine used to solve Equations (5.2.4).

5.3. Viscous Inviscid Interaction

The boundary layer was calculated by the approximate method described in Chapter II. The method is based on the assumption that the boundary-layer flow over a general body is locally similar to the flow over a special body whose solution is readily available. Such bodies are cylinders of arbitrary cross section at yaw with respect to the oncoming flow.

In the present problem we allow the boundary layer to interact with the outer flow only through separation. The strength of the vorticity shed at separation and the location of the line of separation control the development of the free vortex sheets which roll up forming the wake. The structure of the flow at separation and the mathematical modeling that allows the two solutions, the viscous and the inviscid to interact with each other is of crucial importance.

The topology of skin friction lines has been studied extensively in 3-dimensional boundary layer flows. Experimental evidence and numerical information indicate that the skin friction lines merge together along the line of separation. Recent careful boundary-layer calculations (Cebeci et al., (1981)) point to the direction that the separation line is an envelop of skin friction lines and therefore, within the framework of uninteracted boundary-layer theory, a singular behavior should be expected there. It is therefore justified to use the Sears model for the construction of local-similarity solutions since it is also singular along the line of separation.

It is well known that the vortex lines on the surface of the body are orthogonal to the skin friction lines. This implies that the surface vortex lines meet the line of separation at an angle of 90° and lift off the body surface also perpendicular to the line of separation. Incidentally, this is contrary to the common concept of two-dimensional separation where, in principle, surface vortex lines are parallel to the line of separation. The author and his associates have obtained some experimental evidence that in two-dimensional flows, well organized cells of cross flow are present in the neighborhood of separation. It

is therefore possible that all separation lines are lines of zero vorticity. The picture described above is actually the limit of the behavior of streamlines and vortex lines as the distance from the wall tends to zero. Actually the total amount of vorticity parallel to the line of separation contained in the boundary layer is not at all zero at separation. In fact it is the amount which the boundary layer sheds in the wake.

A straightforward integration of vorticity across the boundary layer indicates that, within the boundary-layer approximation, the magnitude of the vorticity flux at a station of the boundary layer is proportional to the square of and its direction is normal to the direction of the edge velocity. This fact has been employed extensively in investigations of 2-dimensional flows and was lucidly explained again by Sears (1948). The idea is that in approximating the shed vorticity by discrete potential vortices, as shown schematically in Fig. 5.7a, the strength of the nascent vortices must be compatible with the vorticity contained in the boundary layer. For a straightforward derivation of the classical formula, consider the circulation about the loop ACOO' shown in Fig. 5.7b.

$$\Gamma = \int V \cdot d\ell = \iint \Omega \cdot dA \qquad (5.3.1)$$

For steady flow, the time derivative of the integral on the right-hand side vanishes, except for a contribution along the side OO' which allows vorticity to be convected outside of this domain.

$$\frac{d\Gamma}{dt} = \int_0^\delta u\Omega dy \qquad (5.3.2)$$

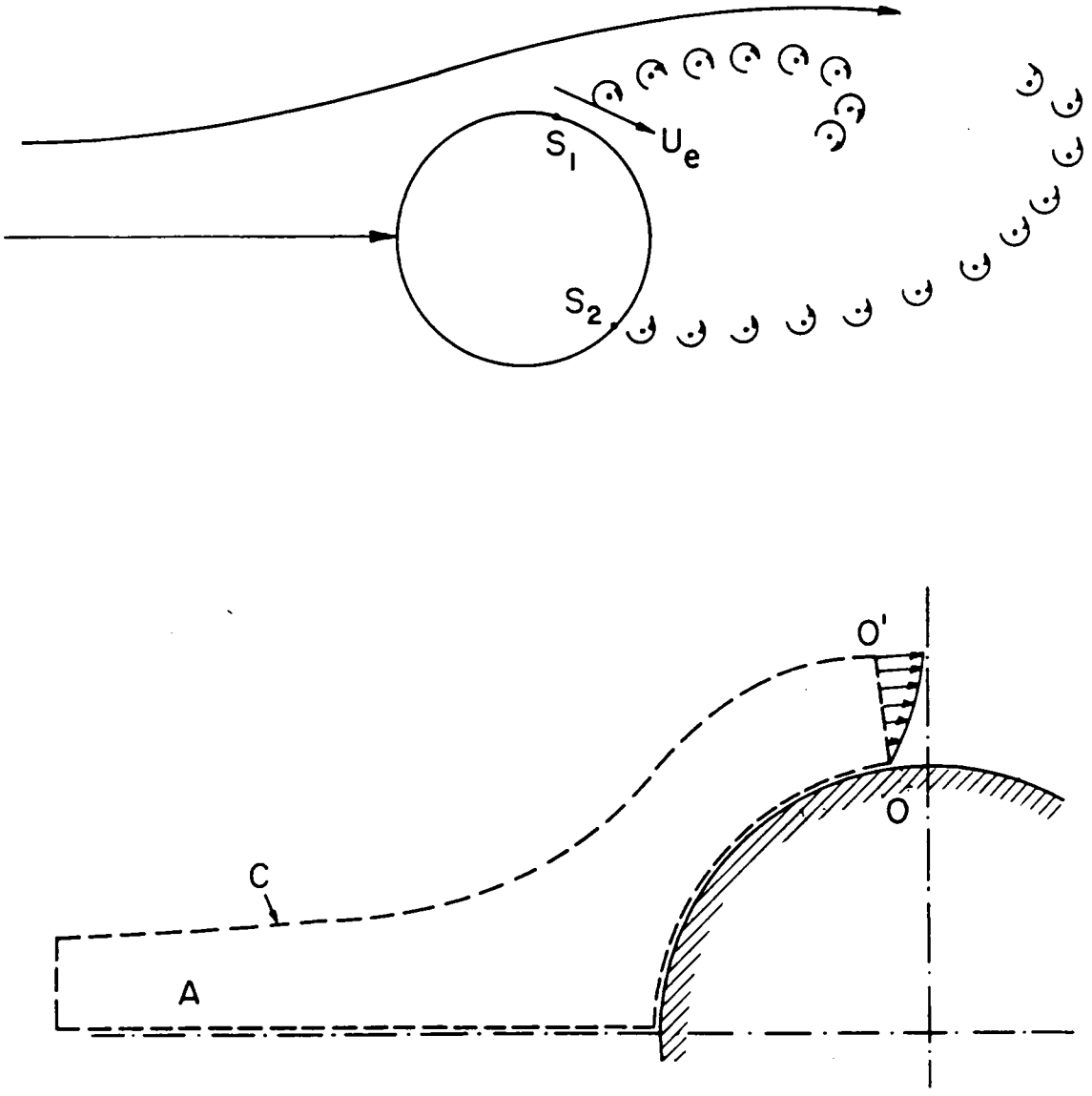

Fig. 5.7 Vorticity field in 2 dimensions.
(a) Schematic of discrete vortex shedding at the separation points S_1 and S_2
(b) The contour of integration for the circulation.

And within the boundary-layer approximation, $\Omega \sim \partial u/\partial y$ we have

$$\frac{d\Gamma}{dt} = \frac{1}{2} U_e^2 \tag{5.3.3}$$

where U_e is the velocity at the edge of the boundary layer. This condition is extended below for 3-D flows and is employed to calculate the strength of the nascent vortices at each time step.

Consider a three-dimensional boundary layer over a solid surface aligned with the coordinate plane xy. In the notation of Fig. 5.8 then the flux of vorticity can be represented by two vectors which can be obtained by similar integrations across the boundary layer

$$\frac{d\Gamma_x}{dt} = \frac{1}{2} U_e^2, \quad \frac{d\Gamma_y}{dt} = \frac{1}{2} V_e^2 \tag{5.3.4}$$

What is of great importance and interest here is that nascent vorticity is parallel to the wall but not necessarily parallel to the line of separation. This is because by definition the vorticity vector in an attached boundary layer is parallel to the wall. The vorticity vector, therefore, is normal to the edge velocity which in turn is <u>not</u> normal to the line of separation. If we need to discretize the nascent vorticity, then we can simply resolve it in components parallel and perpendicular to the line of separation but always parallel to the surface of the body as shown schematically in Fig. 5.8. Let the plane yz in this figure be a plane of separation. Since vorticity is convected with the flow, the vorticity vector $\Delta\Gamma_y$ parallel to the line of separation remains unchanged as it passes over to the free shear layer. However, the

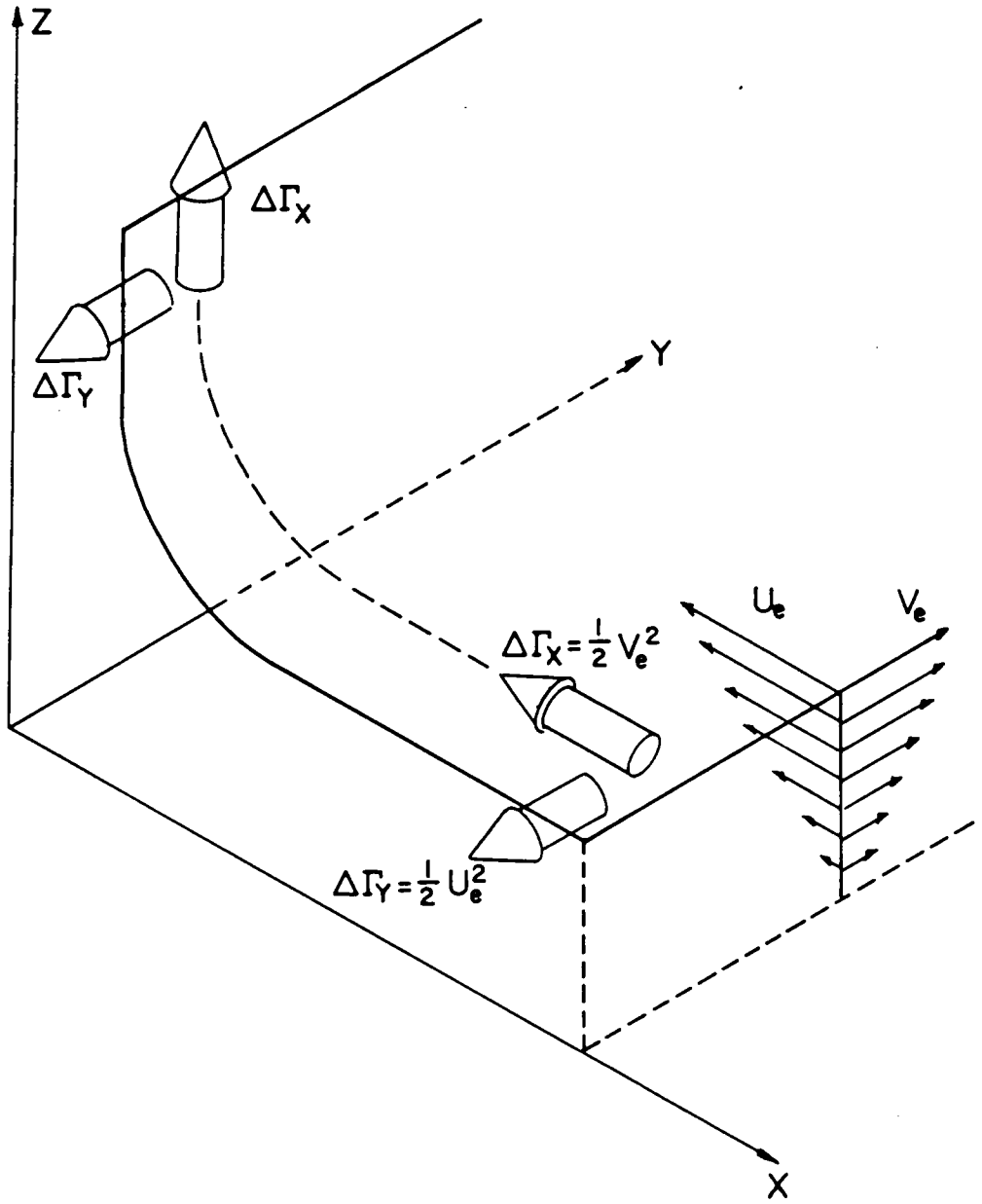

Fig. 5.8 The boundary layer and total vorticity flux near separation. The plane xy is on the surface of the body. The plane y,z is a separation surface.

vector $\Delta\Gamma_x$ is turned to align itself with the flow direction, as shown again in Fig. 5.8. This condition was implemented in the numerical scheme employed here.

A discretization scheme of the free vortex sheet originates with a ribbon of rectangular elements. The surface of the ribbon was assumed to be parallel to the surface of the body at an arbitrary distance of 0.2R where R is radius of the cross section of the body at the station under consideration. More properly, this distance should be a length proportional to the displacement thickness of the boundary layer. The outer nodes of the ribbon were allowed to be convected and a new ribbon of vorticity was generated according to the above scheme. In this way a free vortex sheet was generated.

5.4 Results and Discussion

Two types of problems were solved with the codes developed here. The initial condition for both problems was the potential flow about the body. In the first problem we assumed that the boundary layer develops in a quasi-steady way but the vortex sheets develop in time and grow, feeding their influence back into the freestream and the boundary layer. In this formulation we allow the line of separation to relax and relocate. This is therefore an interactive method. In the second problem we specify the line of separation either aribtrarily or we use experimental data as for example the data of Meier et al. (1980). No boundary layer solution is then necesssary. However, the solution is again developed iteratively, by allowing the vortex sheet to grow as time increases.

The first solution was constructed as follows. A set of skin friction lines based on the exact potential flow solution was calculated first. For a prolate spheroid with axes ratio 1:4 the result is shown in Fig. 5.9a. The strength of the nascent vortices was then calculated and allowed to drift with the local velocity. The inviscid flow problem, namely Eqs. (5.2.5) were solved again to determine to new loop circulations on the body. With the updated potential flow, a new set of skin friction lines was calculated to determine a new envelope, namely the new position of the line of separation. Once again the strength of the nascent vortices was calculated. The free vortices were then convected again by increments proportional to the local velocities. The process was then repeated for a total of 6 time steps.

Figures 5.9b-e display the development of the vortex sheet after the 3rd and through the 6th time step for a prolate spheroid at an angle of attack of $\alpha = 30°$, started impulsively from rest. In these plots, the thick lines on the body are the skin friction lines and the thin lines are the inviscid streamlines. The line of separation is clearly identified in all figures as an envelop of the skin friction lines. The separated vortex sheets are shown in the form of a grid which at the nth time step is made up of n ribbons.

It is clearly desirable to allow the calculation to march to higher values of time. It is felt that 6 time steps are not enough for the full development of the wake. However, at larger time steps numerical instabilities develop which destroy the smoothness of the wake. Figure 5.10 displays the displacement of the line of separation as the flow interacts with the boundary layer. It is seen that a boundary layer

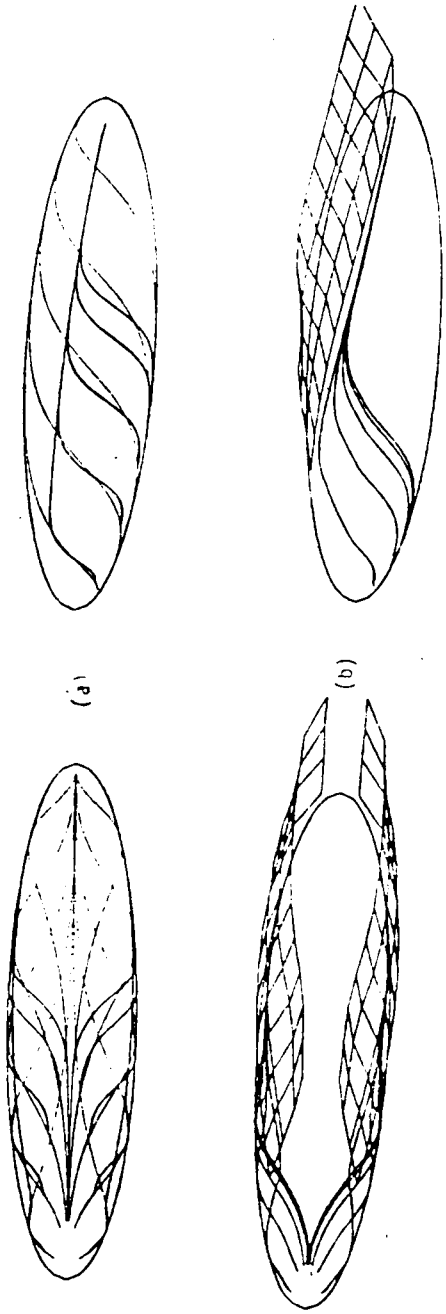

Fig.5.9 Skin friction lines, separation and separated vortex sheets over a prolate spheroid started impulsively from rest (a) t = 0, (b) t = 3Δt, (c) t = 4Δt, (d) t = 5Δt, (e) t = 6Δt.

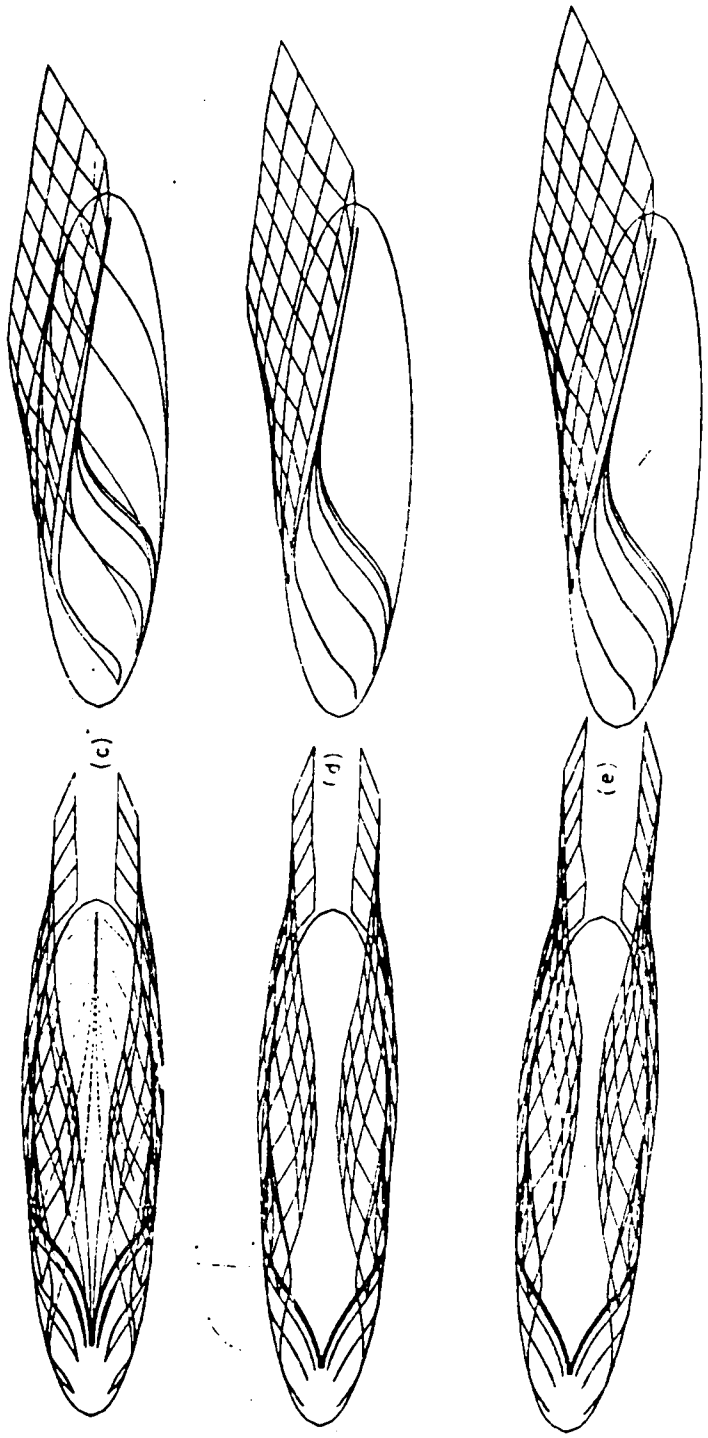

Fig.5.9 continued

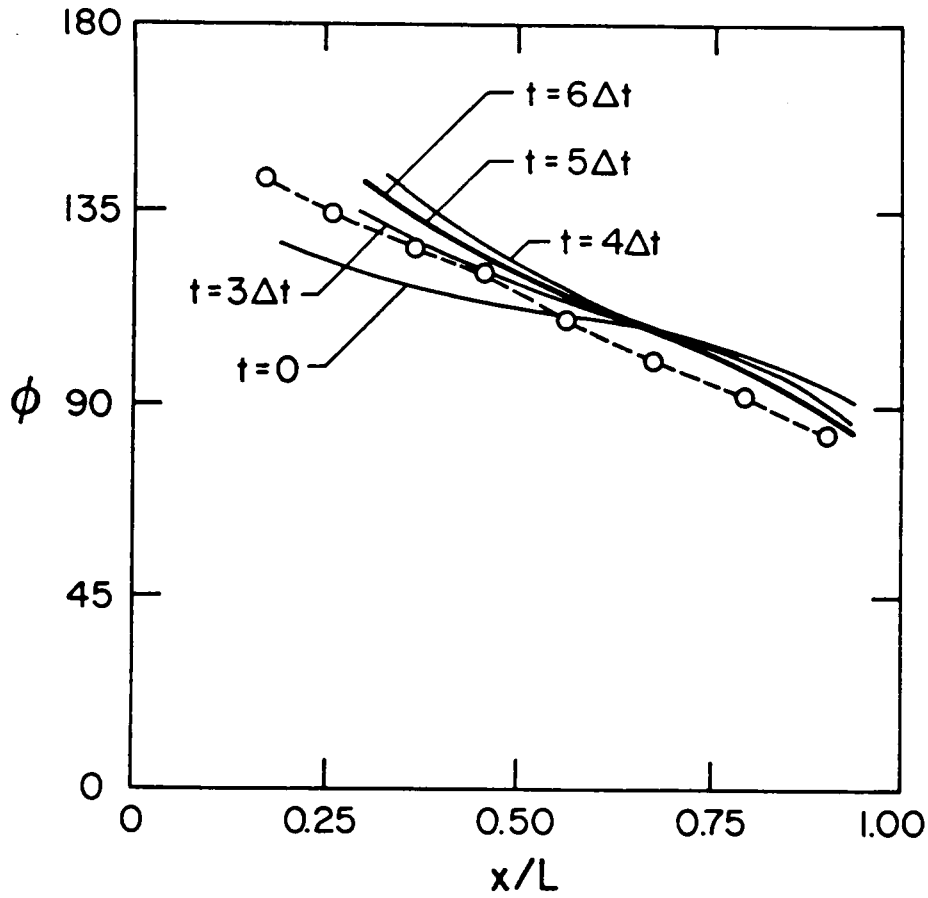

Fig. 5.10 The instantaneous line of separation for a prolate spheroid started impulsively from rest.

calculation based on the potential outer flow predicts very early separation in the forward portion of the body. This is the universal finding of researchers who employed a wide variation of boundary-layer calculations as shown in Fig. 5.11. It should be noted that our simple method for the calculation of a 3-D boundary layers with a potential, unseparated outer flow is in excellent agreement with many other complex methods.

In Fig. 5.12 we display the direct comparison of flow visualizations with our calculation. The streaklines in this figure were obtained by dyes released in the windward side of the model. The dyes are aligned more or less with the skin friction lines. Moreover, they turn sharply along the line of separation and lift off along the vortex sheet. It should be emphasized here that the first vortex line, the nascent vortex is located at a distance 0.2R above the body. As a result, if viewed perspectively from an angle of $\phi = 90°$ or 110°, the vortex line is projected on the separation line only if its polar coordinate is $\phi = 90°$. For larger ϕ's, there is a discrepancy proportional to $(0.2R)\sin\phi$, as shown schematically in Fig. 5.13. This explains partially the deviation in Fig. 5.12 between the vortex line and the separation line at the leading part of the body, where both curves tend to the windward side, i.e. larger values of ϕ.

A few other configurations were tested with our interactive code as well. Here we present two examples: an ellipsoid with axes ratios 1:6:4 and a projectile shape. Results for the ellipsoid at angle of attack of $\alpha = 30°$ are displayed in Fig. 5.14, representing the first instant as well as the 5th time step after the impulsive start. In Fig.

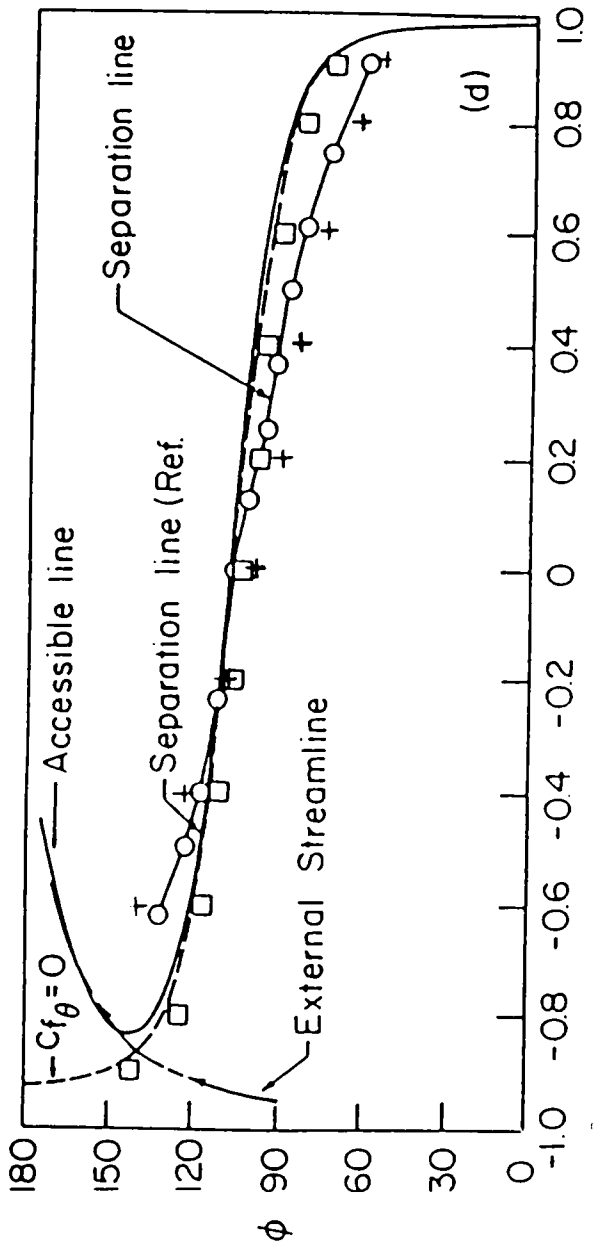

Fig. 5.11 Lines of separation and external streamlines for a prolate spheroid of a/b = 4 at an angle of attack α = 30° as reported in Cebeci, et al. (1981) (solid line); ----, Wang (1975); o-o-, present experimental results; +, present numerical results.

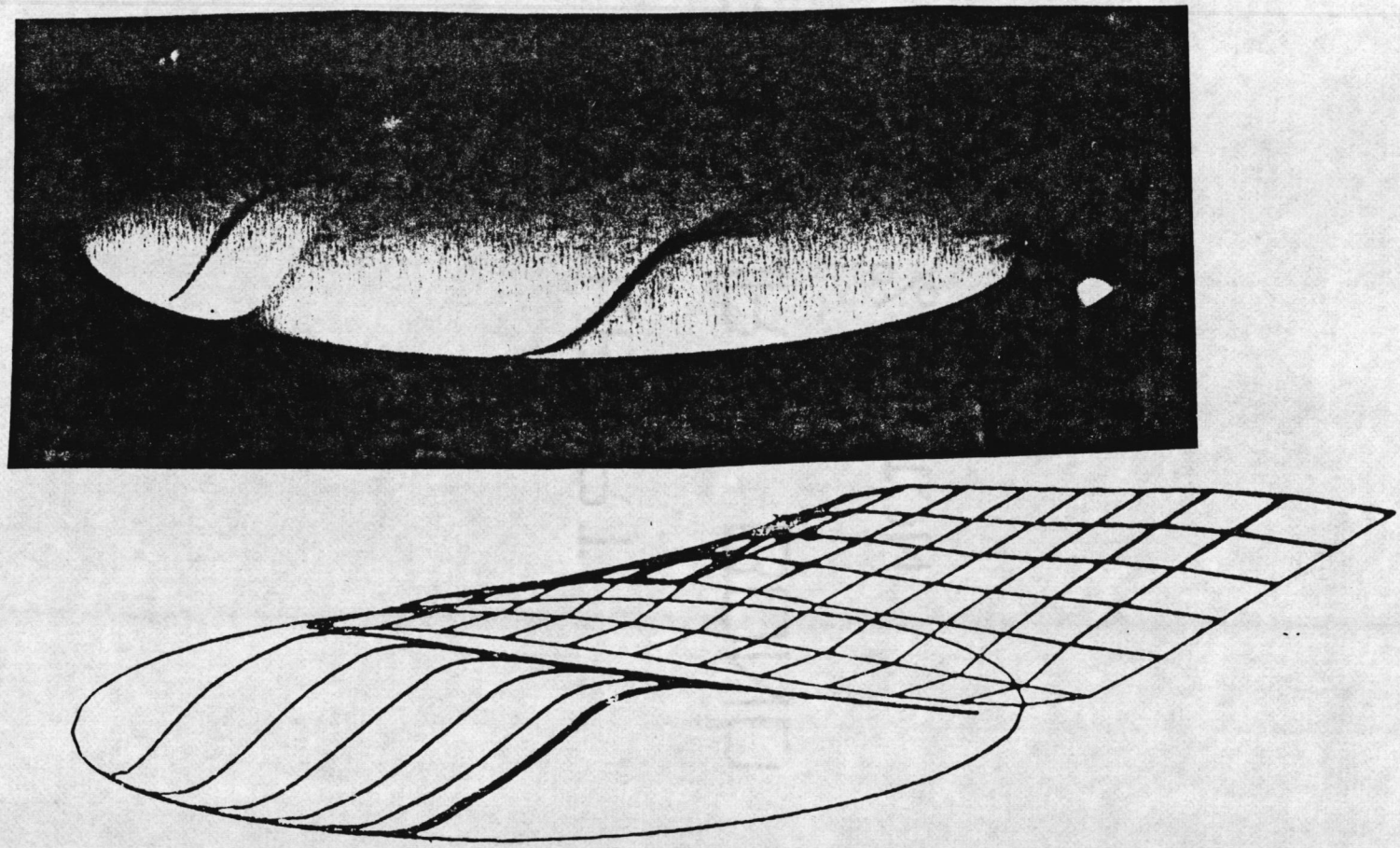

Fig. 5.12 Comparison of flow visualizations from Ref. 20 with present calculations. View from $\phi = 90°$.

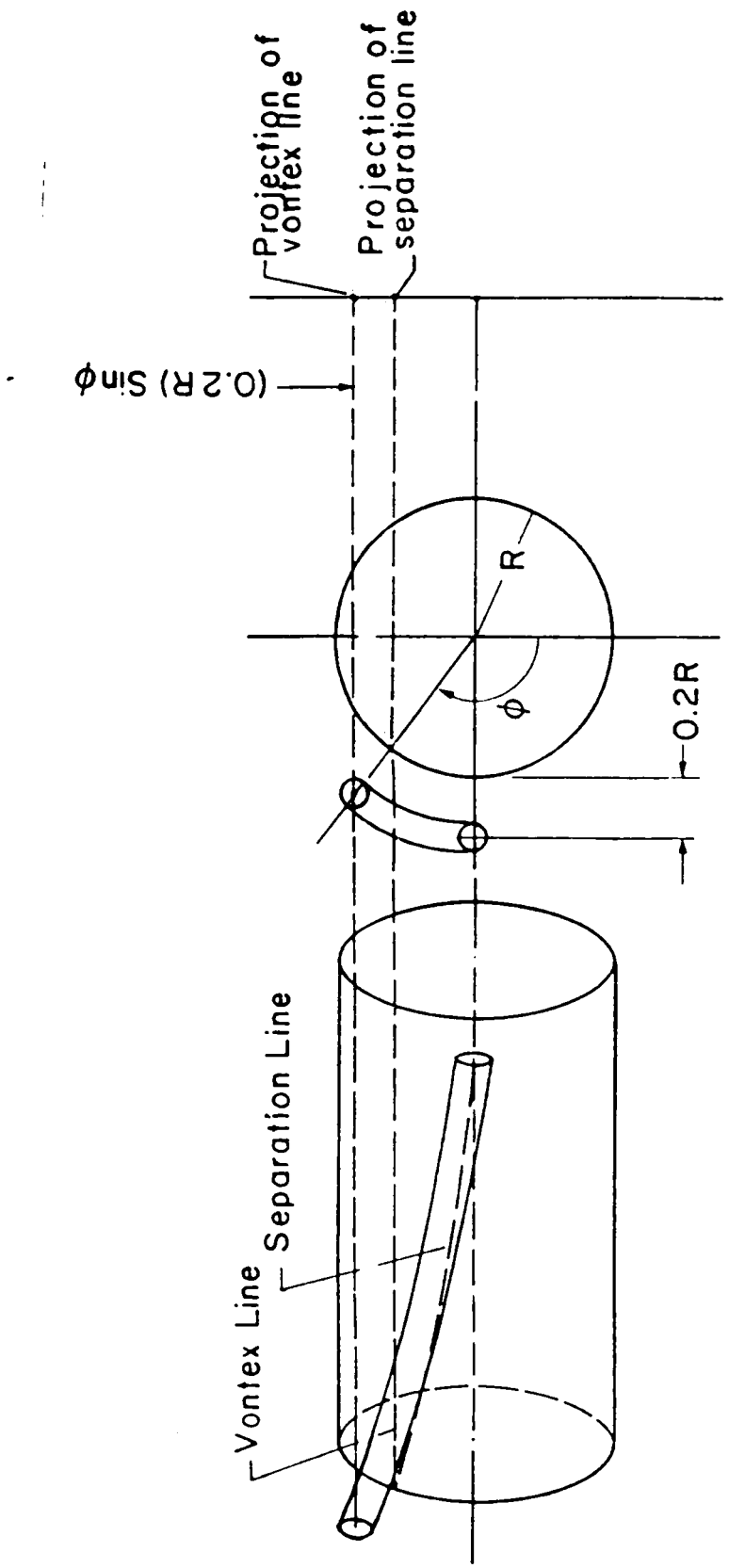

Fig. 5.13 Schematic representation showing a vortex line off the surface of the body.

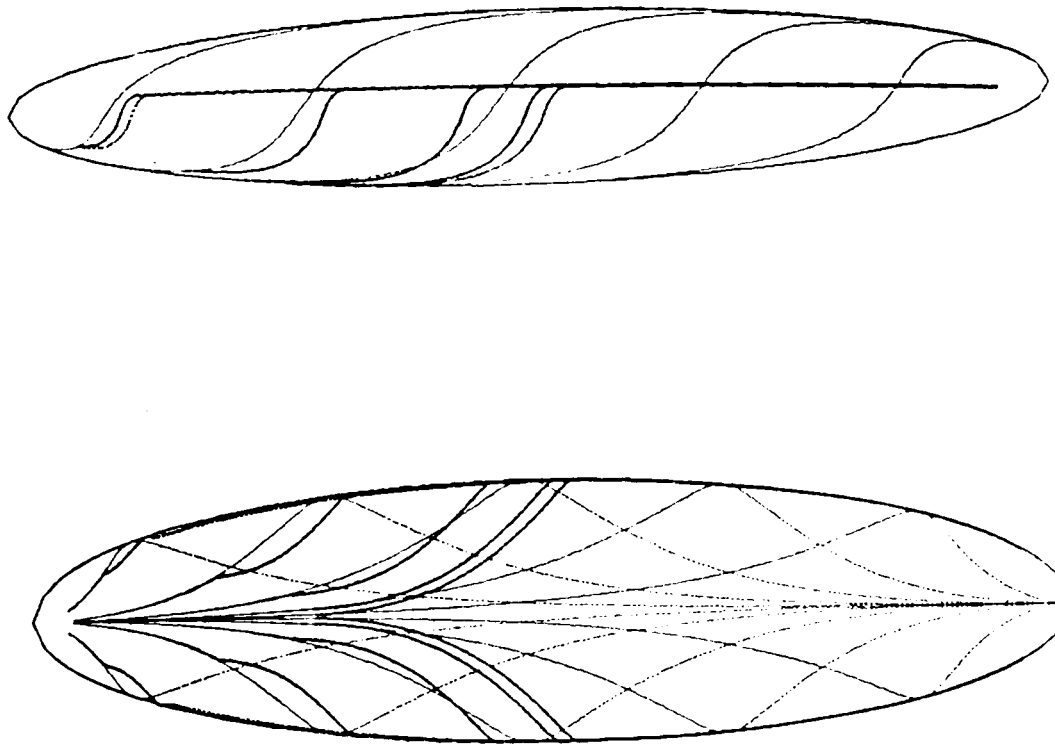

Fig. 5.14 Skin friction and potential lines of an ellipsoid with axes ratio 1:6:4

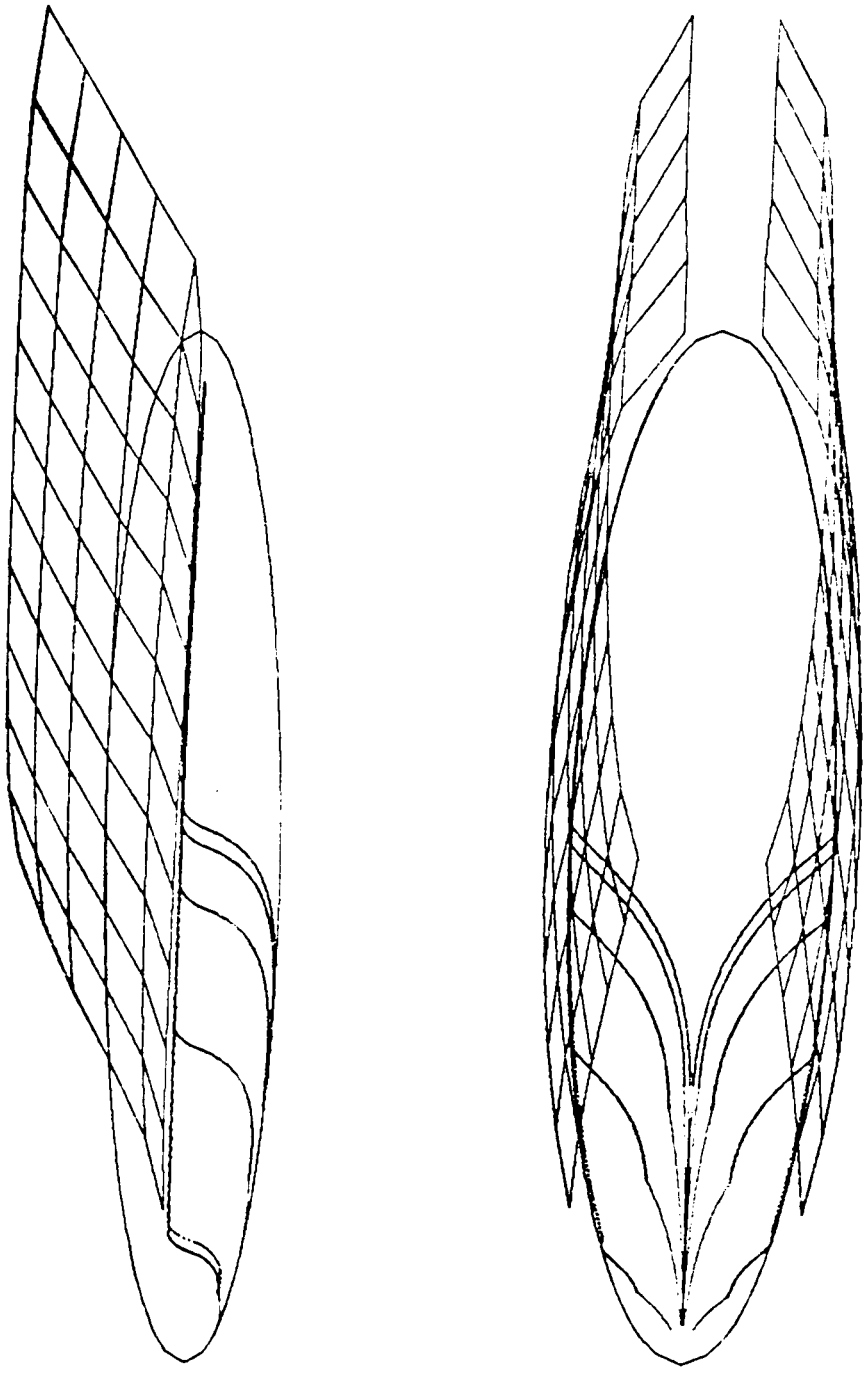

Fig. 5.14b Skin friction lines, potential lines and separated vortex sheets over an ellipsoid with axes ratio 1:6:4 started impulsively from rest at an angle of attack, $\alpha = 30^{\circ}$.

5.15, we show the results of the interactive code for the flow over an ogive-cylinder body at an angle of attack $\alpha = 24.5°$. Figure 5.16 displays results for the same body but with a line of separation fixed at the $\phi = 90°$ meridional. At the bottom of this figure, we present the calculated vector fields at two cross-sectional planes.

To facilitate comparison with the experimental results of Meier et al. (1980), it was necessary to prescribe the line of separation because their boundary layers were turbulent and our approximate code cannot handle this situation. The calculated wake is shown in Fig. 5.17, while in Fig. 5.18 we present a comparison between the analytical and the experimental velocity fields at a cross-section of the flow. Apparently the vortex sheet has not developed enough after 6 time steps. The experimental field indicates larger velocities in the vortex as well as a vortex core which is situated a little closer to the plane of symmetry.

A tape with the pressure distributions measured by Meier and his group have been available in the United States and were employed by other investigators as well for comparison. In Fig. 5.19 we display along two meridionals the experimental data obtained from the tape and the present numerical results. In the same figure, the potential flow results are shown.

Our analysis indicates that it is very hard to predict with a discrete-vortex method the pressure distribution underneath the separated flow region. Apparently the wake vortices break down quickly into turbulence which smooths out the pressure signature on the body. This became more obvious when we plotted our predicted distribution as a

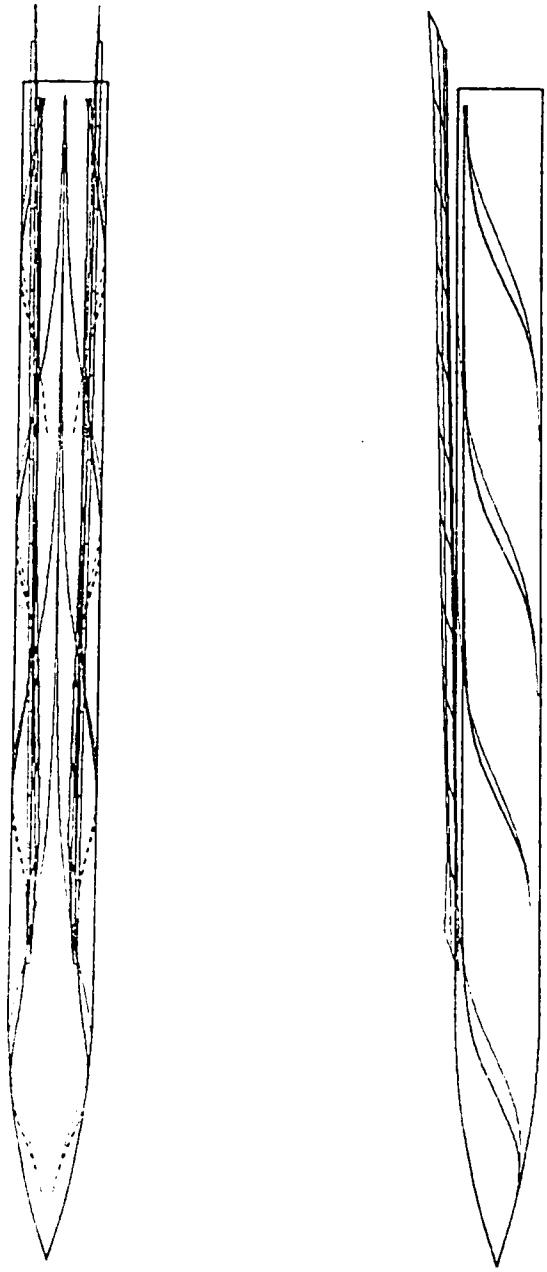

Fig.5.15 Skin friction lines, potential lines and separated vortex sheets over an ogive-cylinder body started impulsively from rest at an angle of attack, α = 24.5°.

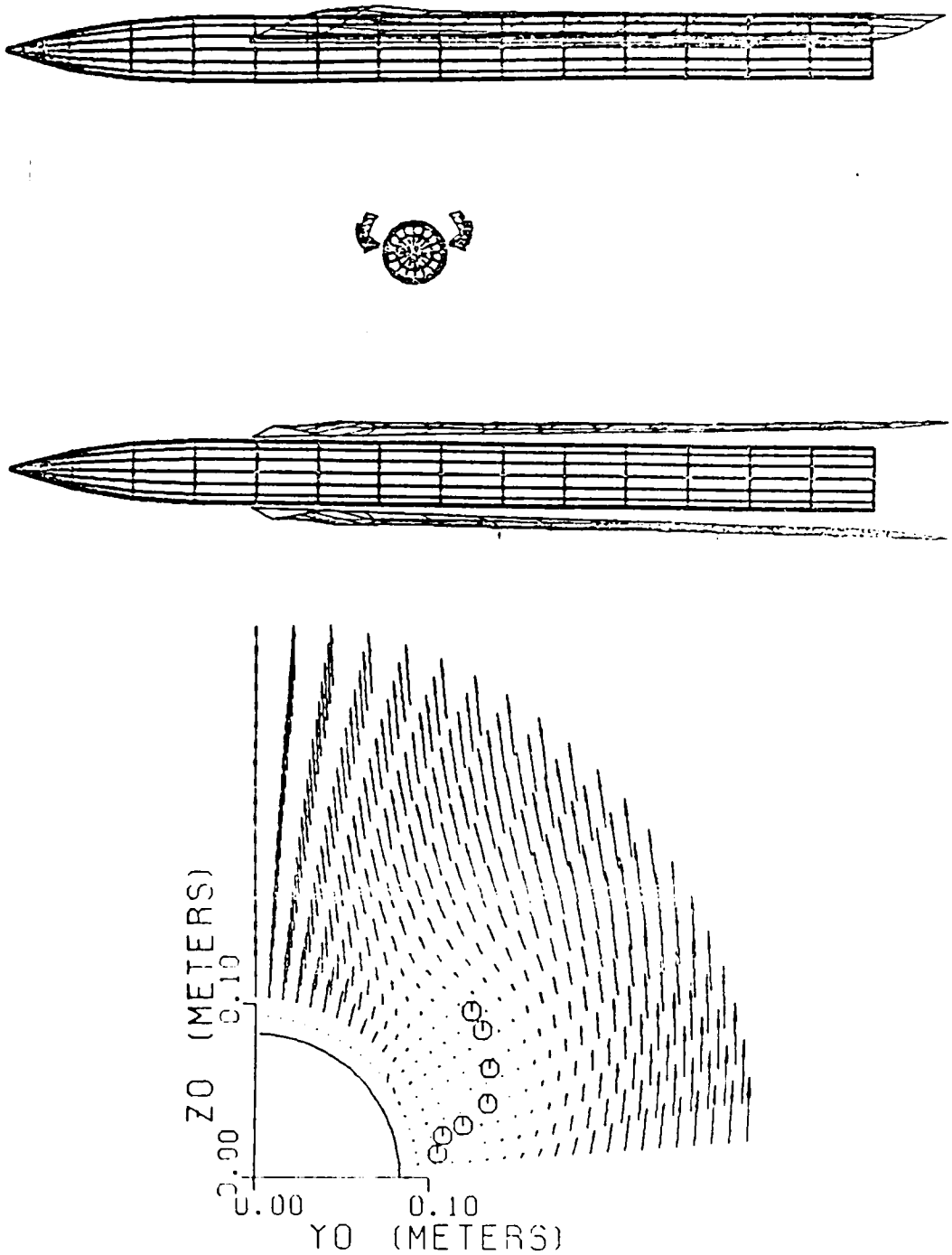

Fig. 5.16 Results for the body of Fig. 5.15 but with separation line fixed along a generator of the body.

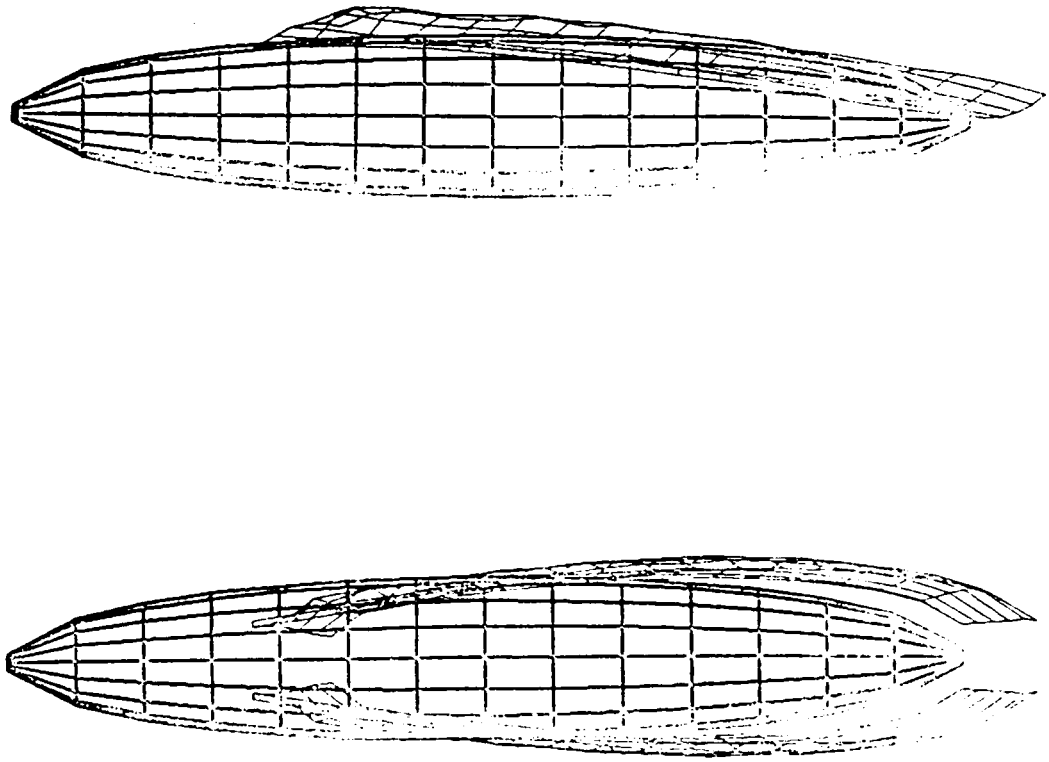

Fig. 5.17 The wake over a prolate spheroid with axes ratio 1:4 and the separation line fixed according to Meier's data.

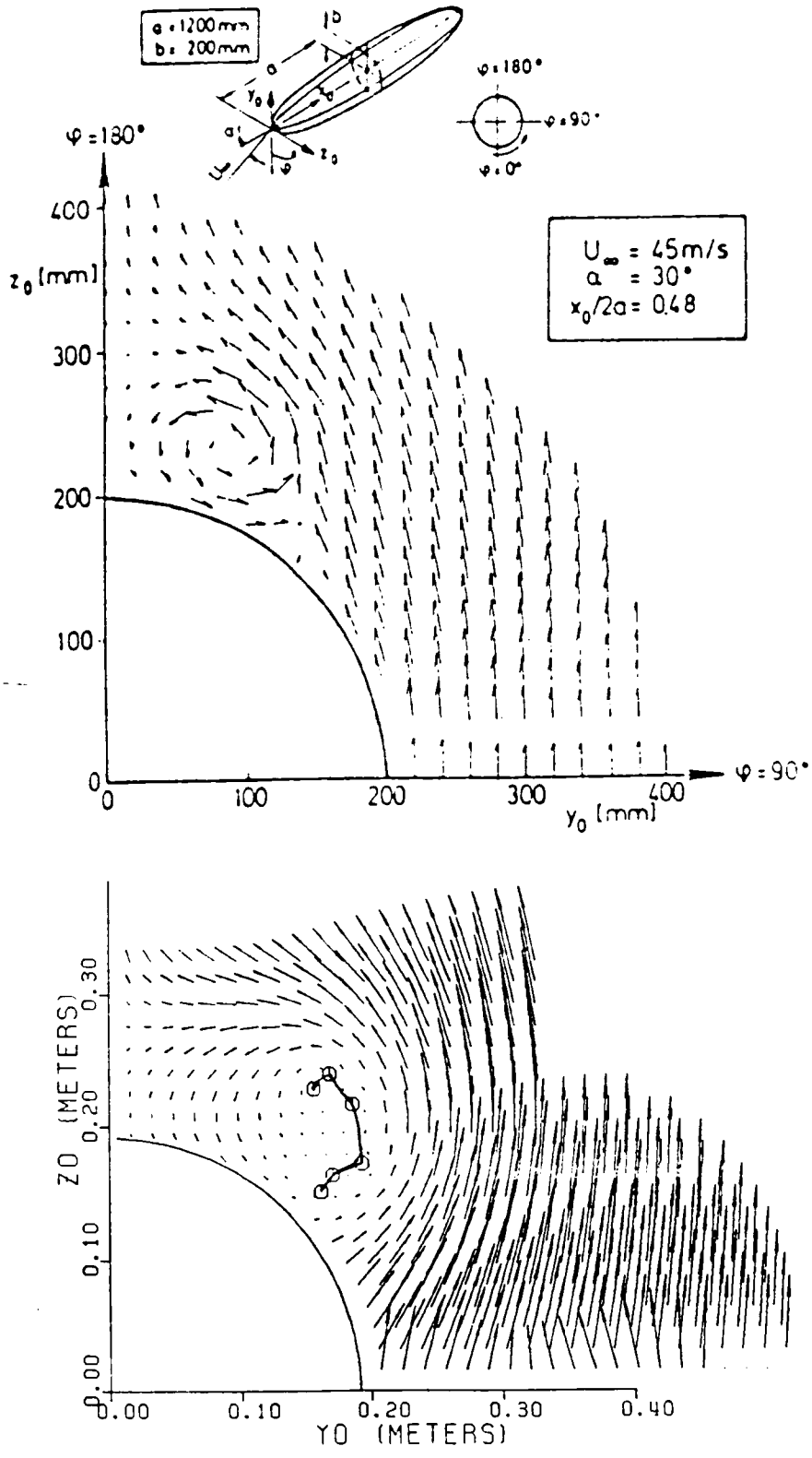

Fig. 5.18 Comparison of vector fields at a cross-sectional plane of x = 0.72. (a) Experiment, Meier, et al. (1980)
(b) Present theory.

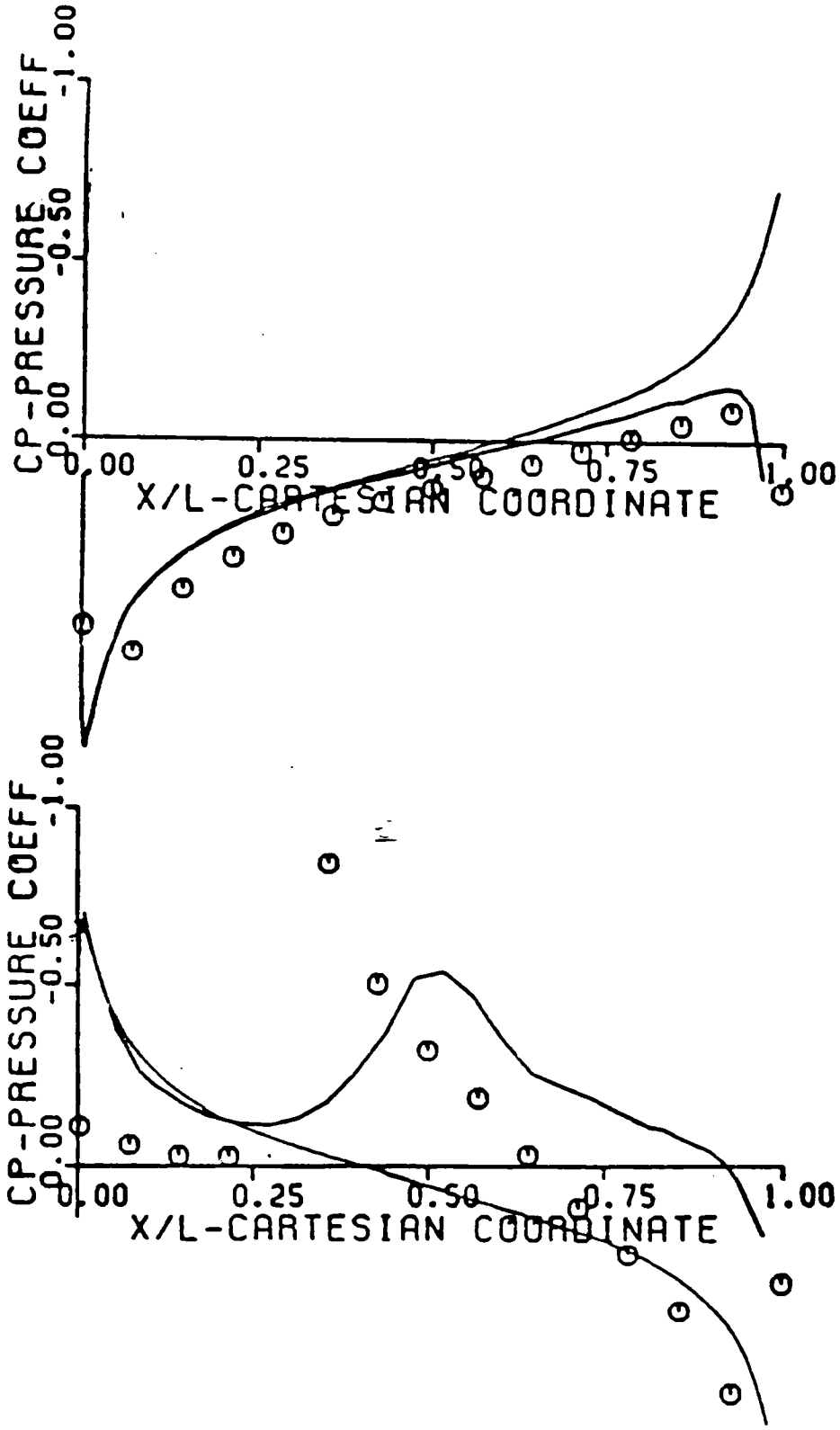

Fig. 5.19 Experimental and analytical pressure distributions for the case of Fig. 5.17, along the meridionals ϕ = 22.5° and 112.5°. O, experiment, Meier et al., (1980). _____, present theory; -----, potential flow.

function of the azimuthal angle. Another reason for this failure could be the limitation in the size of the grid and the number of vortex lines which make up the wake. An example of pressure distribution at $x/L = 0.4812$ is shown in Fig. 5.20. However, this relatively good agreement could not be reproduced at all stations and was found to depend upon the size of the time step.

The method can provide reliable results for the flow and pressure distribution over the attached flow region. However, the base pressure which incidentally varies with the length of the body can also be predicted simply by assuming that from separation and on to the leeward side, the pressure is uniform and equal to its value at separation. Results calculated in this way contrasted with experimental data are shown in Figs. 5.21 through 5.24.

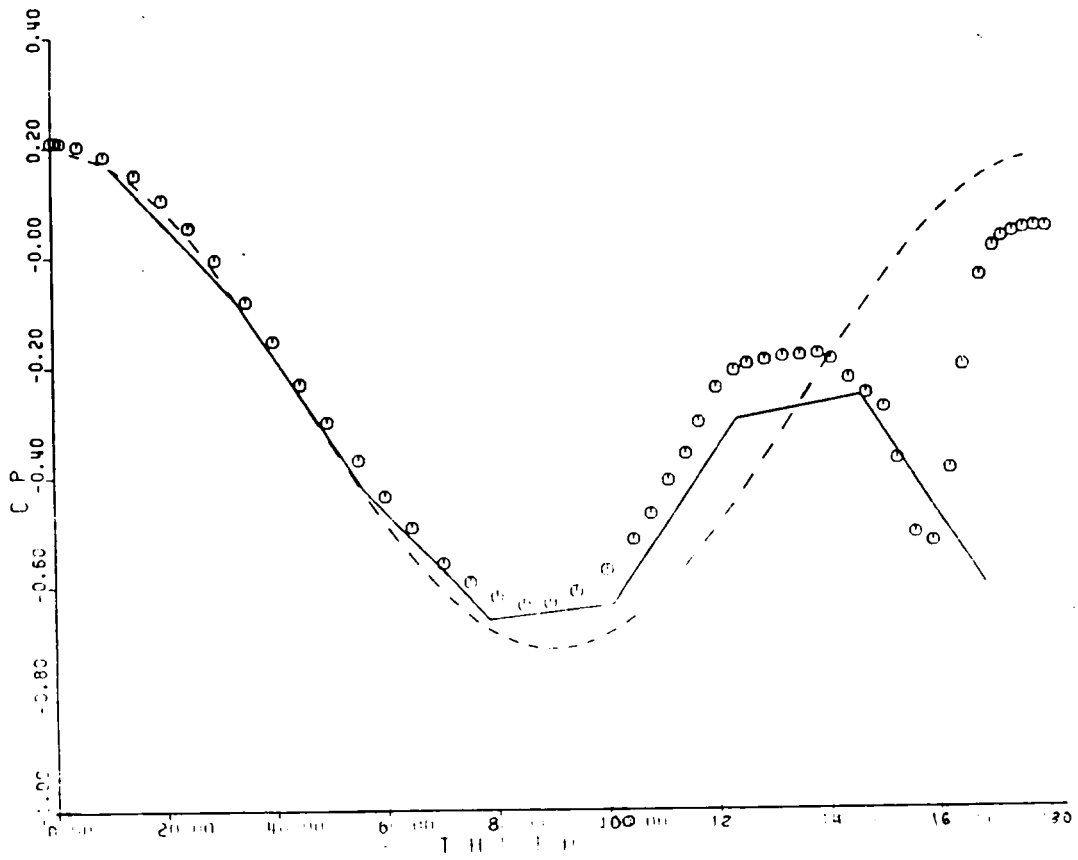

Fig. 5.20 Experimental and analytical pressure distribution for the case of Fig. 5.17, along the axial location x/L = 0.4812. O, experiment, Meier et al. (1980). _____, present theory; ---- potential flow.

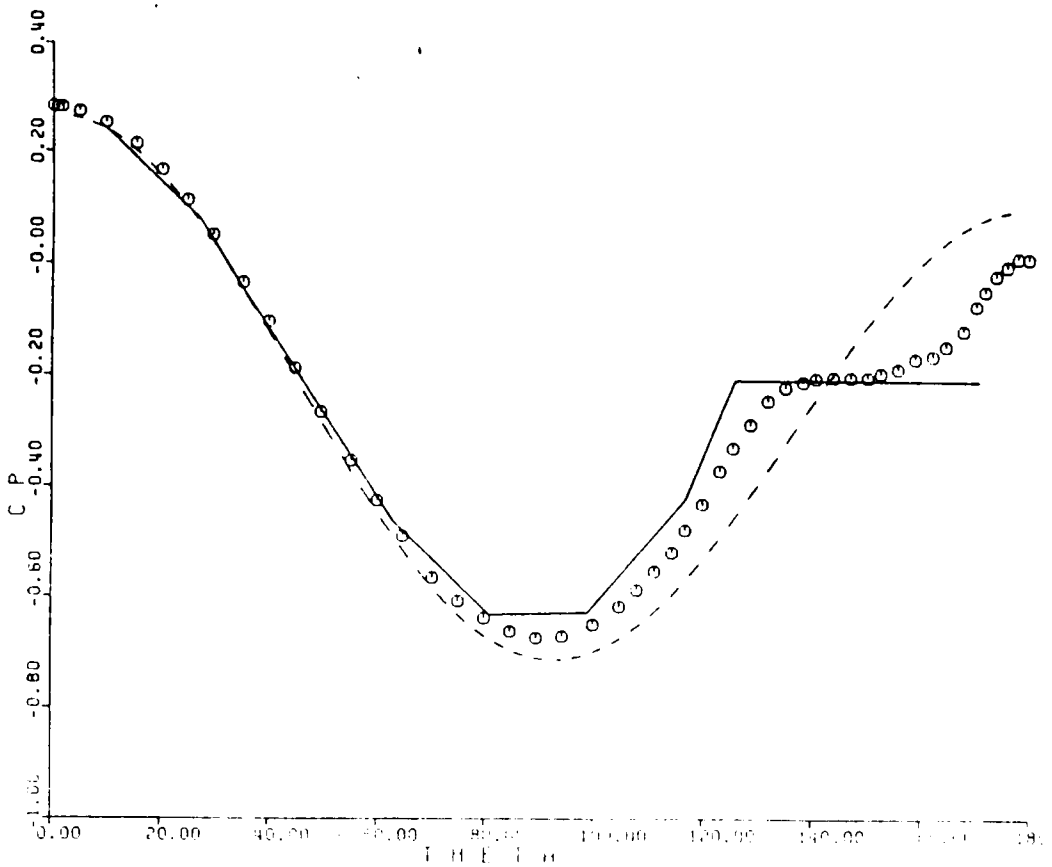

Fig. 5.21 Experimental and analytical pressure distribution for the case of Fig. 5.17, along the axial location x/L = 0.3501. O, experiment, Meier et al. (1980). _____, present theory; ----- potential flow.

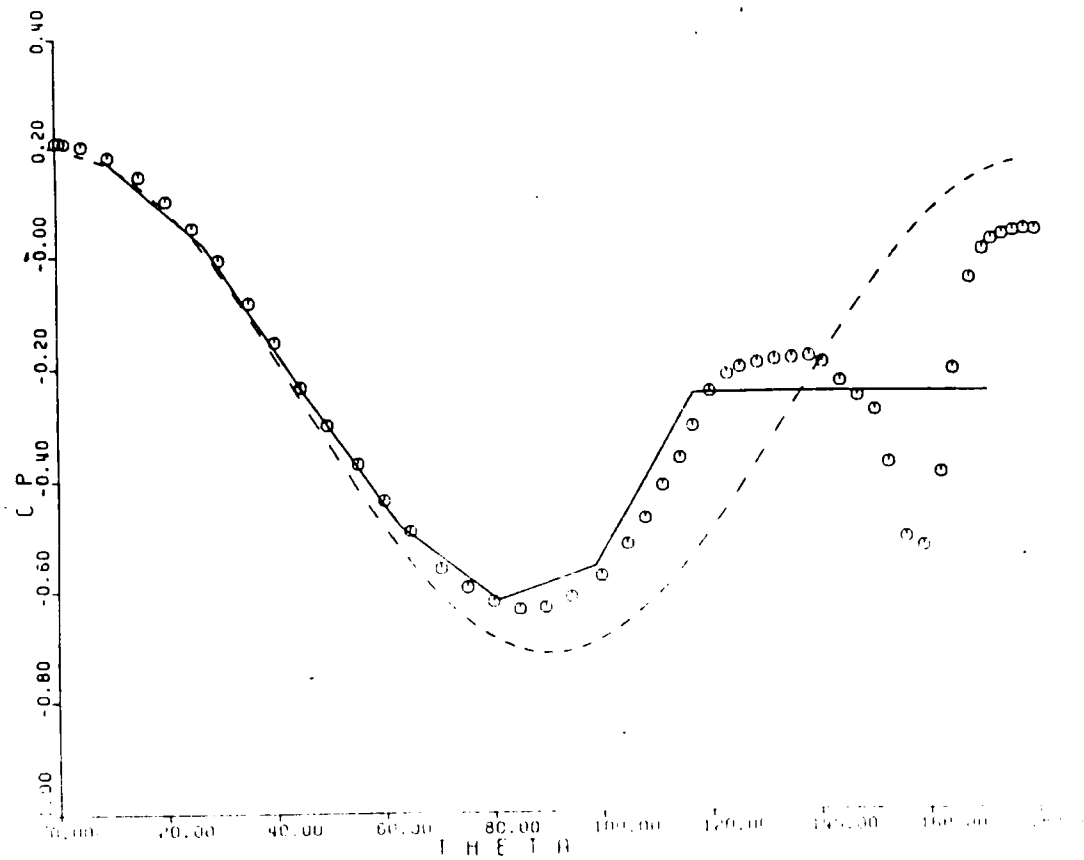

Fig. 5.22 Experimental and analytical pressure distribution for the case of Fig. 5.17, along the axial location x/L = 0.4812. O, experiment, Meier, et al. (1980). _____, present theory; ---- potential flow.

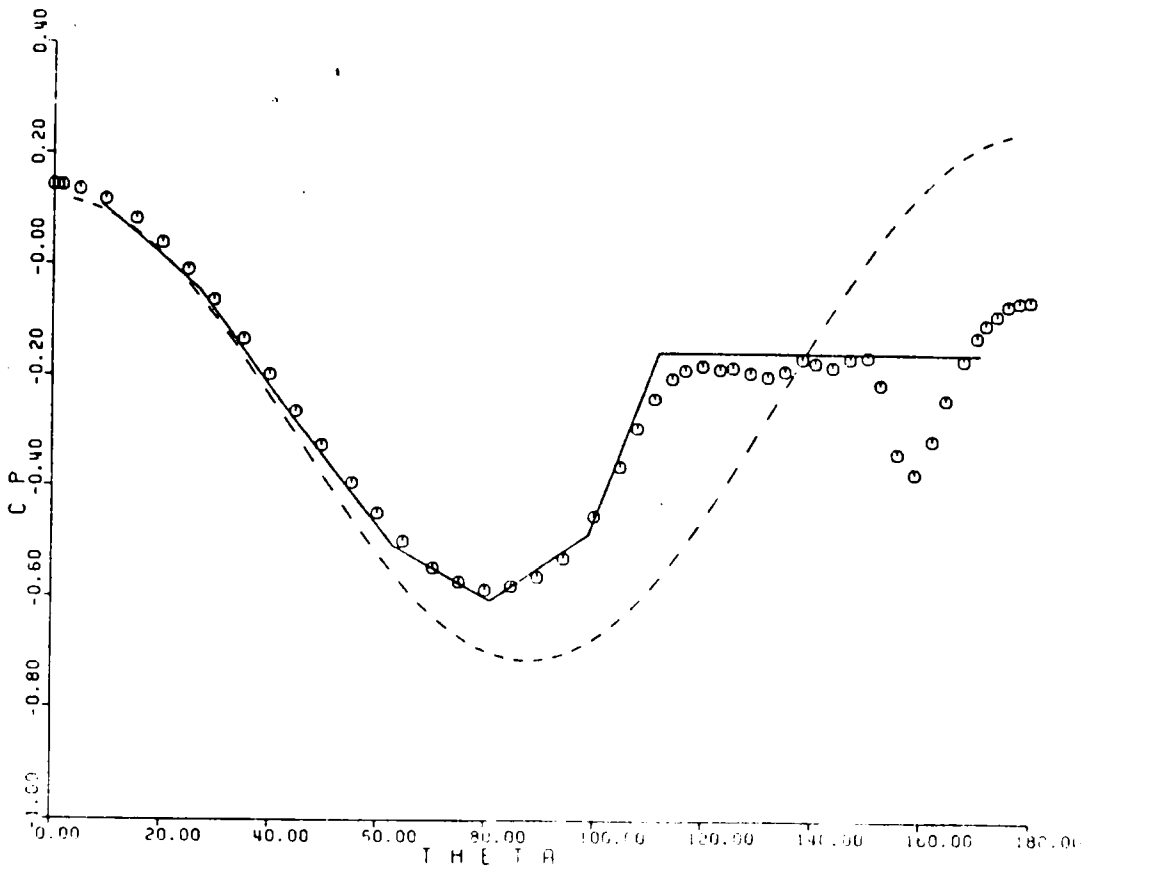

Fig. 5.23 Experiment and analytical pressure distribution for the case of Fig. 5.17, along the axial location x/L = 0.6061. O, experiment, Meier, et al. (1980). _____, present theory; ---- potential flow.

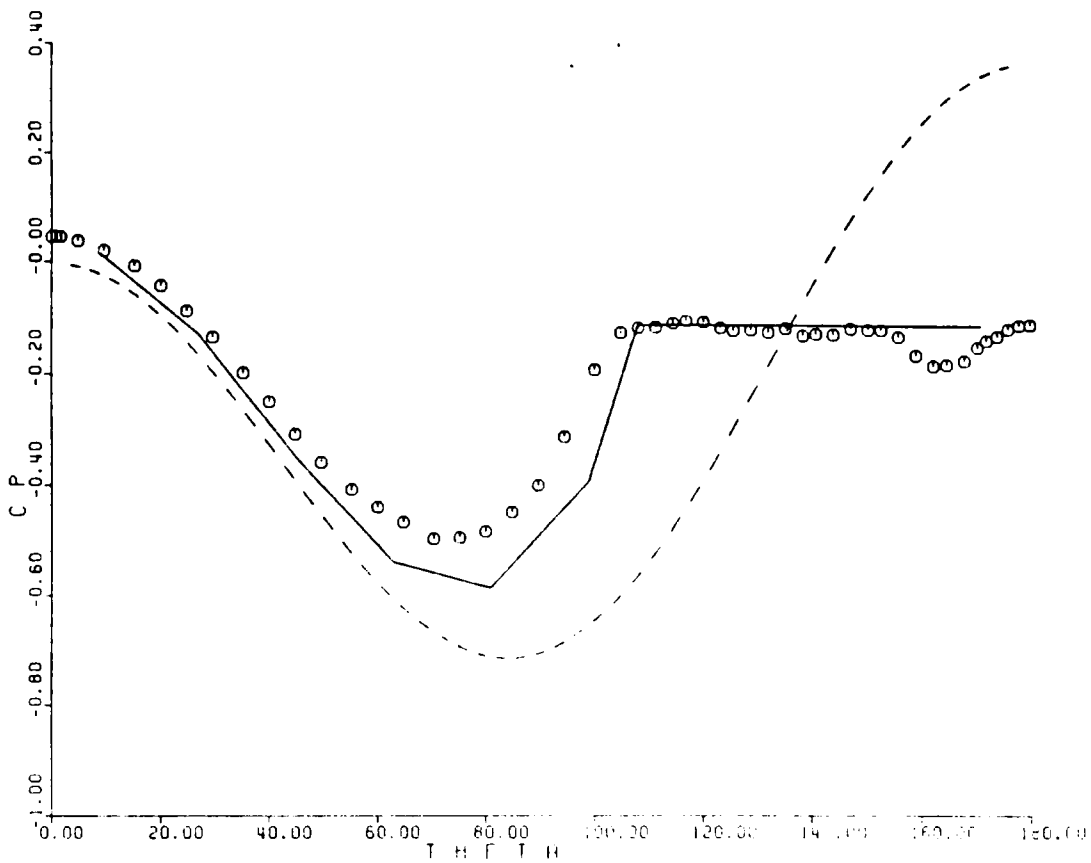

Fig. 5.24 Experimental and analytical pressure distribution for the case of Fig. 5.17 along the axial location x/L = 0.7725. O, experiment, Meier, et al. (1980). _____, present theory; --- potential flow.

CHAPTER VI

CONCLUSIONS AND RECOMMENDATIONS

In the present work we studied for the first time a three-dimensional separation problem at low Reynolds numbers. The importance of laminar flow separation lies in the fact that only then is it possible to disclose the true structure of the flow in the neighborhod of separation, which can then serve as a benchmark case for triple-deck asymptotic solution. Such solutions can then guide the numerical analyst to construct correct solutions to the full Navier-Stokes equations.

The present study revealed that the region of three-dimensional separation has a very complex structure. The experimental results, seem to reconcile the points of view of analyticians about closed and open separation. It appears that for a good range of angles of attack there exists open separation which is, in fact, compatible with boundary-layer studies. The present work generated a large number of flow visualizations which conclusively prove this point. However, our evidence further indicates that a secondary line of separation develops on the lee side of primary separation. In the region between the two lines of separation the flow changes sharply direction near the wall.

Due to the presence of highly inflectional profiles in the region between primary and secondary separation, the "lobes" of separation, i.e. in the regions II and III of Fig. 3.7 the flow is very unstable. Indeed for Reynolds numbers in the range of 10^5 to 10^6 primary separation is still laminar but the flow in regions II and III is fully

turbulent, as evidenced by the work of Meier and his co-workers. A full Navier Stokes calculation would tend to discolse the pattern discovered by the present work and therefore could run into difficulties if the grid size is not adjusted accordingly.

LDV measurements were obtained at the five stations in the forward portion of the ellipsoid. However, it appears necessary to obtain more data further downstream and, in fact, more detail is necessary in the neighborhood of the origin of open separation. The present data complement the evidence obtained by the flow visualization and offer benchmark results for comparison of numerical predictions.

The analytical work was motivated and guided by the experimental work. A very simple boundary-layer method was developed which proved to be very accurate in predicting the primary line of separation. This solution was interfaced with a vortex-lattice code in an interactive manner.

The present calculations have further demonstrated the potential of the vortex-lattice method. For the first time, a boundary layer solution, although somewhat crude, was coupled with the vortex-lattice solution to determine the location of separation and its displacement in time as the wake grows and rolls up. It was demonstrated that the strength of the shed vortex can be determined by simple approximate formulas which essentially represent integrals of boundary-layer profiles. The code we developed is not limited to the configurations considered here. The present results demonstrate that modeling the separating vortex sheets in a crude way, the method can predict with acceptable accuracy the line of primary separation and the pressure

distribution on the region of attached flow. However, the prediction of the pressure distribution underneath the developing wake is grossly in error. The calculations indicate sharp spikes which are the imprint of discrete vortices rolling over the solid surface. On the other hand, the experimental results display very smooth variations which betray the presence of a wide spectrum of eddies and fine turbulence. A refinement of the method may require a much larger number of discrete vortices to represent effectively the separating vortex sheets and some type of turbulence modeling for the fine structure of the random motion.

REFERENCES

Almonsino, D., 1985, "High Angle-of-Attack Calculations of the Subsonic Vortex Flow on Slender Bodies," AIAA Journal, vol. 23, pp. 1150-1156.

Almosnino, D. and Rom, J., 1983, "Calculation of Symetric Vortex Separation Affecting Subsonic Bodies at High Incidence", AIAA Journal, Vol. 21, pp. 398-406.

Atta, E. H., Kandil, O. A., Mook, D. T. and Nayfeh, A. H., 1976, "Unsteady Flow Past Wings Having Sharp Edge Separation", NASA SP-405, (Vortex-Lattice Utilization Workshop), pp. 407-418.

Band, E. G. U. and Payne, P. R., 1979, "The Pressure Distribution on the Surface of an Ellipsoid in Inviscid Flow," Aeronautical Quarterly, pp. 70-84.

Belotserkovskii, S. M., 1966, "Gust Effects on Wings of Complex Planforms at Subsonic Speeds", Mekanika Zhrdkosti i Craza, 4, pp. 129-138.

Blottner, F. G., and Ellis, M. A., 1973, "Finite-difference solution of the incompressible three-dimensional boundary-layer equations for a blunt body", Computers & Fluids, Vol. 1, pp. 133-158.

Cebeci, T., Khattab, A. K., and Stewartson, K., 1981, "Three-Dimensional Laminar Boundary Layers and the OK of Accessibility", J. Fluid Mech., Vol. 107, pp. 57-87.

Deffenbaugh, F. D. and Marshall, F. J., 1974, "Time-Development of the Flow About an Impulsively Started Cylinder", AIAA Journal, Vol. 14, pp. 908-913.

Eichelbrenner, E. A., and Oudart, A., 1955, "Methode de calcul de la couche limite. tridimensionelle," Application a une corps fusele incline sur le Vent. ONERA-Publication No. 76, Chatillon.

Fiddes, S. P., 1980, "A Theory for the Separated Flow Past a Slender Elliptic Cone at Incidence", RAE Tech Memo 1858.

Geissler, W., 1974, "Three-dimensional laminar boundary layer over a body of revolution at incidence and with separation", AIAA J., Tech. Note, Vol. 12, No. 12, pp. 1743-1745.

Gerrard, J. H., 1966, "The Mechanics of the Formation Region of Vortices Behind Bluff Bodies", Journal of Fluid Mechanics, Vol. 25, pp. 401-411.

Han, T. and Patel, V. C., 1979, "Flow separation on a spheroid at incidence", J. Fluid Mech., Vol. 92, Part 4, pp. 643-657.

Kandil, O. A., Mook, D. T. and Nayfeh, A. H., 1976, "A New Convergence Criterion for the Vortex-Lattice Models of Leading Edge and Wing-tip Separation", NASA-SP-405 (Vortex-Lattice Utilization Workshop), pp. 285-300.

Konstadinopoulos, P., Mook, D. T. and Nayfeh, A. H., 1981, "A Numerical Method for General Unsteady Aerodynamics," AIAA Paper 81-1877, also AIAA Journal, vol. 22, pp. 43-49, 1985.

Kuwahara, K., 1978, "Study of Flow Past a Circular Cylinder by an Inviscid Model", Journal of the Physical Society of Japan, Vol. 45, pp. 292-297.

Levin, D. and Katz, J., 1980, "A Vortex-Lattice Method for the Calculation of the Nonsteady Separated Flow Over Delta Wings", AIAA Paper No. 80-1803.

Maskell, E. C., 1955, "Flow Separation in Three Dimensions", RAE Aero Report 2565.

Meier, H. U., and Kreplin, H.-P., 1980, "Experimental study of boundary layer velocity profiles on a prolate spheroid at low incidence in the cross section x/L = 0.64", AFFDL-TR-80-3088, pp. 169-189.

Meier, H. U., Kreplin, H.-P. and Vollmers, H., 1981, "Velocity Distributions in 3-D Boundary Layers and Vortex Flows Developing on a Inclined Prolate Spheroid", DFVLR-AVA-Report IB 222-81-CP-1.

Merzkirch, W., 1980, Flow Visualization II, Hemisphere, Washington, New York, London.

Mook, D. T. and Maddox, S. A., 1974, "Extension of a Vortex-Lattice Method to Include the Effects of Leading-edge Separation", Journal of Aircraft, 11, 2, p. 127.

Oudart, A. and Eichelbrenner, E. A., 1955, "Methode de Calcul de la Couche Limite Tridimensionelle," ONERA publication No. 76.

Patel, V. C., and Choi, D. H., 1979, "Calculation of three-dimensional laminar and turbulent boundary layers on bodies of revolution at incidence", 2nd Symposium on Turbulent Shear Flows, pp. 15.14-15.24, Imperial College, London.

Patel, V. C. and Baek, J. H., 1983, "Calculations of Boundary Layers and Separation on a Spheroid at Incidence", in Numerical & Physical Aspects of Aerodynamic Flows, ed. T. Cebeci.

Ragab, S. A., 1982, "A Method for the Calculation of Three-Dimensional Boundary Layers with Circumferential Reversed Flow on Bodies", AIAA-82-1023.

Ramaprian, B. R., Patel, V. C. and Choi, D. H., "Mean Flow Measurements in the Three-Dimensional Boundary Layer Over a Body of Revolution at Incidence," Journal of Fluid Mechanics, Vol. 103, pg. 81, pp. 479-504.

Sarpkaya, T., 1968, "An Analytical Study of Separated Flow About Circular Cylinders", Journal of Basic Engineering, Vol. 90, pp. 511-520.

Sarpkaya, T. and Schoaff, R. L., 1979, "Inviscid Model of Two-Dimensional Vortex Shedding of a Circular Cylinder", AIAA Journal, 17, 11, November, pp. 1193-1200.

Sears, W. R., 1948, "The Boundary Layers of Yawed Cylinders", Journal of Aeronautical Sciences, 15, 1, pp. 19-52.

Sears, W. R., 1976, "Unsteady Motion of Airfoils with Boundary-Layer Separation", AIAA J., Vol. 14, No. 2, pp. 216-220.

Stock, H. W., 1980, "Computation of the boundary layer and separation lines on inclined ellipsoids and of separated flows on infinite swept wings", AIAA-80-1442.

Tai, T. C., 1981, "Determination of Three-Dimensional Flow Separation by a Streamline Method", AIAA Journal, Vol. 19, No. 10, pp. 1264-1271.

Telionis, D. T. and Costis, C. E., 1983, "Three Dimensional Laminar Separation", VPI & SU Engineering Report, No. VPI-E-83-4.

Thrasher, D. F., Mook, D. T., Kandil, O. A. and Nayfeh, A. H., 1977, "Application of the Vortex-Lattice Concept to General, Unsteady Lifting Surface Problems", AIAA Paper No. 77-1157.

Thrasher, D. F., 1983, "Application of the Vortex-Lattice Concept to Flows with Smooth-Surface Separation", NSRDC Report.

Tobak, M. and Peake, J., 1982, "Topology of Three-Dimensional Separated Flows", Annual Reviews of Fluid Mechanics, Vol. 14, pp. 61-85.

Wang, K. C., 1974, "Boundary Layer Over a Blunt Body at High Incidence with an Open-Type of Separation," Proc. Royal Society, Vol. A340, pp. 33-55.

Wang, K. C., 1975, "Boundary layer over a blunt body at low incidence with circumferencial reversed flow", J. Fluid Mech., Vol. 72, part 1, pp. 49-65.

Wang, K. C., 1982, "New Developments About Open Separation", S.D.S.U. Engineering Report, AE&EM TR-82-02.

Zorea, C. R. and Rom, J., 1978, "The Calculation of Nonlinear Aerodynamic Characteristics of Wings and Their Wakes in Subsonic Flow", Israel Journal of Technology, 16, pp. 83-96.

The vita has been removed from the scanned document

SEPARATION AND WAVES OVER THREE-DIMENSIONAL BODIES

by

CHRISTOPHER E. COSTIS

(ABSTRACT)

The laminar flow over a prolate spheroid was investigated via flow visualization and Laser-Doppler Velocimetry. Experiments were conducted in a water tunnel and the flow was visualized with dyes. The measurement of three-dimensional boundary layers required a special design of the laser optics. Attention was focused in the neighborhood of three-dimensional separation.

The Vortex-Lattice method was employed to calculate the inviscid flow and the development of separated vortex sheets over a prolate spheroid. An approximate-method based on the assumption of local similarity was used to solve the boundary layer equations and calculate the line of open separation. A condition of vortex shedding along separation is proposed. The two schemes, viscous and inviscid, interact through the line of separation which is allowed to displace as the wake grows. Results are compared with flow visualization data for laminar separation and pressure data for turbulent separation.